व **VIDYA**

*The word Vidya, taken from the Vedanta philosophy of the Hindus,
means knowledge. The symbol used to denote the Vidya organization
is the letter "V" from Sanskrit, the ancient language of India.*
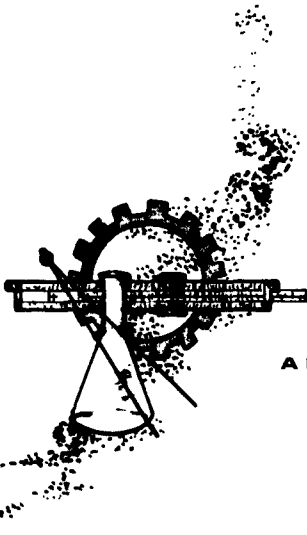
APPLIED MECHANICS . . . . PHYSICS . . . . ANALYSES

VIDYA REPORT NO. 91*

March 31, 1963

A THEORY FOR THE LOW-SPEED AERODYNAMICS OF STRAIGHT AND SWEPT WINGS WITH FLOW SEPARATION

by

Alvin H. Sacks
Jack N. Nielsen
Frederick K. Goodwin

VIDYA

A DIVISION OF Itek CORPORATION

ACKNOWLEDGMENT

SUMMARY

A mathematical theory is developed for the low-speed aerodynamics of rectangular wings with side-edge separation. This theory is then extended to wings with sweptback leading edges (and straight trailing edges) by representing the actual wing as a system of elementary rectangular wings of varying aspect ratio. Thus, in the limit, steady separation along the entire leading edge is approximated, and the theory leads to an iterative computational procedure for calculating the aerodynamic characteristics of sweptback wings with leading-edge separation.

The assumed vortex system of the elementary rectangular wing consists of a lifting line with its associated trailing sheet (lying in the plane of the wing) and a separated vortex sheet from each side edge with an associated bound vortex system in the wing. The Kutta condition is satisfied along the side edges, and the boundary condition of no flow through the wing is satisfied along a selected control line for all spanwise points by means of Fourier analysis. The resulting theory includes the classical lifting-line theory of Prandtl and provides a means of calculating the span load distribution as well as the strength of the shed vortices and the resulting downwash throughout the flow field. The shedding angles of the separated vortices are found by an iterative technique in which the vortices are required to be shed at the angle of the local flow immediately outside the side edges.

Calculations are presented which demonstrate convergence of the method for both rectangular and delta wings, both with and without iteration on the shedding angles of the separated vortices. Comparisons with experiment are also presented for aspect ratios up to five, and it is found that for rectangular wings the calculated normal forces using one wing element are in all cases within 10 percent of experiment but the calculated shedding angles are unrealistically high. For delta wings, the high shedding angles evidently cause high predicted normal forces. However, the present theory gives very good agreement for normal force and

center of pressure for delta wings of aspect ratios from one to
four, provided that an appropriate shedding angle is assumed and
held fixed. In this event, the present theory gives substantial
improvement over linear theory for the prediction of normal force
and center of pressure, particularly at the lower aspect ratios.
The required shedding angle is found to depend only on aspect
ratio and decreases nonlinearly with increasing aspect ratio.

iv

TABLE OF CONTENTS

SYMBOLS

A	aspect ratio
a_n	Fourier coefficients of function defined by Equation (25)
a_{nj}	Fourier coefficients of a_n (see Eq. (70))
b_j	Fourier coefficients of downwash from other wing elements (see Eq. (74))
c	local wing chord
c_k	chord of kth rectangular wing element (taken as c_o/n_w)
c_l	local lift coefficient on chordwise strip (see Eq. (94))
C_N	normal force coefficient, $\dfrac{N}{\frac{1}{2}\,\rho V_\infty^2 S}$ or $\dfrac{N}{\frac{1}{2}\,\rho V_\infty^2 S_o}$
c_o	total chord of sweptback wing
f_n	downwash function associated with a_n (see Eq. (30))
f_{nj}	Fourier coefficients of f_n (see Eqs. (30) and (40))
g_j	Fourier coefficients of $\bar{w}$ (see Eq. (35))
N	total normal force
n_h	number of nonzero harmonics in the series representation of the loading $\gamma(\eta)$
N_l	normal force acting on the lifting line
n_w	number of rectangular wing elements used to represent a sweptback wing
s	semispan of rectangular wing or lifting line
S	planform area of rectangular wing
s_i	semispan of ith rectangular wing element
s_o	semispan of swept wing
S_o	planform area of swept wing
s_v	semispan of elementary horseshoe vortex (see sketch, p. 25)

u, v, w	velocity components in the x, y, z directions, respectively
V_∞	free-stream velocity
w_v	upwash in the plane of the wing due to an elementary horseshoe vortex of unit strength lying in the plane of the wing
$\left.\begin{array}{l} x, y, z \\ \xi, \eta, \zeta \end{array}\right\}$	Cartesian coordinates fixed in the wing (see Fig. 1)
$\bar{x}$	distance of center of pressure behind wing leading edge
x_c	distance from leading edge of rectangular wing to its control line
x_i	distance of ith control line behind leading edge of kth rectangular wing
$(\ )^*$	induced by the lifting line and its trailing sheet lying in the plane of the wing (including image system of separated flow)
$(\bar{\ })$	induced by the horseshoe vortices representing the separated flow
$\|\ \|$	absolute value
α	angle of attack
$\gamma(\eta)$	spanwise circulation distribution of the lifting line
γ_n	Fourier coefficients of $\gamma(\eta)$ (see Eq. (13))
$\gamma_n{}^*$	$n\gamma_n / 4\pi s V_\infty \sin \alpha$
$d\Gamma/d\xi$	circulation per unit length of vortices shed from side edges (see Fig. 1)
Γ^*	$\dfrac{(d\Gamma/d\xi)c}{4\pi s V_\infty \sin \alpha}$
ϵ	a vanishingly small distance
θ	angle of vortex shedding from rectangular wing (see Fig. 1)
ξ_i	distance of lifting line behind leading edge of rectangular wing (taken as 0.25 c)

ξ_k distance of kth lifting line behind leading edge of kth rectangular wing element (taken as 0.25 c_k)

ρ fluid mass density

ψ $\cos^{-1}(-\eta/s)$

ψ_i $\cos^{-1}(-y/s_i)$

ψ_o $\cos^{-1}(-y/s)$

Subscripts

B   induced by bound portion of horseshoe vortex

L   induced by left trailing vortex

R   induced by right trailing vortex

$(\ )_{av}$ average of values on opposite sides of vortex sheet

$(\ )_{ik}$ induced at i^{th} control line by vortex system associated with k^{th} rectangular wing element

$(\ )_{IT}$ iterated value

$(\ )_S$ due to separation (for $\Gamma^* = 1$)

$(\ )_u$ with no separation (for $\Gamma^* = 0$)

LIST OF FIGURES

A THEORY FOR THE LOW-SPEED AERODYNAMICS OF STRAIGHT AND SWEPT WINGS WITH FLOW SEPARATION[1]

1. INTRODUCTION

When a thin rectangular wing is set at a small angle of attack in a uniform incompressible stream, the flow remains attached to the wing surface so that all of the shed vorticity lies in a sheet which contains the wing planform and proceeds to roll up gradually after leaving the wing trailing edge (see sketch).
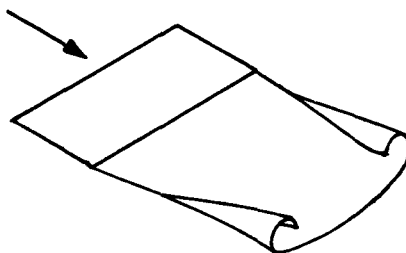
The aerodynamic behavior of such wings at low angles of attack is well predicted by the classical lifting line theory developed by Prandtl. As the angle of attack is increased, the side edges become more oblique to the free stream, the fluid can no longer negotiate the $180°$ turn at the side edges (from lower to upper surface), and side-edge separation occurs, giving rise to two additional vortex sheets which, at higher angles of attack, begin to roll up even ahead of the wing trailing edge (see sketch).

---
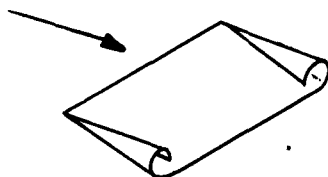
[1]This report supersedes Vidya Report No. 38.

Finally, at still higher angles of attack, the flow separates from the leading edge, giving rise to vortices whose axes are essentially normal to the free-stream direction. For this reason, the leading-edge vortices must pass downstream with the general flow, producing an unsteady flow with vortex shedding in the manner of flow past a bluff body (see sketch).
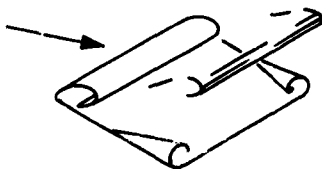
The angles of attack at which the foregoing phenomena occur and the rates of rolling up and shedding depend upon the aspect ratio of the wing, the sharpness of its various edges, and upon the Reynolds number of the free stream. In the early years of airplane flight, wings of practical design were of rather high aspect ratio with well-rounded leading and side edges. Consequently, separation from the side edges was negligible, and the classical lifting line theory was applicable over practically the entire usable angle-of-attack range up to the onset of the familiar stall, corresponding roughly to the leading-edge separation discussed above.

More recently, however, both wing thickness and aspect ratio have diminished (to gain high-speed performance) so that the intermediate regime of side-edge separation has become increasingly important. Furthermore, for wings with sweptback leading edges (e.g., delta wings) the intermediate regime of steady-state separated flow is typical of the landing condition, since such wings do not "stall" in the usual sense. It is in this connection that the present investigation has been undertaken.

The analytical work of the existing literature will first be reviewed as it bears upon the physical problem discussed here, and then a new theory will be developed for the analytical treatment of rectangular wings with side-edge flow separation. This theory will then be extended to the case of sweptback wings with leading-edge separation, using the rectangular wing as an elementary building block. Convergence of the method will be demonstrated, and numerical calculations of normal force and center of pressure for both rectangular and delta wing planforms will be presented. Finally, comparisons will be made with available experimental data, including some span load distributions and vortex shedding angles for delta wings, and the limitations of the theory will be discussed in some detail.

2. LITERATURE SURVEY - STATE OF THE ART

The fact that there exists an apparent fundamental difference between the aerodynamic behavior of rectangular and triangular wings at high angles of attack has been recognized for many years. It is therefore natural that attempts at analytical treatments of high-angle-of-attack phenomena have generally fallen into one or the other of these two categories, and only one serious attempt has been made to formulate a general theory which would handle wings of arbitrary planform exhibiting steady flow separation. Furthermore, the inherent unsteady character of the flow at angles of attack beyond the stall and the strong dependence on viscous phenomena have inhibited analytical progress on the problem of stalled rectangular wings. The first major contribution along these lines was made in 1939 by W. Bollay, who evidently recognized that, for rectangular wings of low aspect ratio, separation occurs mainly along the side edges and that this type of separation produces a steady flow.

2.1 Rectangular Wings

2.1.1 Small aspect ratio

The theory of W. Bollay (Ref. 1) treats rectangular wings of small aspect ratio under the assumption that all shed vortices lie in two planes normal to the wing surface and containing the side edges. Thus, the wing is represented as a continuous distribution of horseshoe vortices lying at some angle θ to the wing surface, as shown in the following sketch:
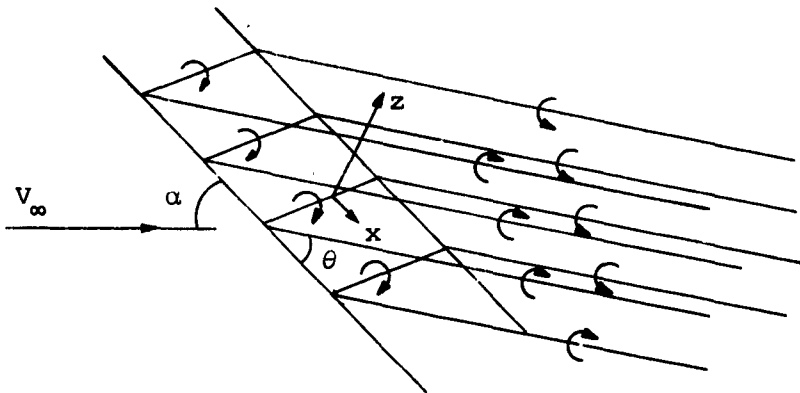
The angle θ is assumed constant and the vortex strengths γ are assumed to be constant across the span (uniform span loading) but continuously varying in the chordwise direction. The chord load distribution is taken to be that of a flat plate of infinite aspect ratio with a singularity at the leading edge; that is,

$$\gamma = \gamma_o \sqrt{\frac{\frac{c}{2} - x}{\frac{c}{2} + x}} \tag{1}$$

where γ is the circulation per unit length and c is the chord. The boundary condition of no flow through the plate is satisfied "in the mean" along the centerline of the plate. Thus,

$$\int_{-\frac{1}{2}}^{+\frac{1}{2}} w \, d\left(\frac{x}{c}\right) = - V_\infty \sin \alpha \qquad (2)$$

where w is the total velocity in the z-direction due to the bound and trailing vortices. This procedure leads to a rather complicated integral equation which is to be solved for the constant γ_0. Since the solution depends upon the shedding angle θ, Bollay determines this angle from the induced velocities by imposing the condition that the free vortices must follow the streamlines. This condition is imposed only in the vertical plane (which means the lateral velocity components are neglected) and only at the surface of the plate (which assumes that the vortices in the immediate vicinity of the plate are dominant in determining the downwash there). Thus, the shedding angle is interpreted as the angle at which the vortices leave the plate initially.

Two limiting cases are considered by Bollay in Reference 1. For the case of infinite aspect ratio (which actually violates the assumptions of the analysis), the normal force is found to be independent of the shedding angle θ and is given by

$$C_{N_{A \to \infty}} = 2\pi \sin \alpha \cos \alpha \qquad (3)$$

which, surprisingly enough, agrees with the Prandtl wing theory. In the second limiting case of vanishing aspect ratio, the shedding angle θ is found to be just half the angle of attack (for small α), and the resulting expression for the normal force coefficient is

$$C_{N_{A \to 0}} = 2 \sin^2 \alpha \qquad (4)$$

which is identical with the result of Newtonian impact theory.
The same result was also obtained by Betz (Ref. 2) in 1935 by
introducing the "cross-flow drag" concept and using the experi-
mental drag coefficient for a two-dimensional flat plate.

The theory of Bollay is limited to rectangular wings of small
aspect ratio in incompressible flow and is not suited to the calcu-
lation of quantities other than normal force. However, the agree-
ment between the calculated and measured normal forces is excellent
at very low aspect ratios up to angles of attack of about 40°.
Furthermore, the predicted normal forces for high aspect ratios
$(A \approx 6)$ agree with experiment within about 20 percent for angles
of attack below the stall. The stalling phenomenon for high aspect
ratios is clearly contrary to the assumed mathematical model.

A few years after the appearance of Bollay's paper, a theo-
retical analysis was published by F. Weinig (Ref. 3) whose aim was
to extend the Prandtl wing theory down to lower aspect ratios.
Weinig observed that for small-aspect-ratio wings the apparent
mass of air which is deflected downward by the wing is greater than
that which results from lifting line theory with elliptic lift dis-
tribution. According to lifting line theory, this mass would corre-
spond to the mass of a cylinder of air having a diameter equal to
the span. Weinig's innovation was twofold: first, he considered
the actual projected area of the wing $(S \sin \alpha)$ so that the
mass of air deflected downward per unit time is given by

$$m = \rho V_{\infty}(\pi s^2 + S \sin \alpha) \qquad (5)$$

where s is the semispan and S the planform area; and second,
he introduced a novel method, based on cascade theory, for calcu-
lating the induced downwash associated with this mass.

In this manner, Weinig developed a theory for the lift and
drag of small-aspect-ratio wings which is considerably simpler
than Bollay's theory from a mathematical standpoint and which gives

identical results (Eqs. (3) and (4)) for the limiting cases of infinite and zero aspect ratio. The agreement with experiment for nonvanishing aspect ratios, however, is not quite as good as for Bollay's theory.

2.1.2 Intermediate aspect ratio

More recently, K. Gersten (Ref. 4) presented an analytical method for extending linear lifting surface theory down to lower aspect ratios by incorporating the low aspect ratio results of Bollay. That is, Gersten allows the trailing vortices of each elementary horseshoe vortex to be shed above the plane of the wing. Thus, the actual wing is considered as made up of a number of Bollay-type wings placed side by side and it is assumed that the shedding angle of all the horseshoe vortices remains constant at the limiting value of $\alpha/2$ found by Bollay for vanishing aspect ratios and angles of attack. Gersten's model therefore has vortices shed over the entire wing surface.[2] In order to make the problem mathematically tractable, Gersten then divided the wing into a finite number of spanwise strips, concentrated the lifting line of each strip at the quarter chord, and proceeded to satisfy the boundary condition of no flow through the wing at the corresponding three-quarter chord of each strip. Thus, Gersten's mathematical model consists of a discrete number of lifting lines, each having an unspecified spanwise loading and shedding a flat, continuous vortex sheet at half the angle of attack, as shown below:

---

[2]This type of vortex shedding is incompatible with the physical requirement that the vortices follow the local streamlines, which must lie in the surface of the wing. (See discussion on page 16.)
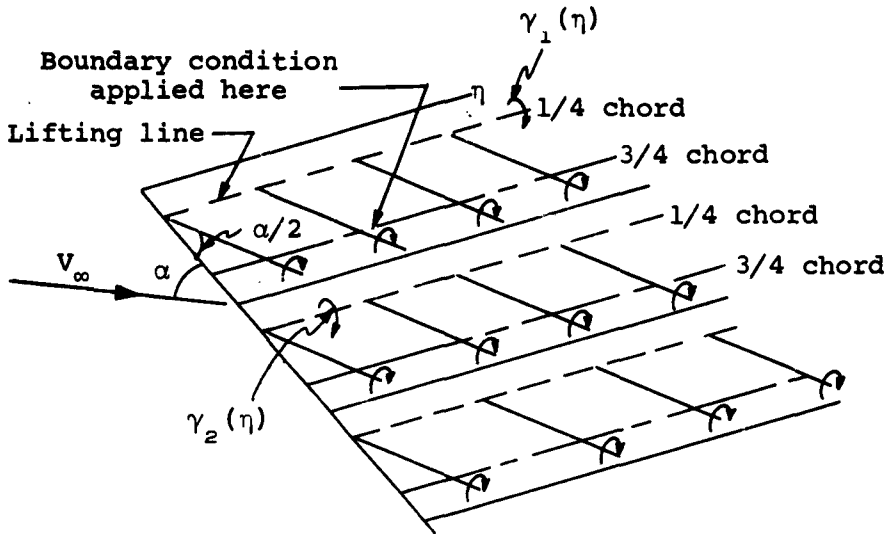
Mathematically, then, Gersten represents the spanwise circulation distribution of each lifting line as a sine series and, by applying the boundary condition at discrete points on each 3/4-chord line, is led to a set of simultaneous algebraic equations for the unknown coefficients. In arriving at these equations, Gersten further assumed that the angle of attack is small and neglected higher order terms in angle of attack. Then, the normal force and the pitching moment can be represented as

$$N = N_{\text{linear theory}} + N_{\text{sep}}$$

$$= k_1 \alpha + k_2 \alpha^2 \tag{6}$$

and

$$M = k_3 \alpha + k_4 \alpha^2 \tag{7}$$

so that the solution of Reference 4 is actually made up of the linear theory of Scholz (Ref. 5) plus a quadratic correction term which is determined from the analysis and stems from the fact that the trailing vortices do not lie in the plane of the wing.

It is clear that the above model does not reduce to Bollay's model for very low aspect ratios. In fact at aspect ratio zero, Gersten's model yields a coefficient of 3.2 for the quadratic term in the normal force, as compared with Bollay's value of 2.0. Gersten's mathematical procedure is by nature restricted to small angles of attack, but appears to give an improvement over Bollay's theory for the aspect ratio range from 2 to 4 for angles of attack up to about 15°. In addition, Gersten's analysis is suited to the calculation of load distribution and pitching moment in addition to lift and drag.

2.1.3 High aspect ratio

For aspect ratios of the order of 5 or 6 and above, with rounded wing tips, the flow over the wing remains attached up to the stall. Below the stall, the classical lifting line theory applies and the lift curve is essentially linear. The stall itself becomes more abrupt as the aspect ratio increases and does not behave according to the steady-flow models proposed by Bollay and Gersten. Instead, additional vortices which are aligned normal to the stream direction begin shedding from the leading and trailing edges, and the flow becomes unsteady. The problem then becomes the bluff body problem, which remains one of the classical unsolved problems of aerodynamics. There is, therefore, as yet no satisfactory theory for treating high-aspect-ratio wings above the stall angle, which is well defined experimentally. However, there has been some interesting analytical work related to this problem (Refs. 6 and 7) which employs the classical integral-differential equation of Prandtl lifting-line theory. The essential contribution of this work is a demonstration that if the airfoil section is assumed to have a lift curve which shows discontinuities or

negative slopes (which are typical of the stall), then the Prandtl
equation yields asymmetric solutions for the span loading and
therefore predicts the possibility of large rolling moments asso-
ciated with the stall. The thesis work of Schairer (Ref. 7) treats
a specific case of a discontinuous lift curve, as shown in the
following sketch:
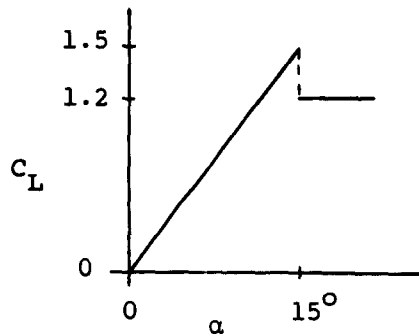
2.2 Triangular Wings

The theory of Brown and Michael (Ref. 8) contains the essential
elements of a number of recent papers (e.g., Refs. 9, 10, and 11)
which collectively represent the present status of the mathematical
analysis of highly swept wings with leading-edge separation. The
analysis is confined to triangular wings of low aspect ratio and
makes use of the slender-body approximation. With this approxi-
mation, the total lift is given by (see Ref. 12)

$$L = -\rho V_\infty \oint_c \phi \, dy \qquad (8)$$

where the contour c encloses the trailing-edge cross section of
the wing and the vortex sheets. Thus, the lift is linear in the
potential ϕ and is therefore composed of two parts; one being

the usual slender-body lift (which is linear in α), and one being the additional lift due to the potential associated with the separated vortices.

The model proposed by Brown and Michael is illustrated in the following sketch:
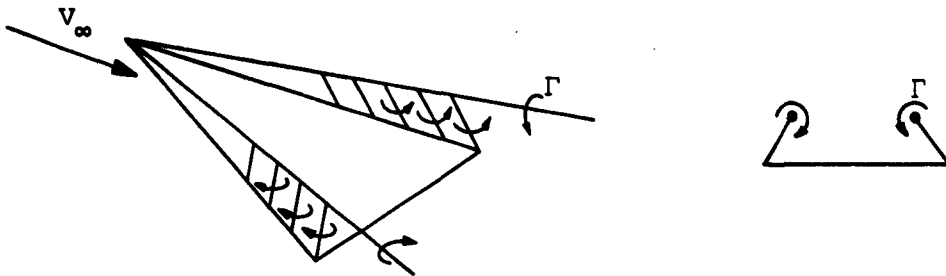
It is assumed that all of the trailing vorticity above the wing is concentrated in two fully rolled-up vortices whose strengths vary linearly in the chordwise direction. The contribution of the feeding vortex sheets (between the wing leading edges and the rolled-up vortices) to the complex potential in the cross-flow plane is neglected. However, since the feeding vortices shed from the leading edge lie almost normal to the free stream (rather than along the streamlines) they must sustain a force. The condition that the shed vortex system be force-free everywhere is therefore approximated by requiring that the net force on the entire vortex system be zero. In this manner, with the Kutta condition imposed at the leading edges, Brown and Michael proceed to solve for the vortex strengths Γ and the vortex positions, and thereby calculate the total lift and drag, as well as the spanwise load distribution[3].

---

[3]A similar analysis has been applied by Cheng (Ref. 13) to the corresponding problem of a rectangular wing with side-edge separation in supersonic flow. Here the separation effects are confined to the tip region within the Mach cone.

The lift curve calculated by the above method agrees well with experiment only for extremely low-aspect ratios (small apex angles) and the predicted high peaks in the pressure distribution are not realized because the streamwise vorticity is actually distributed through the feeding sheet rather than being concentrated in two discrete vortices.

A somewhat more general treatment of the slender triangular wing with leading-edge separation has been developed by Mangler and Smith (Ref. 14) who consider a more realistic shape of the vortex sheets and calculate the lateral distribution of streamwise circulation within the sheet, accounting approximately for the requirement of no force on the sheet and no flow through it. (See sketch.)

However, the severe limitation on aspect ratio remains.

2.3 Sweptback Wings

In Reference 15, Pappas and Kunen treated the high-aspect-ratio swept wing by what is essentially simple sweep theory with a single concentrated vortex representing the leading-edge separation. Thus, the flow in planes normal to the leading edge is treated as shown in the sketch below.
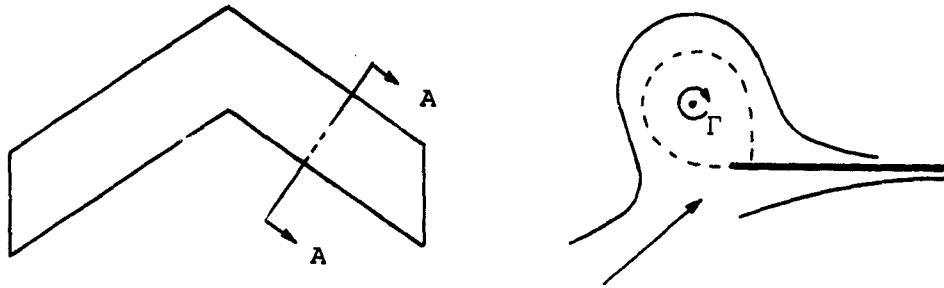
Section A-A

and the lift and drag of the airfoil section are calculated by the
two-dimensional Blasius theorem involving the complex potential
in the plane A-A. This treatment is similar to the slender-body
analysis of Brown and Michael (Ref. 8) for the slender delta wing
where the two-dimensional flow in the cross-flow plane is calcu-
lated. Hence, there are similar drawbacks to the analysis of Pappas
and Kunen (Ref. 15) who calculate the separation vortex strength
Γ from the experimentally determined vortex position over the swept
wing. That is, the separated vortex strength Γ must actually
vary spanwise over the sweptback wing. Therefore, there must be
a feeding vortex sheet connecting the separated vortex with the
wing leading-edge, and the force acting on this sheet plus the
separated vortex must be set to zero. This was not done in Ref-
erence 15. However, good agreement with experiment was demonstrated
for the calculated span load distribution over the inner half of
the span for the case of a 45° swept wing at 10° angle of attack.

The theory of Reference 15 is clearly restricted to high
aspect ratios and does not apply over the outboard sections of
the wing, where the flow pattern is quite different from the
assumed two-dimensional model. Pappas and Kunen suggest using
experimental stalled-airfoil data in the tip regions.

Just in the past year, an attempt has been made to treat
sweptback wings of arbitrary aspect ratio with flow separation.
This analysis (Ref. 16) by Gersten represents a natural extension
of his rectangular wing analysis (Ref. 4) which was discussed in
Section 2.1.2. In Reference 16, however, the Bollay model is com-
bined with the lifting surface model of Truckenbrodt (Ref. 17) to
produce a wing element with side-edge separation. That is, the
trailing portion of the horseshoe vortices making up each chord-
wise strip in the lifting surface theory are permitted to drift
above the wing surface at half the angle of attack. Thus, Gersten
again permits vortex shedding over the entire wing surface. In
Reference 16, as in Reference 4, the normal force is expressed as
a linear term plus a quadratic term, the former now being given
by the lifting surface theory of Truckenbrodt. The chordwise
loading is assumed to be given by the first two terms of the
Birnbaum series, and the boundary condition of no flow through
the wing is satisfied at both the quarter-chord and the wing
trailing edge.

In this manner, Gersten has built up a model of arbitrary
planform and aspect ratio with a solid wake of streamwise vorticity
forming an angle $\alpha/2$ above the plane of the wing (see sketch).
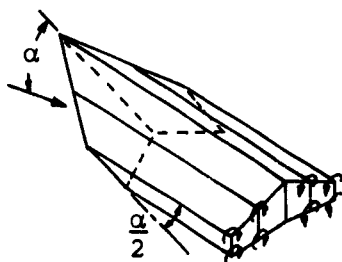
The agreement between theory and experiment for Gersten's model
appears to be satisfactory, although better agreement for swept
and delta wings of aspect ratios below unity is obtained with

Newtonian impact theory[4], and still better agreement for very low aspect ratio rectangular wings is obtained with the theory of Bollay (Ref. 1).

2.4 Summary of State of the Art

From the foregoing review of the analytical papers pertinent to the problem of wings with separated flow, it is apparent that the theory is lacking in several respects. With the exception of Reference 15 (which does not give total forces) and Reference 16 (which violates a fundamental boundary condition), the analytical work on sweptback wings with leading-edge separation has been confined to delta wings of extremely low aspect ratio and shows little improvement over the original slender-wing analysis of R. T. Jones (Ref. 18) insofar as the prediction of total aerodynamic forces is concerned, except for aspect ratios less than one. These theories do, however, give a more realistic prediction of the span loading on a very slender delta wing at moderate angles of attack, indicating the peaks under the separated vortices, as opposed to the elliptic span load distribution of the attached-flow solution of Jones.

For the rectangular wing, the theory of Bollay is similarly restricted to rather low aspect ratios but is valid up to high angles of attack and shows excellent agreement with the experimentally measured normal force on a rectangular wing of aspect ratio $A = 1/30$ up to an angle of attack of about 40°. If Bollay's theory is to be properly extended to higher aspect ratios, however, one must clearly abandon both the assumption of uniform span loading and that of the two-dimensional form of the chordwise loading. These steps were both taken by Gersten in References 4 and 16, but the resulting mathematical model violates certain physical requirements which are fundamental to the validity

---

[4] Vidya is publishing a separate report on this subject, Vidya Report No. 92 by Sacks and Burnell, dated March 30, 1963.

of the results. The agreement of Gersten's theory with experiment,
which extends only to moderate angles of attack, must therefore
be considered fortuitous.

The objections to Gersten's model can most easily be under-
stood if we consider the physical problem in somewhat greater
detail. Perhaps the most basic observation is that there can be
no flow of fluid through a solid surface. Thus, a boundary con-
dition on the mathematical problem is that the normal component
of velocity at the wing surface must be zero[5]. In other words,
the wing is a stream surface and the streamlines must lie in the
surface of the wing except at points of flow separation. Further,
according to Helmholtz's law of vortex motion, a free vortex must
follow the streamlines. Therefore, vortices can be shed only
along lines of flow separation. For the sharp-edged flat plate,
the lines of flow separation coincide with the edges of the plate,
and vortex shedding can therefore occur only along the sharp
edges! It can be seen that the mathematical model postulated by
Gersten implies an arbitrary number of spanwise lines of flow
separation over the upper surface of the wing and is evidently
unacceptable. Bollay's model, on the other hand, permits flow
separation only along the side edges. It should also be pointed
out that in both of these models it has been assumed that all of
the vorticity is shed out of the plane of the wing. This means
that there are no chordwise vortices in the plane of the wing and
hence there is no vortex sheet lying in the wing and shed at the
trailing edge! Because of this assumption, it was not necessary
in the analyses of References 1, 4, and 16, to impose the Kutta
condition along the side edges, since the velocities there were
necessarily finite. However, if chordwise vortices in the plane

---

[5]This boundary condition is ordinarily satisfied only at a finite
number of points on the wing surface (as in Ref. 4) or else in
the mean (as in Ref. 1).

of the wing are permitted, as they should be, then the Kutta condition must be imposed along the side edges to insure that the velocities there remain finite. This is equivalent to the physical requirement that the flow must separate tangentially at all sharp edges.

In the following sections, a new theory will be developed for rectangular wings with side-edge separation which will in fact satisfy these fundamental requirements and therefore will furnish a sound basis upon which we shall be able to develop a treatment for other planforms as well. The flow will be considered to be three-dimensional, so that no restriction on aspect ratio is implied.

3. APPROACH TO THE PROBLEM

The problem to be treated in the present analysis is that of a sweptback wing of arbitrary aspect ratio in incompressible flow with separation along the entire leading edge. Such flow separation is steady up to large angles of attack, depending upon the sweep angle, but is three-dimensional in character, becoming conical only for sweep angles near 90° (i.e., for vanishing aspect ratios). The use of strip theory in either the chordwise or spanwise direction is therefore not appropriate. However, if the trailing edge is straight, then we can represent a sweptback wing of arbitrary aspect ratio and rather general planform by a number of rectangular wing elements (see sketch), provided that each element satisfies the appropriate boundary and side-edge conditions.
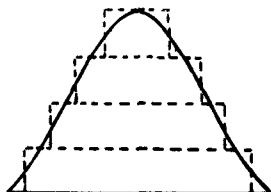
Since separation from the equivalent wing (composed of rec-
tangular elements) can occur only along its outline (i.e., along
its exposed edges), leading-edge separation can be permitted only
over the exposed portion of the span of each rectangular wing.
Furthermore, leading-edge separation from a rectangular wing occurs
at higher angles of attack and is essentially an unsteady phenomenon
in which the separated vortices are normal to the free stream and
are shed periodically. Therefore, for the purpose of treating the
present problem, flow separation will be permitted only along the
side edges of each rectangular wing element. Thus, as the number
of wing elements is increased, the mathematical approximation will
approach the physical problem of steady flow separation along a
sweptback leading edge (see sketch).
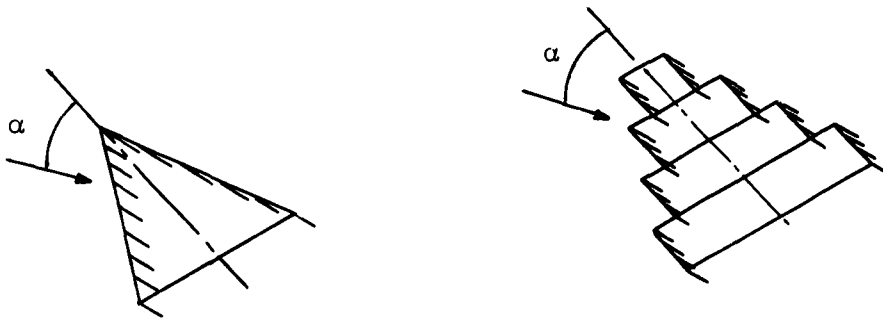
In the present analysis, each rectangular wing element will
be treated in the manner of classical lifting line theory, except
that side-edge flow separation will be included and the Kutta
condition will be satisfied along each side edge. This latter
point is essential to the success of the basic approach, since it
automatically removes the chordwise singularity in the downwash
along each side edge, which arises in Prandtl lifting line theory.
Only by the removal of these singularities can one safely super-
pose rectangular elements in the manner sketched above.

It should be noted that, since the rectangular wing is repre-
sented by a single lifting line (plus a separated vortex system),
one cannot expect an accurate prediction of the chordwise load
distribution or of the center of pressure. However, these details
can be obtained if desired by building up a rectangular wing with
a number of higher aspect ratio rectangular elements in the same
manner as for the swept wing (see sketch below).
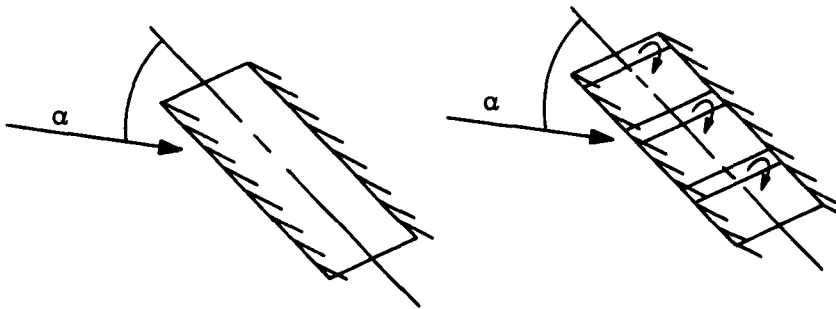
In the following section, the theoretical analysis will
first be developed for the basic rectangular wing with side-edge
flow separation. This analysis will then be applied to swept-
back wings with straight trailing edges by superposition, using
the rectangular wing as an elementary building block in the
manner described above. In addition, the extension of the analy-
sis to incorporate the influence of the ground plane will be
outlined in an appendix.

4. THEORY OF RECTANGULAR WINGS WITH SIDE-EDGE SEPARATION

4.1 Statement and Discussion of the Problem

The problem to be treated in this section is that of a rectangular wing element of arbitrary aspect ratio in incompressible flow with side-edge separation. Separation from the leading edge will not be considered, since it is intended to apply the theory later to sweptback wings, as explained in the previous paragraphs. Thus, the rectangular wing will be represented mathematically by (1) a lifting line of unspecif'ed spanwise circulation distribution $\gamma(\eta)$, (2) its associated trailing vortex sheet of strength $-(d\gamma/d\eta)\,d\eta$ lying <u>in the plane of the wing</u>, and (3) a continuous system of horseshoe vortices of strength $(d\Gamma/d\xi)\,d\xi$ representing the separated vortex system. This representation is shown schematically in Figure 1.

It is assumed that separation occurs all along the side edges and that all of the vortices shed from the side edges lie in the two planes containing the free-stream direction and the side edges, in the manner of Bollay. It is evident that the boundary conditions of no flow through the wing can be satisfied along a selected control line by a suitable choice of $\gamma(\eta)$ for any given $d\Gamma/d\xi$. Therefore, the Kutta condition of finite velocity at the side edges will have to be imposed to render $d\Gamma/d\xi$ (which will be assumed constant in the present analysis) unique. Here again, the justification for this assumption stems from the intended application to swept wings wherein $d\Gamma/d\xi$ may vary from one rectangular wing element to the next. Hence, the assumption that $d\Gamma/d\xi$ is constant on a given rectangular wing element is of no consequence in the swept wing problem.

Again, it is pointed out that the representation of the rectangular wing by a single lifting line (plus a separated vortex system of constant strength per unit length) may later be improved by the use of a number of such rectangular wing elements of higher aspect ratio, placed one behind the other.

Note that the above mathematical model satisfies the physical conditions discussed in Section 2.4 and differs from the models of Bollay (Ref. 1) and/or Gersten (Ref. 4) in the following important respects:

    (1)   The span load distribution is not specified.

    (2)   The appropriate streamwise vorticity in the plane of the wing is included. Thus there is a vortex sheet shed from the trailing edge.

    (3)   Vortex shedding occurs only at the side and trailing edges of the wing.

4.2 Analysis

4.2.1 Mathematical formulation of boundary-value problem

The mathematical equations to be solved for the above problem are actually those which express the boundary condition of no flow through the wing at each of a number of selected control points on the wing surface. Thus, if we express the upwash due to the lifting line and its trailing sheet in the plane of the wing as $w^*(x,y)$ and the upwash due to the horseshoe vortices of the separated system as $\bar{w}(x,y)$, then the boundary condition at a selected point (x_p, y_p) on the wing becomes

$$w^*(x_p, y_p) + \bar{w}(x_p, y_p) = -V_\infty \sin \alpha \qquad (9)$$

Ordinarily, this tangency condition of no flow through the wing is satisfied at a number of discrete points, and the number of simultaneous equations to be solved is then equal to the number of points selected. However, in the present analysis, we shall satisfy Equation (9) for each Fourier component. Thus, the number of simultaneous equations to be solved is equal to the number of terms taken in the Fourier analysis, and the boundary condition is satisfied, approximately, for all spanwise points along the selected control line[6].

---

[6]This method avoids the question of where control points should be located. Also its accuracy can be assessed by examining the size of subsequent Fourier terms.

The following analysis will therefore consist of setting up mathematical expressions for $w^*(x,y)$ and $\overline{w}(x,y)$, performing a Fourier analysis in a spanwise variable related to y, and substituting these expressions into Equation (9), which will then be satisfied for each Fourier component. Finally, the resulting set of simultaneous equations will be solved for the unknown Fourier coefficients of the expansion representing the spanwise circulation distribution $\gamma(\eta)$. Once this loading is obtained, the strength of the separated vortex system will be determined <u>uniquely</u> by imposing the Kutta condition along the side edges $y = \pm\, s$, and the resulting aerodynamic forces and moments will be calculated.

4.2.2 Velocity field of separated horseshoe vortex system

Each horseshoe vortex making up the separated vortex system is composed of three parts, a bound vortex in the wing and a left and a right trailing vortex lying at an angle θ above the wing. It is therefore convenient to write the corresponding upwash in the plane of the wing $w(x,y)$ in three parts as

$$\overline{w}(x,y) = \overline{w}_B(x,y) + \overline{w}_L(x,y) + \overline{w}_R(x,y) \tag{10}$$

The expression for each of these components at an arbitrary point in space has been derived in Appendix A for a single horseshoe vortex of strength Γ. Thus, replacing Γ in the expressions of Appendix A by $(d\Gamma/d\xi)\, d\xi$, setting z to zero, and integrating over the chord c, we have for the continuous vortex distribution representing the side-edge separation (see Fig. 1)

$$\overline{w}_B(x,y) = -\frac{1}{4\pi}\int_0^c \frac{(d\Gamma/d\xi)}{x-\xi}\left[\frac{s-y}{\sqrt{(x-\xi)^2+(s-y)^2}}+\frac{s+y}{\sqrt{(x-\xi)^2+(s+y)^2}}\right]d\xi$$

$$\overline{w}_L(x,y) = -\frac{(s+y)\cos\theta}{4\pi}\int_0^c \frac{(d\Gamma/d\xi)}{(x-\xi)^2\sin^2\theta+(s+y)^2}\left[1+\frac{(x-\xi)\cos\theta}{\sqrt{(x-\xi)^2+(s+y)^2}}\right]d\xi \quad (11)$$

$$\overline{w}_R(x,y) = -\frac{(s-y)\cos\theta}{4\pi}\int_0^c \frac{(d\Gamma/d\xi)}{(x-\xi)^2\sin^2\theta+(s-y)^2}\left[1+\frac{(x-\xi)\cos\theta}{\sqrt{(x-\xi)^2+(s-y)^2}}\right]d\xi$$

In the present analysis, we shall assume that $d\Gamma/d\xi$ is constant along the chord, which means that vortex shedding is uniform along the side edges. (In the case of the swept wing to be treated in Section 5, the values of θ and $d\Gamma/d\xi$ will be permitted to vary from one rectangular wing element to the next.) Thus, noting that the integral for $\overline{w}_B(x,y)$ is singular for $0 \le x \le c$ and taking the Cauchy principal value for that integral, we find upon integration

$\overline{w}_B(x,y)$

$$= -\frac{d\Gamma/d\xi}{4\pi}\log\left\{\frac{\frac{x^2}{s^2}\left[\frac{s-y}{s}+\sqrt{\left(\frac{x}{s}-\frac{c}{s}\right)^2+\frac{(s-y)^2}{s^2}}\right]\left[\frac{s+y}{s}+\sqrt{\left(\frac{x}{s}-\frac{c}{s}\right)^2+\frac{(s+y)^2}{s^2}}\right]}{\left(\frac{c}{s}-\frac{x}{s}\right)^2\left[\frac{s-y}{s}+\sqrt{\frac{x^2}{s^2}+\frac{(s-y)^2}{s^2}}\right]\left[\frac{s+y}{s}+\sqrt{\frac{x^2}{s^2}+\frac{(s+y)^2}{s^2}}\right]}\right\}$$

$$(12a)$$

$$\overline{w}_L(x,y) = -\frac{d\Gamma/d\xi}{4\pi}\, \text{ctn}\,\theta\left\{\tan^{-1}\left[\frac{\frac{s+y}{s}\sin\theta}{\left(\frac{x}{s}-\frac{c}{s}\right)-\cos\theta\,\sqrt{\left(\frac{x}{s}-\frac{c}{s}\right)^2+\frac{(s+y)^2}{s^2}}}\right]\right.$$

$$\left. -\tan^{-1}\left[\frac{\frac{s+y}{s}\sin\theta}{\frac{x}{s}-\cos\theta\,\sqrt{\frac{x^2}{s^2}+\frac{(s+y)^2}{s^2}}}\right]\right\} \tag{12b}$$

$$\overline{w}_R(x,y) = -\frac{d\Gamma/d\xi}{4\pi}\, \text{ctn}\,\theta\left\{\tan^{-1}\left[\frac{\frac{s-y}{s}\sin\theta}{\left(\frac{x}{s}-\frac{c}{s}\right)-\cos\theta\,\sqrt{\left(\frac{x}{s}-\frac{c}{s}\right)^2+\frac{(s-y)^2}{s^2}}}\right]\right.$$

$$\left. -\tan^{-1}\left[\frac{\frac{s-y}{s}\sin\theta}{\frac{x}{s}-\cos\theta\,\sqrt{\frac{x^2}{s^2}+\frac{(s-y)^2}{s^2}}}\right]\right\} \tag{12c}$$

These three expressions, then, represent the upwash at any point (x,y) in the plane of the wing due to the separated vortex system shown in Figure 1.

4.2.3 Velocity field of vortex system in wing surface

It will be convenient, as in classical lifting line theory (e.g., Ref. 19) to represent the unknown circulation distribution $\gamma(\eta)$ along the lifting line as a Fourier sine series of the form

$$\gamma(\eta) = \sum_{n=1,3,5--}^{\infty} \gamma_n \sin n\psi \tag{13}$$

where

$$\psi = \cos^{-1}\left(-\frac{\eta}{s}\right) \tag{14}$$

and

$$\gamma(-\psi) = -\gamma(\psi) \tag{15}$$

Thus, the wing lies in the interval $-s \leq \eta \leq s$ which corresponds
to $0 \leq \psi \leq \pi$. It can be seen that the series of Equation (13)
satisfies the requirement that γ be zero at the wing tips, regard-
less of how few terms are used in the series, and that the selected
series is even in η, which insures lateral symmetry.

If we consider now that the circulation distribution $\gamma(\eta)$
can be thought of as a large number of steps as shown in the sketch,
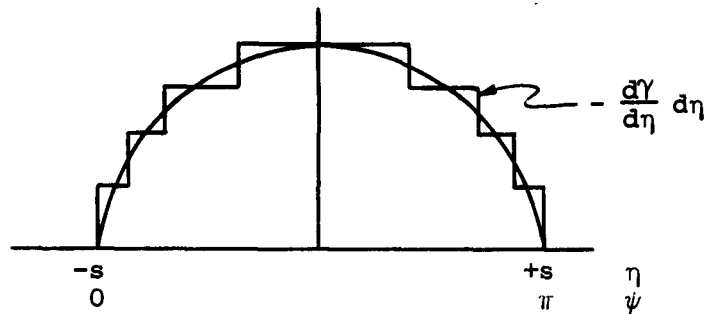
then it is clear that a vortex of strength $-(d\gamma/d\eta)\,d\eta$ must be
shed at each step and we can therefore construct the entire vortex
system in the plane of the wing from elementary horseshoe vortices
of semispan s_v and strength $-(d\gamma/d\eta)\,d\eta$ as shown below:
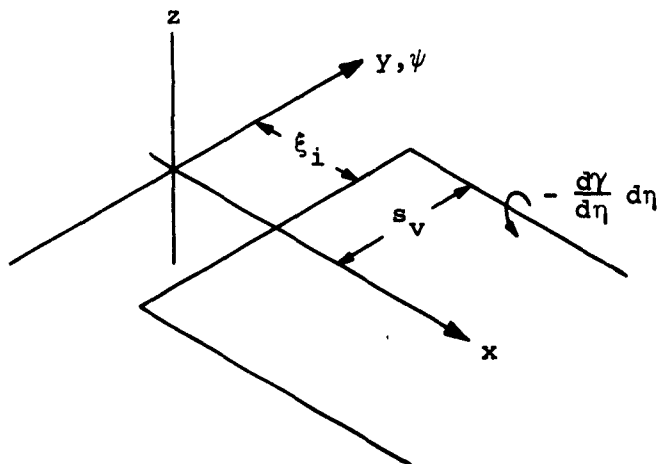
Thus, if we represent the upwash (in the plane of the wing) due to an elementary horseshoe vortex of unit strength as w_v, we have for the total upwash at a point (x,y) on the wing due to the entire vortex system in the plane of the wing

$$w^*(x,y) = -\int_0^s w_v(x,y,\xi_i,s_v)\,\frac{d\gamma}{d\eta}\,d\eta \qquad (16)$$

Upon introducing Equation (13) for $\gamma(\eta)$ and interchanging the order of integration and summation, we have

$$w^*(x,y) = -\sum_{n=1,3,5--}^{\infty} n\gamma_n \int_{\pi/2}^{\pi} w_v(x,y,\xi_i,s_v)\,\cos n\psi\,d\psi$$

$$(17)$$

Now we can employ the expressions of Appendix A for the upwash w_v due to each elementary horseshoe vortex by setting $z = 0$ and letting

$$\Gamma = 1$$
$$\theta = 0$$
$$s_v = -s\cos\psi \qquad (18)$$

Thus we find from Equations (A.15) that

$$w_v(x,y,\xi_i,\psi) = -\frac{1}{4\pi}\,\frac{1}{(x-\xi_i)}\left[\frac{-(y+s\cos\psi)}{\sqrt{(x-\xi_i)^2+(y+s\cos\psi)^2}}\right.$$

$$\left.+\frac{(y-s\cos\psi)}{\sqrt{(x-\xi_i)^2+(y-s\cos\psi)^2}}\right]$$

$$-\frac{1}{4\pi}\left(\frac{1}{-y-s\cos\psi}\right)\left[1+\frac{x-\xi_i}{\sqrt{(x-\xi_i)^2+(y+s\cos\psi)^2}}\right]$$

$$-\frac{1}{4\pi}\left(\frac{1}{y-s\cos\psi}\right)\left[1+\frac{x-\xi_i}{\sqrt{(x-\xi_i)^2+(y-s\cos\psi)^2}}\right]$$

$$(19)$$

The total upwash w^* due to $\gamma(\eta)$ is therefore given by

$$\frac{w^*}{V_\infty}(x,y,\xi_i) = +\frac{1}{4\pi}\sum_{n=1,3,5}^{\infty}\frac{n\gamma_n/V_\infty}{x-\xi_i}\int_{\pi/2}^{\pi}\left[\frac{-(y+s\cos\psi)}{\sqrt{(x-\xi_i)^2+(y+s\cos\psi)^2}}\right.$$

$$+\left.\frac{y-s\cos\psi}{\sqrt{(x-\xi_i)^2+(y-s\cos\psi)^2}}\right]\cos n\psi\,d\psi$$

$$-\frac{1}{4\pi}\sum_{n=1,3,5}^{\infty}\frac{n\gamma_n}{V_\infty}\int_{\pi/2}^{\pi}\frac{1}{y+s\cos\psi}\left[1\right.$$

$$+\left.\frac{x-\xi_i}{\sqrt{(x-\xi_i)^2+(y+s\cos\psi)^2}}\right]\cos n\psi\,d\psi$$

$$+\frac{1}{4\pi}\sum_{n=1,3,5}^{\infty}\frac{n\gamma_n}{V_\infty}\int_{\pi/2}^{\pi}\frac{1}{y-s\cos\psi}\left[1\right.$$

$$+\left.\frac{x-\xi_i}{\sqrt{(x-\xi_i)^2+(y-s\cos\psi)^2}}\right]\cos n\psi\,d\psi \qquad (20)$$

Now it can be shown by a simple change of variable and algebraic manipulation that for odd values of n

$$\int_{\pi/2}^{\pi}\frac{\cos n\psi\,d\psi}{y-s\cos\psi} = \int_{0}^{\pi/2} - \frac{\cos n\psi\,d\psi}{y+s\cos\psi}$$

and

$$\int_{\pi/2}^{\pi}\frac{\sqrt{(x-\xi_i)^2+(-s\cos\psi+y)^2}}{(x-\xi_i)(-s\cos\psi+y)}\cos n\psi\,d\psi$$

$$= +\int_{0}^{\pi/2}\frac{\sqrt{(x-\xi_i)^2+(s\cos\psi+y)^2}}{(x-\xi_i)(-s\cos\psi-y)}\cos n\psi\,d\psi$$

$$\left.\right\} \qquad (21)$$

so that Equation (20) can be collapsed into two integrals over the larger interval of 0 to π. Thus, combining the four terms involving the square root, and making use of Equations (21), we find that Equation (20) can be written in the following form:

$$\frac{w^*}{V_\infty}(x,y,\xi_i) = -\frac{1}{4\pi}\sum_{n=1,3,5}^\infty \frac{n\gamma_n}{V_\infty}\left[\int_0^\pi \frac{\cos n\psi}{y+s\cos\psi}\,d\psi\right.$$

$$\left.+\int_0^\pi \frac{\sqrt{(x-\xi_i)^2+(y+s\cos\psi)^2}}{(x-\xi_i)(y+s\cos\psi)}\,\cos n\psi\,d\psi\right]$$

(22)

Both of the integrals in Equation (22) are improper (i.e., singular) integrals. However, if we replace the control-point variable y by $(-s\cos\psi_o)$, then we recognize the first integral as that of classical lifting-line theory. For points <u>within the span</u>, the value of this integral is (Ref. 19)

$$\int_0^\pi \frac{\cos n\psi\,d\psi}{\cos\psi - \cos\psi_o} = \frac{\pi\sin n\psi_o}{\sin\psi_o}$$

(23)

where

$$\cos\psi_o = -(y/s) \quad \text{and} \quad -1 \le (y/s) \le +1$$

The singularity of the second integral in Equation (22) can be removed by simply adding and subtracting a term. Thus

$$\int_0^\pi \frac{\sqrt{(x-\xi_i)^2+(y+s\cos\psi)^2}}{(x-\xi_i)(y+s\cos\psi)}\,\cos n\psi\,d\psi$$

$$= \int_0^\pi \left[\frac{\sqrt{(x-\xi_i)^2+(y+s\cos\psi)^2}-|x-\xi_i|}{(x-\xi_i)(y+s\cos\psi)}\right]\cos n\psi\,d\psi \pm \int_0^\pi \frac{\cos n\psi\,d\psi}{y+s\cos\psi}$$

(24)

where the lower sign applies if $(x-\xi_i) < 0$ (i.e., for points ahead of the lifting line) and we recognize that the last integral is identical with that of Equation (23). The remaining integral is non-singular and is furthermore recognizable as the integral giving the Fourier coefficients of a certain cosine series in ψ. That is, if we let

$$f\left(\psi, \psi_o, \frac{x-\xi_i}{s}\right) = \frac{1}{(\cos \psi - \cos \psi_o)}\left[\frac{\sqrt{\left(\frac{x-\xi_i}{s}\right)^2 + (\cos \psi - \cos \psi_o)^2}}{\left(\frac{x - \xi_i}{s}\right)} \mp 1\right]$$

$$= \sum_{n=o,1,2,\ldots}^{\infty} a_n\left(\frac{x - \xi_i}{s}, \psi_o\right) \cos n\psi \qquad (25)$$

where the lower sign again applies if $x - \xi_i < 0$, then

$$a_n\left(\frac{x - \xi_i}{s}, \psi_o\right) = \frac{2}{\pi} \int_o^{\pi} f\left(\psi, \psi_o, \frac{x - \xi_i}{s}\right) \cos n\psi \, d\psi \qquad (26)$$

and the resulting relation is

$$\int_o^{\pi} \frac{\sqrt{(x-\xi_i)^2 + (y+s \cos \psi)^2}}{(x-\xi_i)(y+s \cos \psi)} \cos n\psi \, d\psi = \frac{\pi}{2s} a_n\left(\frac{x-\xi_i}{s}, \psi_o\right) \pm \frac{\pi \sin n\psi_o}{s \sin \psi_o}$$

$$(27)$$

Substitution of Equations (23) and (27) into Equation (22) therefore yields the final expression for w^* (for points within the span) in the form

$$\frac{w^*}{V_\infty}\left(\frac{x-\xi_i}{s}, \frac{y}{s}\right) = -\frac{1}{4\pi} \sum_{n=1,3,5}^{\infty} \frac{n\gamma_n}{sV_\infty}\left[\frac{2\pi \sin n\psi_o}{\sin \psi_o} + \frac{\pi}{2} a_n\left(\frac{x-\xi_i}{s}, \psi_o\right)\right]$$

$$\text{for} \quad x - \xi_i > 0 \qquad (28a)$$

and

$$\frac{w^*}{V_\infty}\left(\frac{x-\xi_i}{s}, \frac{y}{s}\right) = -\frac{1}{4\pi}\sum_{n=1,3,5}^{\infty}\frac{n\gamma_n}{sV_\infty}\left[\frac{\pi}{2}a_n\left(\frac{x-\xi_i}{s}, \psi_o\right)\right]$$

$$\text{for } x - \xi_i < 0 \tag{28b}$$

The first term of Equation (28a) is that appertaining to a value of $(x - \xi_i)/s$ which is sufficiently far behind the lifting line that the upwash no longer depends on $(x - \xi_i)/s$. This is evidently twice the upwash at the lifting line itself.

It is instructive to look at the term $n = 1$ of the foregoing equations. The circulation distribution from Equations (13) and (14) is then

$$\gamma(\eta) = \gamma_1 \sin \psi = \gamma_1 \sqrt{1 - \eta^2/s^2} \tag{29}$$

so that the corresponding span loading is elliptical. Thus letting

$$f_n\left(\frac{x - \xi_i}{s}, \frac{y}{s}\right) = \frac{2\pi \sin n\psi_o}{\sin \psi_o} + \frac{\pi}{2}a_n\left(\frac{x - \xi_i}{s}, \psi_o\right) \tag{30}$$

we find that the upwash behind the lifting line is

$$\frac{w^*}{V_\infty}\left(\frac{x - \xi_i}{s}, \frac{y}{s}\right) = -\frac{\gamma_1}{4\pi sV_\infty}\cdot f_1\left(\frac{x - \xi_i}{s}, \frac{y}{s}\right) \tag{31}$$

Table I shows the variation of downwash $(-w^*/V_\infty)$ with longitudinal distance behind the lifing line in semispans and with lateral distance from the wake centerline in semispans. It is interesting to note that one semispan behind the lifting line, the downwash is still about 10 percent higher than its value infinitely far downstream (where $f_1 = 2\pi$) and that it is quite uniform across the span.

4.2.4 Solution of the boundary-value problem

The set of equations representing the present boundary value problem simply express the boundary condition that there can be no flow through the wing surface. Thus, having derived the mathematical expression for the normal velocity $\bar{w}$ due to the separation vortices and $w*$ due to the lifting line and its trailing sheet, we can express this condition as

$$\frac{w*}{V_\infty} (x_p, y_p) + \frac{\bar{w}}{V_\infty} (x_p, y_p) = - \sin \alpha \qquad (32)$$

That is, the velocity component normal to the wing surface due to all vortices must exactly cancel the normal component of the free-stream velocity. The point (x_p, y_p) is the point on the wing at which this condition is to be satisfied, and the number of equations to be solved for the unknown distribution $\gamma(\eta)$ is ordinarily equal to the selected number of control points. However, in the present analysis, we shall eliminate the dependence on y_p by Fourier analysis and thus satisfy Equation (32) for all y_p within the span at a specified control <u>line</u> $x = x_p$. The number of equations will therefore be equal to the number of Fourier components employed.

In order to expand $w*$ in a Fourier series of ψ_0, it is first convenient to note from the trigonometric identity (Ref. 20)

$$\sin mx \cos nx = \frac{1}{2} \sin(n + m)x - \frac{1}{2} \sin(n - m)x$$

that $\sin n\psi_0 / \sin \psi_0$ can be written in the form

$$\frac{\sin n\psi_0}{\sin \psi_0} = 1 + 2 \sum_{j=2,4,6}^{n-1} \cos j\psi_0 \; ; \quad -\pi \leq \psi_0 \leq \pi \qquad (33)$$

Therefore, we shall expand w^* and $\bar{w}$ in the form of cosine series in ψ_o. Furthermore, only even multiples of ψ_o can appear because of the required symmetry about the midspan $\psi_o = (\pi/2)$. Thus, we have, from Equations (28a) and (33), for a control line lying behind the lifting line,

$$\frac{w^*}{V_\infty} = -\frac{1}{4\pi} \sum_{n=1,3,5}^{\infty} \frac{n\gamma_n}{sV_\infty} \left[2\pi \left(1 + 2 \sum_{j=2,4,6}^{n-1} \cos j\psi_o \right) \right.$$
$$\left. + \frac{\pi}{2} \left(\sum_{j=0,2,4,6}^{\infty} a_{nj} \cos j\psi_o \right) \right] \tag{34}$$

The corresponding expression for $\bar{w}$ is therefore taken to be

$$\frac{\bar{w}}{V_\infty} = +\frac{1}{4\pi} \frac{(d\Gamma/d\xi)c}{V_\infty s} \sum_{j=0,2,4}^{\infty} g_j \cos j\psi_o \; ; \quad -\pi \leq \psi_o \leq \pi \tag{35}$$

Note that these series are unique since $w(\psi_o) = w(-\psi_o)$ by the choice of a cosine series, so that w is specified over the entire interval $-\pi \leq \psi_o \leq \pi$ although the wing span covers only the interval $0 \leq \psi_o \leq \pi$.

Substitution of Equations (34) and (35) into Equation (32) yields the set of equations to be solved for the unknown coefficients γ_n representing the circulation distribution

$$\gamma = \sum_{n=1,3,5}^{\infty} \gamma_n \sin n\psi$$

along the lifting line. The expanded form of Equation (32) thus becomes

$$\left(\frac{1\gamma_1}{4\pi sV_\infty}\right)\left[2\pi(1+0)+\frac{\pi}{2}(a_{10}+a_{12}\cos 2\psi_0+a_{14}\cos 4\psi_0+\ldots)\right]$$

$$+\left(\frac{3\gamma_3}{4\pi sV_\infty}\right)\left[2\pi(1+2\cos 2\psi_0)\right.$$

$$+\frac{\pi}{2}(a_{30}+a_{32}\cos 2\psi_0+a_{34}\cos 4\psi_0+\ldots)\bigg]$$

$$+\left(\frac{5\gamma_5}{4\pi sV_\infty}\right)\left[2\pi(1+2\cos 2\psi_0+2\cos 4\psi_0)\right.$$

$$+\frac{\pi}{2}(a_{50}+a_{52}\cos 2\psi_0+a_{54}\cos 4\psi_0+\ldots)\bigg]+\ldots$$

$$=\left[\frac{1}{4\pi}\frac{(d\Gamma/d\xi)c}{V_\infty s}\right](g_0+g_2\cos 2\psi_0+g_4\cos 4\psi_0+\ldots)+\sin\alpha$$

$$\tag{36}$$

Now, in order that this equation be satisfied for __all__ values of ψ_0 it must be satisfied for __each__ Fourier component. Therefore, if we let

$$\gamma_n{}^* = \frac{n\gamma_n}{4\pi sV_\infty\sin\alpha}$$

and

$$\Gamma^* = \frac{(d\Gamma/d\xi)c}{4\pi sV_\infty\sin\alpha} = \frac{d\Gamma/d\xi}{2\pi AV_\infty\sin\alpha}$$

$$\left.\begin{array}{c}\\\\\\\\\end{array}\right\}\tag{37}$$

the following set of equations results:

$$\underline{n=1}\qquad\underline{n=3}\qquad\underline{n=5}\qquad\underline{n=7}$$

$\underline{j=0}:\ \left(2\pi+\frac{\pi}{2}a_{10}\right)\gamma_1^*+\left(2\pi+\frac{\pi}{2}a_{30}\right)\gamma_3^*+\left(2\pi+\frac{\pi}{2}a_{50}\right)\gamma_5^*+\left(2\pi+\frac{\pi}{2}a_{70}\right)\gamma_7^*+\ldots=g_0\Gamma^*+1$

$\underline{j=2}:\ \left(\frac{\pi}{2}a_{12}\right)\gamma_1^*\ \ +\left(4\pi+\frac{\pi}{2}a_{32}\right)\gamma_3^*+\left(4\pi+\frac{\pi}{2}a_{52}\right)\gamma_5^*+\left(4\pi+\frac{\pi}{2}a_{72}\right)\gamma_7^*+\ldots=g_2\Gamma^*$

$\underline{j=4}:\ \left(\frac{\pi}{2}a_{14}\right)\gamma_1^*\ \ +\left(\frac{\pi}{2}a_{34}\right)\gamma_3^*\ \ +\left(4\pi+\frac{\pi}{2}a_{54}\right)\gamma_5^*+\left(4\pi+\frac{\pi}{2}a_{74}\right)\gamma_7^*+\ldots=g_4\Gamma^*$

$\underline{j=6}:\ \left(\frac{\pi}{2}a_{16}\right)\gamma_1^*\ \ +\left(\frac{\pi}{2}a_{36}\right)\gamma_3^*\ \ +\left(\frac{\pi}{2}a_{56}\right)\gamma_5^*\ \ +\left(4\pi+\frac{\pi}{2}a_{76}\right)\gamma_7^*+\ldots=g_6\Gamma^*$

$\underline{j=8}:\qquad\qquad\qquad\text{etc.}\qquad\qquad\qquad\qquad\tag{38}$

These equations can now be written in the following abbreviated form:

$$\sum_{n=1,3,5,\ldots}^{\infty} f_{nj}\gamma_n{}^* = g_j\Gamma^* + 1 \; ; \quad j = 0$$

$$\sum_{n=1,3,5,\ldots}^{\infty} f_{nj}\gamma_n{}^* = g_j\Gamma^* \; ; \quad j = 2,4,6, \ldots \tag{39}$$

where

$$f_{nj} = 2\pi + \frac{\pi}{2} a_{nj} \; ; \quad j = 0$$

$$\left. \begin{array}{ll} f_{nj} = \frac{\pi}{2} a_{nj} & n < j \\[2mm] f_{nj} = 4\pi + \frac{\pi}{2} a_{nj} & n > j \end{array} \right\} \quad j = 2,4,6, \ldots \tag{40}$$

The numbers denoted by f_{nj} are, then, universal numbers which can be used to obtain the loading coefficients $\gamma_n{}^*$ for any specified separated flow pattern as given by the coefficients g_j. The particular type of flow separation assumed here is shown in Figure 1 and the corresponding function $\overline{w}(x,y)$ is given by Equations (10) and (12).

In the asymptotic formulation for large distances behind the lifting line, all the coefficients a_{nj} become zero, (see Eqs. (25) and (26)) and the matrix of the foregoing infinite set of equations yields the following matrix of coefficients:

	n=1	3	5	7		
j = 0	2π	2π	2π	2π	. . .	
j = 2	0	4π	4π	4π	. . .	
j = 4	0	0	4π	4π	. . .	$= \left| f_{nj} \right|$
j = 6	0	0	0	4π	. . . .	

$$\tag{41}$$

Thus it is clear that in this case the determinant is not zero. Numerical calculations for other locations behind the lifting line indicate that this is in fact true in general. Therefore, there exists no nontrivial solution to the homogeneous set of equations $\Sigma\, f_{nj}\gamma_n{}^* = 0$, and the general solution of Equations (39) for the loading coefficients $\gamma_n{}^*$ can be represented as

$$\gamma_n{}^* = \left(\gamma_n{}^*\right)_u + \Gamma^* \left(\gamma_n{}^*\right)_S \qquad (42)$$

The first term $\left(\gamma_n{}^*\right)_u$ is the solution of the equations

$$\sum_{n=1,3,5}^{\infty} f_{nj}\gamma_n{}^* = 1 ; \quad (j = 0) \qquad (43)$$

$$\sum_{n=1,3,5}^{\infty} f_{nj}\gamma_n{}^* = 0 ; \quad (j = 2,4,6\ldots) \qquad (44)$$

which corresponds to no flow separation $(\Gamma^* = 0)$. On the other hand, $\left(\gamma_n{}^*\right)_S$ is the solution of the equations

$$\sum_{n=1,3,5}^{\infty} f_{nj}\gamma_n{}^* = g_j ; \quad (j = 0,2,4,6\ldots) \qquad (45)$$

which corresponds to the image system required for the separated flow $(\Gamma^* = 1)$. Thus for a given value of Γ^*, the general solution (which is unique) is given by Equation (42). The solution of Equation (45) is therefore seen to be the basic source of the change in the aerodynamic characteristics of the wing due to separation.

4.2.5 Satisfying the Kutta condition

In the foregoing solution, the value of Γ^* is a parameter which has not been specified, and a solution exists for each value of Γ^*. From this spectrum of solutions, it is desired to select the one corresponding to the value of Γ^* required on the basis of physical considerations. It turns out that it is possible to make the determination of Γ^* on the basis of the Kutta condition. The particular condition is that the downwash just off the side edges of the wing be finite rather than infinite. Thus, the flow at the side edge of the wing seen in end view leaves the side edges smoothly and (see sketch) does not turn around the sharp edges with a flow singularity.
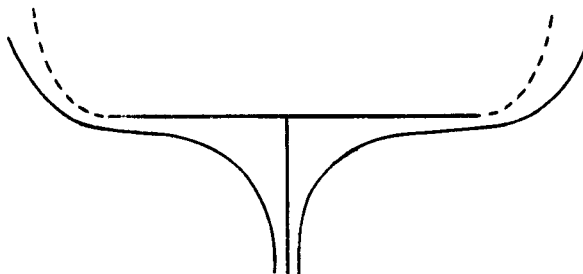
The mathematical requirement for the Kutta condition can be established by examining Equation (22) for points lying <u>outside</u> the span of the vortex sheet. For such points, by making use of Equations (24) and (25), we can write Equation (22) in the form

$$\frac{w^*}{V_\infty}(x,y,\xi_i) = -\frac{1}{4\pi}\sum_{n=1,3}^{\infty}\frac{n\gamma_n}{sV_\infty}\left[\frac{\pi}{2}\,a_n\left(\frac{x-\xi_i}{s},\frac{y}{s}\right) + 2\int_0^\pi\frac{\cos n\psi\,d\psi}{\cos\psi+\frac{y}{s}}\right]$$

(46)

where $x - \xi_i > 0$, since we need to satisfy the Kutta condition <u>behind</u> the lifting line only. Now, integration of the second term yields, for points outside the interval of integration (Ref. 21)

$$\int_0^\pi \frac{\cos n\psi \, d\psi}{\cos \psi + \frac{y}{s}} = \frac{\pi \left[\sqrt{\left(\frac{y}{s}\right)^2 - 1} - \left|\frac{y}{s}\right| \right]^n}{\sqrt{\left(\frac{y}{s}\right)^2 - 1}} \quad \text{for} \quad \left|\frac{y}{s}\right| > 1 \quad (47)$$

Thus, for points lying outside the span of the vortex sheet and behind the lifting line, the upwash w^*/V_∞ becomes

$$\frac{w^*}{V_\infty}(x,y,\xi_i) = -\frac{1}{4\pi} \sum_{n=1,3}^{\infty} \frac{n\gamma_n}{sV_\infty} \left\{ \frac{\pi}{2} a_n\left(\frac{x - \xi_i}{s}, \frac{y}{s}\right) \right.$$

$$\left. + \frac{2\pi \left[\sqrt{\left(\frac{y}{s}\right)^2 - 1} - \left|\frac{y}{s}\right| \right]^n}{\sqrt{\left(\frac{y}{s}\right)^2 - 1}} \right\} \quad (48)$$

Hence, the <u>singular</u> part of the upwash denoted by $(w^*/V_\infty)_\infty$ just outside the span is given by

$$\left(\frac{w^*}{V_\infty}\right)_\infty = -\frac{1}{2\pi sV_\infty} \sum_{n=1,3}^{\infty} n\gamma_n \frac{\pi \left[\sqrt{\left(\frac{y}{s}\right)^2 - 1} - \left|\frac{y}{s}\right| \right]^n}{\sqrt{\left(\frac{y}{s}\right)^2 - 1}} \quad (49)$$

An examination of this result reveals several very interesting facts. As we approach the side edges of the vortex sheet from outside the span of the vortex sheet, the downwash for each Fourier component has a square root singularity. Furthermore the coefficient of the singularity is independent of x so that the singularities have the same strength along the length of each side edge. It follows, therefore, that we can satisfy the Kutta condition <u>along the entire length of each side edge</u> if

$$\sum_{n=1,3,5}^{\infty} n\gamma_n = 0 \quad \text{or} \quad \sum_{n=1,3,5}^{\infty} \gamma_n^* = 0 \tag{50}$$

This is, therefore, the mathematical formulation of the Kutta condition[7].

From Equations (42) and (50), we can now determine the separated vortex strength Γ^* which is necessary to satisfy the Kutta condition. Thus, substituting Equation (42) into Equation (50), we have

$$\sum_{n=1,3,5,\ldots}^{\infty} \left(\gamma_n^*\right)_u + \Gamma^* \sum_{n=1,3,5,\ldots}^{\infty} \left(\gamma_n^*\right)_S = 0$$

or

$$\Gamma^* = \frac{-\sum_{n=1,3,5,\ldots}^{\infty} \left(\gamma_n^*\right)_u}{\sum_{n=1,3,5,\ldots}^{\infty} \left(\gamma_n^*\right)_S} \tag{51}$$

The final solution of the complete boundary-value problem of a rectangular wing with side-edge separation is therefore given by Equations (42) and (51), so that the loading coefficients of the lifting line are

---

[7] It can easily be shown that this condition is precisely the same as requiring that the loading $\gamma(\eta)$ must have a zero slope at the wing tips. But the slope of the loading is proportional to the strength of the trailing vortex sheet, so the Kutta condition is satisfied along the side edges if the trailing vortex sheet has zero strength at the edges.

$$\gamma_n{}^* = \left(\gamma_n{}^*\right)_u - \left(\gamma_n{}^*\right)_S \left[\frac{\displaystyle\sum_{n=1,3,5}^{\infty} \left(\gamma_n{}^*\right)_u}{\displaystyle\sum_{n=1,3,5}^{\infty} \left(\gamma_n{}^*\right)_S}\right] \tag{52}$$

It is clear from the foregoing analysis that there is only one correct solution for $\gamma_n{}^*$ in the given boundary-value problem[8]. That is, the solution is unique (for a specified θ), and there is only one correct value for Γ^* which satisfies the Kutta condition. One may well ask, then, what is the meaning of the so-called "unseparated" solution with $\Gamma^* = 0$? Clearly, this solution does not satisfy the Kutta condition at the side edges. Mathematically, it simply represents a portion of the complete solution of the stated boundary-value problem. But physically this "unseparated" solution actually represents the solution for which there is no side-edge separation. That is, the side edges are not sharp, and one therefore need not impose the Kutta condition. We have a different boundary-value problem, then, and the unseparated solution therefore corresponds to the classical wing theory of Prandtl, which applies to high aspect ratio wings at low angles of attack.

4.2.6 Determination of the shedding angle θ

The orientation of the vortex lines which comprise a free vortex sheet is determined by the average of the velocity vectors on the two sides of the sheet. This follows from the Helmholtz law that a free vortex must follow the local streamlines. Therefore, we can determine the inclination, or shedding angle, θ, of the side-edge vortex sheets by calculating the total velocity components just above the wing on either side of the sheet. Thus (see sketch),

---

[8]Note that the determination of <u>each</u> loading coefficient for the complete problem requires the determination of <u>all</u> of the loading coefficients from the homogeneous and the nonhomogeneous solutions.
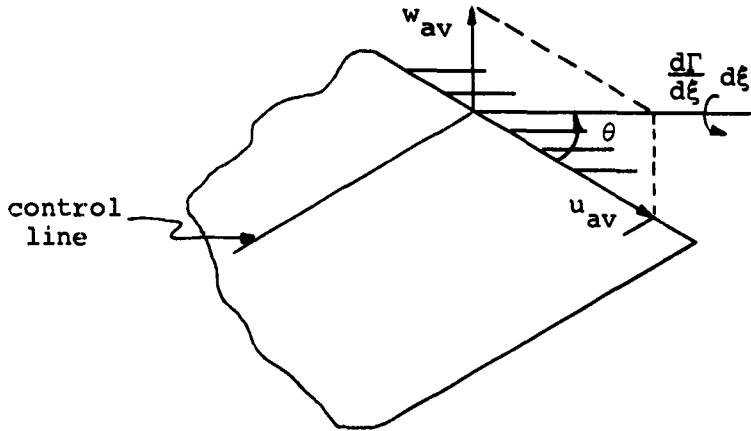
$$\tan \theta = \frac{w_{av}}{u_{av}} = \left\{ \frac{\frac{1}{2}\left[\left(\frac{w^{\star}}{V_{\infty}} + \frac{\overline{w}}{V_{\infty}} + \sin\alpha\right)_{y=s+\epsilon} + \left(\frac{w^{\star}}{V_{\infty}} + \frac{\overline{w}}{V_{\infty}} + \sin\alpha\right)_{y=s-\epsilon}\right]}{\frac{1}{2}\left[\left(\frac{u^{\star}}{V_{\infty}} + \frac{\overline{u}}{V_{\infty}} + \cos\alpha\right)_{y=s+\epsilon} + \left(\frac{u^{\star}}{V_{\infty}} + \frac{\overline{u}}{V_{\infty}} + \cos\alpha\right)_{y=s-\epsilon}\right]} \right\}_{z=o+\epsilon}$$

(53)

Since w and u are both functions of θ, the determination of θ will require an iterative process in which a value of θ is assumed, the right-hand side of Equation (53) is calculated and compared with the assumed value of θ, the right-hand side is recalculated using the new value of θ, and so on. The procedure is analogous to that employed by Bollay (Ref. 1).

Since the boundary condition of no flow through the wing has been satisfied only at one chordwise location (i.e., at the control line), we shall solve Equation (53) for θ at the control line also. At this location, the boundary condition requires that

$$\left(\frac{w^{\star}}{V_{\infty}} + \frac{\overline{w}}{V_{\infty}} + \sin\alpha\right)_{y=s-\epsilon} = 0 \tag{54}$$

Now, since the singular part of w* just outside the span has been removed by imposing the Kutta condition of Equation (50), the value of w* at $y = s + \epsilon$ is given by (see Eq. (28))

$$\left(\frac{w^*}{V_\infty}\right)_{y=s+\epsilon} = -\frac{1}{4\pi} \sum_{n=1,3,5}^{\infty} \frac{n\gamma_n}{sV_\infty} \left[\frac{\pi}{2} a_n \left(\frac{x - \xi_i}{s}\right)\right]_{y=s} \tag{55}$$

and it is noted that a_n is continuous across the vortex sheet. The value of $\bar{w}$ just beyond the wing tip can be found simply from Equation (12c) by noting that as we pass from $y = s - \epsilon$ to $y = s + \epsilon$ the second arc tangent in that equation jumps from 0 to 2π, while the first arc tangent remains at π. That is, the last term of Equation (12c) is discontinuous as y moves across the vortex sheet, and we find that $\bar{w}_R$ simply changes sign across the sheet. Therefore, we can write $\bar{w}$ just outside the span in the form

$$\bar{w}_{y=s+\epsilon} = \bar{w}_{y=s-\epsilon} - 2\bar{w}_{R_{y=s-\epsilon}}$$

$$= \bar{w}_{B_{y=s}} + \bar{w}_{L_{y=s}} - \bar{w}_{R_{y=s-\epsilon}} \tag{56}$$

Inasmuch as the vortex sheet lying in the plane of the wing consists of a single vortex line ahead of the control line and a system of chordwise trailing vortices, this vortex system produces no chordwise velocity component at the control line. Therefore

$$\left(\frac{u^*}{V_\infty}\right)_{y=s-\epsilon} = \left(\frac{u^*}{V_\infty}\right)_{y=s+\epsilon} = 0 \tag{57}$$

Also, it can be seen from Appendix A that the chordwise components of velocity due to the side-edge vortex sheets are directly related to the corresponding upwash in the following manner:

$$\left.\begin{array}{l} \bar{u}_R = -\bar{w}_R \tan\theta \\[2mm] \bar{u}_L = -\bar{w}_L \tan\theta \end{array}\right\} \tag{58}$$

(Note that $\bar{u}$ changes sign with $\bar{w}$ as we cross the vortex sheet.) The chordwise velocity component produced by the bound portion of the separated vortices can be obtained from Appendix A. Thus, replacing Γ by $(d\Gamma/d\xi)\, d\xi$ and integrating over the chord, we find that

$$\bar{u}_B = \frac{zs}{2\pi}\ \frac{d\Gamma}{d\xi}\ \int_0^c \frac{d\xi}{\left[(x - \xi)^2 + z^2\right]\ \sqrt{(x - \xi)^2 + 4s^2 + z^2}} \tag{59}$$

Now, integrating this expression (Ref. 21) and taking the limit as $z \to 0$ from the positive direction, to find the induced chordwise velocity component immediately above the wing surface, we obtain

$$\bar{u}_{B_{z=o+\epsilon}} = \frac{d\Gamma/d\xi}{4} = \frac{\pi}{2}\ A\Gamma^* V_\infty \sin\alpha \tag{60}$$

Finally, substitution of Equations (54) through (60) into Equation (53) yields the following expression for the shedding angle:

$$\tan\theta = \frac{1}{2}\ \frac{\left(\dfrac{\overline{w}_B + \overline{w}_L}{V_\infty \sin\alpha}\right)_{y=s} - \left(\dfrac{\overline{w}_R}{V_\infty \sin\alpha}\right)_{y=s-\epsilon} - \dfrac{\pi}{2}\ \displaystyle\sum_{n=1,3}^{\infty} \gamma_n^* a_n + 1}{\dfrac{\pi}{2}\ A\Gamma^* - \left(\dfrac{\overline{w}_L}{V_\infty \sin\alpha}\right)_{y=s}\ \tan\theta + \operatorname{ctn}\alpha} \tag{61}$$

It is noted that Bollay (Ref. 1) obtained a value of θ equal to half the angle of attack for the limiting case of vanishing aspect ratio at small angles of attack. In the more general case (Eq. (61)), the ratio of θ/α will be a function of both aspect ratio and angle of attack.

4.3 Normal Force and Center of Pressure

According to the Kutta-Joukowski law, the normal force acting on the lifting line of circulation strength $\gamma(\eta)$ is given by

$$N_l = \rho V_\infty \cos \alpha \int_{-s}^{+s} \gamma(\eta) \, d\eta \tag{62}$$

so that, with the definitions of Equations (13) and (14), we find that

$$N_l = \rho V_\infty \cos \alpha \int_0^\pi \left(\sum_{n=1,3,5}^\infty \gamma_n \sin n\psi \right) (s \sin \psi \, d\psi)$$

$$= \rho V_\infty \, s \cos \alpha \left(\frac{\pi}{2} \right) \gamma_1$$

$$= 2\pi^2 \rho V_\infty^2 s^2 \cos \alpha \sin \alpha \left(\gamma_1^* \right) \tag{63}$$

Thus, only γ_1^* contributes to the normal force, whereas the higher harmonics affect only the span load distribution. The load distribution associated with γ_1^* is elliptical, but its magnitude will be affected by the existence of the higher harmonics.

For the unseparated case $(\Gamma^* = 0)$, we have for the normal force coefficient

$$\left(C_N \right)_u = \frac{N_u}{(1/2)\rho V_\infty^2 (2 \, sc)} = \pi^2 A \left(\gamma_1^* \right)_u \cos \alpha \sin \alpha \tag{64}$$

For small aspect ratios, the lifting line and the line of control points may be separated by many semispans so that $(x - \xi_i)/s$ is large. Thus, $(\gamma_1^*)_u$ approaches its asymptotic value of $1/(2\pi)$ and we have

$$\left(C_N \right)_{u_{A \to 0}} = \frac{\pi}{2} A \sin \alpha \cos \alpha \tag{65}$$

This result agrees with the slender-body result for the normal force coefficient of a rectangular wing of low aspect ratio at low angles of attack.

The total normal force acting on the wing with flow separation is the sum of the normal force on the lifting line N_l (including the image system $(\gamma_n{}^*)_S$) and the normal force acting on the bound vortices of the separated system (which have uniform span loading). Thus, using Equations (37), (42), (62), and (63), we have for the total normal force

$$N = \rho V_\infty \cos \alpha \left[\int_{-s}^{+s} \gamma(\eta) \, d\eta + 2s \cdot \frac{d\Gamma}{d\xi} \cdot c \right]$$

$$= 2\pi^2 \rho V_\infty{}^2 s^2 \cos \alpha \sin \alpha \left[\left(\gamma_1{}^*\right)_u + \Gamma^* \left(\gamma_1{}^*\right)_S \right]$$

$$+ 2\rho V_\infty sc \cos \alpha (2\pi A V_\infty \sin \alpha \cdot \Gamma^*) \tag{66}$$

The total normal force coefficient C_N is therefore given by

$$C_N = \frac{N}{\frac{1}{2} \rho V_\infty{}^2 (2sc)} = \frac{\pi}{2} A \cos \alpha \sin \alpha \left\{ 2\pi \left(\gamma_1{}^*\right)_u + \Gamma^* \left[2\pi \left(\gamma_1{}^*\right)_S + 8 \right] \right\}$$

$$= C_{N_u} + C_{N_S} \tag{67}$$

where

$$C_{N_S} = \frac{\pi}{2} A \cos \alpha \sin \alpha \cdot \Gamma^* \left[2\pi \left(\gamma_1{}^*\right)_S + 8 \right] \tag{68}$$

represents the normal force due to the separated vortices and their images.

The center of pressure is obtained by noting that the loadings due to $(\gamma_1{}^*)_u$ and to $(\gamma_1{}^*)_S$ both act on the lifting line (i.e., at the quarter chord), whereas that due to Γ^* acts at

the half chord, since $d\Gamma/d\xi$ was taken as constant. Thus we can write at once, from Equation (67)

$$\frac{\overline{x}}{c} = \frac{\frac{1}{4}\left(\gamma_1^*\right)_u + \frac{1}{4}\Gamma^*\left(\gamma_1^*\right)_S + \frac{1}{2}\left(\frac{4}{\pi}\right)\Gamma^*}{\left(\gamma_1^*\right)_u + \Gamma^*\left(\gamma_1^*\right)_S + \frac{4}{\pi}\Gamma^*} \qquad (69)$$

The foregoing solution also yields a precise determination of the proper location of the control line if the present theory is to yield results in accordance with experiment for small angles of attack. To demonstrate this fact, let us calculate the lift-curve slope at zero angle of attack as a function of aspect ratio and position of the control line. By comparing these results with those from experiment or exact theory, it can be determined where the control line should be placed as a function of aspect ratio.

The lift-curve slope at zero angle of attack has been computed as a function of aspect ratio using Equation (67). Note that

$$\left(\frac{\partial c_{N_S}}{\partial \alpha}\right)_{\alpha=0} = 0$$

since there is no flow separation at zero angle of attack. The results are shown in Figure 2 for several chordwise positions of the control line with the lifting line placed at the quarter-chord position. They are also compared with the mean experimental curve of Scholz (Ref. 5). It is seen that locating the control line at the three-quarter-chord position yields excellent agreement between the present theory and experiment for unseparated flows. The use of a control line at the half-chord position yields values of lift-curve slope about 10 percent low at an aspect ratio of unity and 25 percent low at $A = 2$. These results are in substantial agreement with the classical work of Weissinger (Ref. 22) which was evidently based on his observation that the influence of

the semi-infinite trailing vortices varies very little over the airfoil chord, so the influence of the bound vortex is dominant in determining the proper placement of the control line. The present calculations take the trailing vortices fully into account and therefore serve to substantiate Weissinger's conclusion.

4.4 Downwash at the Tail Location

In order to investigate longitudinal stability and control characteristics of an aircraft configuration, one must determine the downwash at the location of the horizontal tail. This is a relatively straightforward procedure once the strengths and positions of the vortices shed from the wing are known. Thus, the upwash at any point in space is given by

$$w(x,y,z) = w^* + \overline{w} + V_\infty \sin \alpha$$

and the expressions for w^* and $\overline{w}$ for points lying <u>in the plane of the wing</u> are given by Equations (12) and either (28) or (48), depending upon whether the point in question lies <u>inside</u> or outside of the wing span.

The determination of the upwash w^* and $\overline{w}$ for points lying <u>out of the plane of the wing</u> is clearly not covered by Equations (12), (28), and (48), since they were specialized by setting $z = 0$. Therefore, one must start with the more general expressions of Appendix A for the single vortex and develop expressions analogous to Equations (12), (28), and (48) for $z \neq 0$. The procedure is exactly parallel to that of Section 4.2 of the present report. However, the resulting expressions are considerably more complicated and do not lend themselves to the same method of evaluation.[9]

---

[9]Vidya has actually carried out the analysis for $z \neq 0$, but that analysis has not been checked independently and has, therefore, not been programed for computation. The analysis can, however, be made available in its present form.

4.5 Calculative Procedure

The calculation of the aerodynamic characteristics of a rec-
tangular wing element, using the analysis developed in the present
report, requires the solution of the set of simultaneous equations
given by either Equations (38) or (39). This solution yields the
loading coefficients, $\gamma_n{}^*$, and the strength of the separated
vortices, Γ^*, which in turn determine the normal force coefficient
and the center of pressure.

The procedure for performing the numerical calculations is
outlined below:

(a) Select the number of terms, n_h, to be used in the series
representation of the loading (i.e., the number of nonzero harmonics
to be carried in the calculation). This will be discussed further
in Section 6.

(b) Calculate the Fourier coefficients, a_n, using Equa-
tions (25) and (26) with

$$n = 1, 3, \ldots, (2n_h - 1)$$

for

$$0 \leq \psi_0 \leq \pi$$

and

$$\frac{x - \xi_i}{s} = \frac{(x_c/c) - 0.25}{A/2}$$

where x_c/c is the distance of the control line behind the lead-
ing edge, expressed in chord lengths.

(c) Calculate the Fourier coefficients a_{nj} where

$$a_{nj}\left(\frac{x - \xi_i}{s}\right) = \frac{2}{\pi} \int_0^\pi a_n\left[\frac{(x_c/c) - 0.25}{A/2}, \psi_0\right] \cos j\psi_0 \, d\psi_0 \qquad (70)$$

and

$$j = 0, 2, \ldots, (2n_h - 2)$$

(d) Determine the coefficient matrix of the set of simultaneous equations (Eq. (38) or (39)) using Equation (40).

(e) Assume an initial value of the shedding angle, θ, for the separated vortex system.

(f) Calculate the Fourier coefficients, g_j, from

$$g_j\left(\frac{x}{s}\right) = \frac{2}{\pi} \int_0^\pi \frac{\overline{w}(x/s, \psi_o)}{\Gamma^* V_\infty \sin \alpha} \cos j\psi_o \, d\psi_o \qquad (71)$$

for

$$j = 0, 2, \ldots, (2n_h - 2)$$

and

$$\frac{x}{s} = \frac{x_c/c}{A/2}$$

(g) Determine $\left(\gamma_n^*\right)_u$ by solving Equations (43) and (44).

(h) Determine $\left(\gamma_n^*\right)_S$ by solving Equation (45).

(i) Calculate Γ^* using Equation (51).

(j) Calculate the normal force coefficient, C_N, the center of pressure, $\overline{x}/c$, and the new shedding angle, θ, using Equations (67), (69), and (61), respectively.

(k) Using this new value of θ, repeat steps (f) through (j) and compare the two values of C_N. If the desired accuracy in C_N has not been obtained, return to step (f) and repeat until it is obtained.

5. AERODYNAMIC THEORY OF SWEPTBACK WINGS WITH LEADING-EDGE SEPARATION

5.1 Construction of Mathematical Model

Having developed a theoretical analysis for the rectangular wing element with side-edge flow separation which satisfies the proper conditions of no flow through the wing and finite velocities at the side edges, we can now proceed to apply the theory to a wider variety of planforms in the following manner. Since the Kutta condition of finite velocity at the side edges is actually satisfied for all values of x (see Eq. (50)), the only singularities in velocity in the foregoing theory are along the lifting line itself. Therefore, other planforms can be constructed by using rectangular wings of various aspect ratios as elementary building blocks, provided that the trailing edge is straight. This representation will enable us to treat rather general leading-edge shapes, as shown in the sketch below.

————— lifting line (at 1/4 chord) of rectangular wing element

– – – – control line of rectangular wing element (at 3/4 chord)
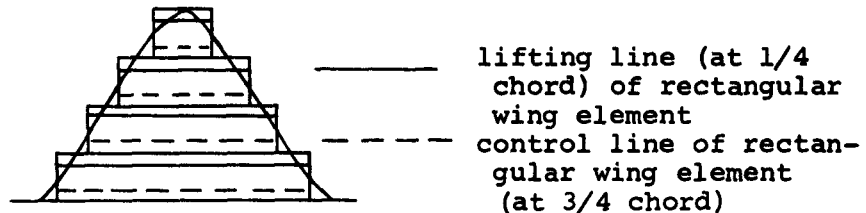
We shall now place a lifting line at the quarter chord of each rectangular wing element and proceed to satisfy the boundary condition of no flow through the wing surface at the corresponding 3/4-chord lines, accounting for the downwash from all of the wing elements and their associated shed vortices. This will require that we be able to calculate the downwash produced along the 3/4 chord of any rectangular wing element by the vortex system associated with any other wing element. It is clear, then, from

the foregoing sketch that for a sweptback wing we must be able to
calculate the downwash <u>anywhere</u> in the plane of the wing as pro-
duced by any of the rectangular wing elements. In particular,
we shall require the downwash <u>outside the span</u> of the lifting line
itself. For this purpose, we shall have recourse to Equation (48)
which was used in satisfying the Kutta condition.

Consider now the case of a sweptback wing which is to be made
up of n_w rectangular wing elements of equal chord $c_i = c_o/n_w$
and whose semispans are selected such that the area of each rectan-
gular element is equal to the area it replaces (see sketch)
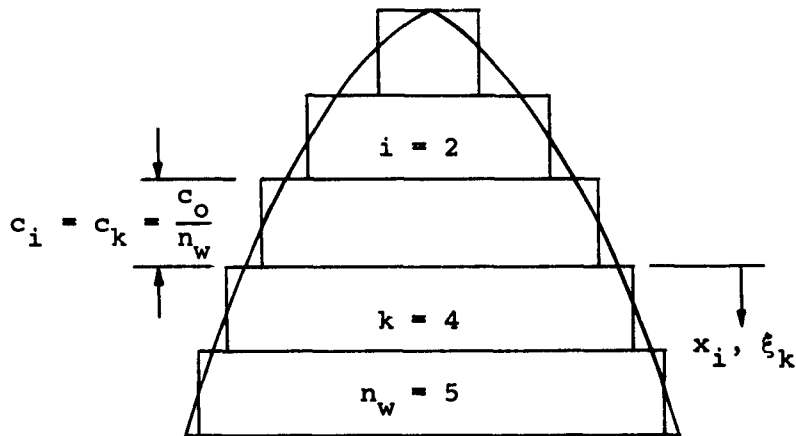
Note that the distances x_i and ξ_k will be measured rearward
from the leading edge of the kth wing element.

The boundary condition to be satisfied on each of the n_w
rectangular wing elements is that the normal velocity, $(\overline{w})_{ii}$,
due to the separation vortices of the wing itself, the ith wing,
plus the normal velocity, $(w*)_{ii}$, due to the lifting line of
the ith wing and its trailing sheet must exactly cancel the
component of the free stream normal to the wing $(V_\infty \sin \alpha)$ plus
the sum of the normal components induced by the vortex systems

of all of the other wings, $\displaystyle\sum_{\substack{k=1 \\ k\neq i}}^{n_w} (w)_{ik}$, where

$$\sum_{\substack{k=1 \\ k\neq i}}^{n_w} (w)_{ik} = \sum_{\substack{k=1 \\ k\neq i}}^{n_w} \left[(w^*)_{ik} + (\overline{w})_{ik} \right] \tag{72}$$

The boundary condition can, therefore, be written in the form

$$\left(\frac{w^*}{V_\infty}\right)_{ii} + \left(\frac{\overline{w}}{V_\infty}\right)_{ii} = - \sin \alpha - \sum_{\substack{k=1 \\ k\neq i}}^{n_w} \left[\left(\frac{w^*}{V_\infty}\right)_{ik} + \left(\frac{\overline{w}}{V_\infty}\right)_{ik} \right] \tag{73}$$

where this condition must be satisfied for all values of $i(i = 1, 2, \ldots, n_w)$. Thus, a set of n_w simultaneous equations is generated. Now if the loading coefficients and the separated vortex strengths on all of the rectangular wing elements except the ith wing are known, and if the summation on the right-hand side of Equation (73) can be replaced by an even cosine series, then the boundary value problem can be solved in the same manner as is presented in Section 4.2.4 for the rectangular wing alone.

Initially, in the solution of the sweptback wing problem, the vortex strengths and the loading coefficients are not known for any of the n_w wings. However, an initial guess can be made by treating each wing as an isolated rectangular wing and using the method of Section 4 to obtain initial values for the loading coefficients, $(\gamma_n^*)_i$ and the separated vortex strengths, Γ_i^*, for each of the n_w wings. Then an iterative technique can be used to solve the set of n_w equations. Since the sweptback wings being treated in the present analysis are restricted to

those which are symmetrical about the midspan, the midspans of the rectangular elements are aligned and thus the downwash produced on any element by any other elements is symmetrical about the midspan of the ith element. Therefore, the summation can be represented by an even cosine series of the form

$$\sum_{\substack{k=1 \\ k \neq i}}^{n_w} \left[\left(\frac{w^*}{V_\infty}\right)_{ik} + \left(\frac{\bar{w}}{V_\infty}\right)_{ik} \right] = \sin \alpha \sum_{j=0,2,4}^{\infty} \left(b_j\right)_{ik} \cos j\psi_0 \qquad (74)$$

where

$$- \pi \leq \psi_0 \leq \pi$$

Now, by a development similar to that of Section 4.2.4 the set of simultaneous equations to be solved may be written as

$$\left. \begin{aligned} \sum_{n=1,3,5}^{\infty} \left(f_{nj}\right)_{ii} \left(\gamma_n^*\right)_i &= \left(g_j\right)_{ii} \Gamma_i^* + 1 + \left(b_j\right)_{ik} \; ; \quad j = 0 \\ \sum_{n=1,3,5}^{\infty} \left(f_{nj}\right)_{ii} \left(\gamma_n^*\right)_i &= \left(g_j\right)_{ii} \Gamma_i^* + \left(b_j\right)_{ik} \; ; \quad j = 2,4,\ldots \end{aligned} \right\} \qquad (75)$$

There are n_w sets of these simultaneous equations to be solved by the iterative technique. Equations (75) are the counterpart of Equations (39) for the rectangular wing and may be solved in the same manner by splitting the solution for γ_n^* into an unseparated solution $(\Gamma_i^* = 0)$ and a solution due to separation, as described in Section 4.2.4.

In order to obtain the coefficients b_j, we shall have to calculate the upwash w_{ik} produced at the 3/4 chord of the ith wing element by the vortex system associated with the kth wing element. For this purpose, we shall need the distances from the kth lifting line to the ith control line, given by

$$\frac{x_i - \xi_k}{s_k} = \frac{i - k + \frac{1}{2}}{n_w \frac{s_k}{s_o} \frac{s_o}{c_o}} \qquad (76)$$

for the determination of $w_{ik}{}^*$, and the distance from the leading edge of the kth wing element to the ith control line, given by

$$\frac{x_i}{s_k} = \frac{i - k + \frac{3}{4}}{n_w \frac{s_k}{s_o} \frac{s_o}{c_o}} \qquad (77)$$

for the determination of $\overline{w}_{ik}$. Note that both of these distances are expressed in semispans of the wing element whose vortex system produces the downwash (i.e., of the kth wing element).

Now from Equation (28) we can write for points lying within the span of the lifting line (i.e., for $-1 \leq (y/s_k) \leq 1$)

$$\frac{w_{ik}{}^*}{V_\infty \sin \alpha}\left(\frac{x_i - \xi_k}{s_k}, \psi_o\right) = -\sum_{n=1,3}^{\infty} \left(\gamma_n{}^*\right)_k \left[\frac{2\pi \sin n\psi_o}{\sin \psi_o} + \frac{\pi}{2} a_{n_k}\left(\frac{x_i - \xi_k}{s_k}, \psi_o\right)\right]$$

$$\text{for } x_i - \xi_k > 0 \qquad (78)$$

$$= -\sum_{n=1,3}^{\infty} \left(\gamma_n{}^*\right)_k \left[\frac{\pi}{2} a_{n_k}\left(\frac{x_i - \xi_k}{s_k}, \psi_o\right)\right]$$

$$\text{for } x_i - \xi_k < 0 \qquad (79)$$

where

$$\psi_o = \cos^{-1}\left(-\frac{y}{s_k}\right)$$

For points lying <u>outside</u> the span of the lifting line (i.e., for $1 < \left|y/s_k\right| < \infty$), Equation (28) is modified in accordance with Equation (48) to yield

$$\frac{w_{ik}{}^*}{V_\infty \sin \alpha}\left(\frac{x_i - \xi_k}{s_k}, \frac{y}{s_k}\right) = -\sum_{n=1,3}^{\infty}\left(\gamma_n{}^*\right)_k\left\{\frac{2\pi\left[\sqrt{\left(\frac{y}{s_k}\right)^2 - 1} - \left|\frac{y}{s_k}\right|\right]^n}{\sqrt{\left(\frac{y}{s_k}\right)^2 - 1}}\right.$$

$$\left. + \frac{\pi}{2}\,a_{n_k}\left(\frac{x_i - \xi_k}{s_k}, \frac{y}{s_k}\right)\right\}$$

$$\text{for}\quad x_i - \xi_k > 0 \tag{80}$$

$$\frac{w_{ik}{}^*}{V_\infty \sin \alpha}\left(\frac{x_i - \xi_k}{s_k}, \frac{y}{s_k}\right) = -\sum_{n=1,3}^{\infty}\left(\gamma_n{}^*\right)_k\left[\frac{\pi}{2}\,a_{n_k}\left(\frac{x_i - \xi_k}{s_k}, \frac{y}{s_k}\right)\right]$$

$$\text{for}\quad x_i - \xi_k < 0 \tag{81}$$

Similarly, we obtain the required expression for $\overline{w}_{ik}$ (the up-wash produced at the ith control line by the separated vortex system associated with the kth wing element) by replacing x by x_i, s by s_k, and c by c_k in Equation (12). With the resulting equation and Equations (78) through (81), we are now in a position to set up an iterative procedure for determining the loading on the sweptback wing with leading-edge separation. The detailed procedure will be outlined in Section 5.5.

It should be noted that the same method may be applied to a low or intermediate aspect ratio rectangular wing by representing it as a chordwise distribution of higher aspect ratio rectangular wing elements. The purpose of such a procedure in these cases would be to extract more detailed information regarding chordwise load distribution and center of pressure than can be obtained by using a single wing element.

5.2 Determination of Shedding Angle, θ_i, on i^{th} Rectangular Wing Element

The determination of the angle, θ_i, at which the separated vortices are shed from each of the rectangular wing elements is similar to that described in Section 4.2.6 for the rectangular wing alone. However, in addition to the velocities induced by the ith wing itself, we must now consider the velocities induced by all of the other wing elements making up the swept wing.

The general expression for the shedding angle on the ith wing is given by (Eq. (53))

$$\tan \theta_i = \frac{w_{av}}{u_{av}}$$

$$= \left[\frac{\frac{1}{2}\left(w_{y=s_i-\epsilon} + w_{y=s_i+\epsilon}\right)}{\frac{1}{2}\left(u_{y=s_i-\epsilon} + u_{y=s_i+\epsilon}\right)} \right]_{z=o+\epsilon} \tag{82}$$

Now, since the boundary condition of no flow through the wing has been satisfied at the control line, we have

$$w_{y=s_i-\epsilon} = 0 \qquad (83)$$

The expression for the velocity induced by the vortex system of the ith wing on itself is the same as that in Section 4.2.6. Therefore, the total upwash at the ith control line (just outside the span) is given by

$$\left(\frac{w}{V_\infty \sin \alpha}\right)_{y=s_i+\epsilon} = \left(\frac{\bar{w}_{B_{ii}} + \bar{w}_{L_{ii}}}{V_\infty \sin \alpha}\right)_{y=s_i} - \left(\frac{\bar{w}_{R_{ii}}}{V_\infty \sin \alpha}\right)_{y=s_i-\epsilon}$$

$$-\frac{\pi}{2}\sum_{n=1,3}^{\infty}\left(\gamma_n^*\right)_i a_{n_{ii}} + 1 + \sum_{\substack{k=1\\k\neq i}}^{n_w}\left(\frac{w_{ik}}{V_\infty \sin \alpha}\right)_{y=s_i} \qquad (84)$$

where w_{ik} is the upwash at the ith control line produced by the vortex system of the kth wing element. Similarly, from Section 4.2.6, using Equations (58) and (60), we have for the average chordwise velocity at the end of the ith control line

$$\frac{1}{2}\left[\left(\frac{u}{V_\infty \sin \alpha}\right)_{y=s_i-\epsilon} + \left(\frac{u}{V_\infty \sin \alpha}\right)_{y=s_i+\epsilon}\right] = \frac{\pi}{2}A_i\Gamma_i^* - \left(\frac{\bar{w}_{L_{ii}}}{V_\infty \sin \alpha}\right)_{y=s_i} \quad \tan\theta_i + \mathrm{ctn}\,\alpha$$

$$+\frac{1}{2}\sum_{\substack{k=1\\k\neq i}}^{n_w}\left[\left(\frac{u_{ik}}{V_\infty \sin \alpha}\right)_{y=s_i-\epsilon} + \left(\frac{u_{ik}}{V_\infty \sin \alpha}\right)_{y=s_i+\epsilon}\right]$$

That is,

$$\frac{1}{2}\left[\left(\frac{u}{V_\infty \sin\alpha}\right)_{y=s_i-\epsilon} + \left(\frac{u}{V_\infty \sin\alpha}\right)_{y=s_i+\epsilon}\right] = \frac{\pi}{2}A_i\Gamma_i^* - \left(\frac{\overline{w}_{L_{ii}}}{V_\infty \sin\alpha}\right)_{y=s_i} \tan\theta_i + \operatorname{ctn}\alpha$$

$$-\sum_{\substack{k=1\\k\neq i}}^{n_w}\left(\frac{\overline{w}_{R_{ik}}+\overline{w}_{L_{ik}}}{V_\infty \sin\alpha}\right)_{y=s_i}\tan\theta_k \qquad (85)$$

Finally, substitution of Equations (83), (84), and (85) into Equation (82) yields the following expression for the shedding angle at the ith control line

$$\tan\theta_i = \frac{\dfrac{1}{2}\left(\dfrac{\overline{w}_{B_{ii}}+w_{L_{ii}}}{V_\infty \sin\alpha}\right)_{y=s_i} - \left(\dfrac{\overline{w}_{R_{ii}}}{V_\infty \sin\alpha}\right)_{y=s_i-\epsilon} - \dfrac{\pi}{2}\displaystyle\sum_{n=1,3}^{\infty}(\gamma_n^*)_i\, a_{n_{ii}}+1+\displaystyle\sum_{\substack{k=1\\k\neq i}}^{n_w}\left(\dfrac{w_{ik}}{V_\infty \sin\alpha}\right)_{y=s_i}}{\dfrac{\pi}{2}A_i\Gamma_i^* - \left(\dfrac{\overline{w}_{L_{ii}}}{V_\infty \sin\alpha}\right)_{y=s_i}\tan\theta_i + \operatorname{ctn}\alpha - \displaystyle\sum_{\substack{k=1\\k\neq i}}^{n_w}\left(\dfrac{\overline{w}_{R_{ik}}+\overline{w}_{L_{ik}}}{V_\infty \sin\alpha}\right)_{y=s_i}\tan\theta_k}$$

$$(86)$$

This equation is solved by an iterative procedure, as was Equation (61) for the single rectangular wing element.

5.3 Normal Force, Center of Pressure, and Span Loading

The total normal force on the sweptback wing is simply the sum of the normal forces on all of the wing elements, so that the total normal force coefficient is, from Equations (66) and (67),

$$
C_N = \frac{N}{\frac{1}{2}\rho V_\infty^2 S_o} = \frac{\displaystyle\sum_{i=1}^{n_w} N_i}{\frac{1}{2}\rho V_\infty^2 \displaystyle\sum_{i=1}^{n_w} 2 s_i c_i}
$$

$$
= \frac{4\pi n_w \sin\alpha \cos\alpha \dfrac{s_o}{c_o} \displaystyle\sum_{i=1}^{n_w} \left(\dfrac{s_i}{s_o}\right)^2 \left[\dfrac{\pi}{2}\left(\gamma_1{}^*\right)_i + 2\Gamma_i{}^*\right]}{\displaystyle\sum_{i=1}^{n_w} \dfrac{s_i}{s_o}}
\tag{87}
$$

The center of pressure is found by summing the pitching moment about the wing leading edge and dividing by the total normal force. That is,

$$
\bar{x} = \frac{\displaystyle\sum_{i=1}^{n_w} N_i \bar{x}_i}{\displaystyle\sum_{i=1}^{n_w} N_i}
\tag{88}
$$

Thus, noting that the loading due to $(\gamma_1{}^*)$ acts at the quarter chord of the ith wing element whereas $\Gamma_i{}^*$ acts at the midchord of the element, we have

$$\sum_{i=1}^{n_w} N_i \bar{x}_i = 4\pi \frac{c_o}{n_w} \rho V_\infty^2 \sin \alpha \cos \alpha \sum_{i=1}^{n_w} s_i^2 \left[\frac{\pi}{2} \left(\gamma_1^*\right)_i \left(i - \frac{3}{4}\right) \right.$$

$$\left. + 2\Gamma_1^* \left(i - \frac{1}{2}\right) \right] \tag{89}$$

Therefore, the center of pressure for the sweptback wing is given by

$$\frac{\bar{x}}{c_o} = \frac{\displaystyle\sum_{i=1}^{n_w} \left(\frac{s_i}{s_o}\right)^2 \left[\frac{\pi}{2} \left(\gamma_1^*\right)_i \left(i - \frac{3}{4}\right) + 2\Gamma_i^* \left(i - \frac{1}{2}\right) \right]}{\displaystyle n_w \sum_{i=1}^{n_w} \left(\frac{s_i}{s_o}\right)^2 \left[\frac{\pi}{2} \left(\gamma_1^*\right)_i + 2\Gamma_i^* \right]} \tag{90}$$

The span loading (in, say, pounds per foot) is obtained by expressing the quantity $c_l c$ at each spanwise station, where c_l is the section lift coefficient. Equating two expressions for the lift on an elementary chordwise strip (see sketch),
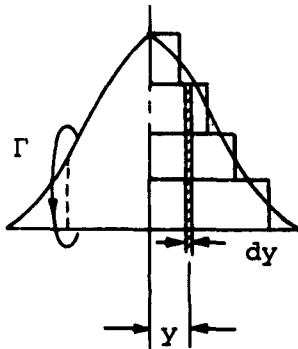
we have

$$c_l c \, dy \cdot \frac{1}{2} \rho V_\infty^2 = \rho V_\infty \Gamma \, dy \tag{91}$$

where Γ is the total circulation on the chordwise strip. Thus

$$c_l c = \frac{2\Gamma}{V_\infty} \tag{92}$$

In the present mathematical model, the total circulation round any chordwise strip is given by

$$\Gamma(y) = \sum_i \left[\gamma_i(y) + \frac{d\Gamma_i}{d\xi} \cdot c_i \right] \tag{93}$$

where the summation is carried over the wing elements whose semispan is greater than the value of y in question. Thus, since $\gamma(y)$ in the present analysis is represented by a Fourier sine series, Equations (92) and (93) combine to yield the following expression for the non-dimensional span loading on a swept wing.

$$\frac{c_l c(y)}{c_o} = \frac{2\Gamma(y)}{V_\infty c_o} = 8\pi \frac{s_o}{c_o} \sin \alpha \sum_i \frac{s_i}{s_o} \left[\Gamma_i^* + \sum_{n=1,3}^{\infty} \frac{(\gamma_n^*)_i}{n} \sin n\psi_i \right] \tag{94}$$

where $\psi_i = \cos^{-1}(-y/s_i)$ and the summation over i is carried over the wing elements whose semispan is greater than y.

5.4 Downwash at the Tail Location

The calculation of the downwash behind a swept wing is again a matter of collecting the appropriate expressions for w^* and $\overline{w}$. That is, the upwash at any point is again given by

$$w(x, y, z) = w^* + \overline{w} + V_\infty \sin \alpha$$

just as in the rectangular wing case, but here we must account for the contribution of every wing element comprising the swept wing. Thus, we have

$$w^* = \sum_{k=1}^{n_w} w_{ik}^*$$

and

$$\overline{w} = \sum_{k=1}^{n_w} \overline{w}_{ik}$$

where the distance x_i appearing in the expressions for w_{ik}^* and $\overline{w}_{ik}$ is now the distance from the leading edge of the kth wing element to the point in question. For points lying in the plane of the wing, the expressions for w_{ik}^* are given by Equations (78) to (81), depending upon whether the point in question lies inside or outside of the span of the kth wing element. The corresponding expressions for $\overline{w}_{ik}$ are given by Equations (12) if we replace x by x_i, s by s_k, and c by c_k. For points lying out of the plane of the wing, see Footnote 9, page 46.

5.5 Calculative Procedure

The detailed procedure for performing the numerical calculations is outlined below:

(a) Select the number of wing elements, n_w, and the number of harmonics, n_h, to be carried in the calculation. This point will be discussed in Section 6.2 where convergence with respect to these parameters is investigated.

(b) Assume an initial value of the shedding angle, $\theta_i (i = 1, 2 \ldots n_w)$, for each wing element.

(c) Calculate the $(f_{nj})_{ii}$ coefficient matrix for each wing, treating each as an isolated wing, using the method outlined in steps (b) through (d) of Section 4.5.

(d) Calculate the Fourier coefficients $(g_j)_{ii}$ as outlined in step (f) of Section 4.5.

(e) Obtain initial values of the loading coefficients, $(\gamma_{n_u}{}^*)_i$ and $(\gamma_{n_s}{}^*)_i$, for each wing element by treating each wing as an isolated rectangular wing and solving Equations (43), (44), and (45).

(f) Calculate $\Gamma_i{}^*$ for each isolated wing by Equation (51).

(g) Calculate $w_{ik}{}^*$ for $i = 1$; $k = 2, \ldots, n_w$ using Equation (76) and Equations (78), (79), (80), or (81) as appropriate with the values of $(\gamma_n{}^*)_k$ from step (e).

(h) Calculate $\bar{w}_{ik}$ for $i = 1$; $k = 2, \ldots, n_w$ using Equations (12) and replacing x by x_i (Eq. (77)), s by s_k, and c by c_k.

(i) Determine coefficients $(b_j)_{ik}$ from Equation (74), using the results of steps (g) and (h).

(j) Solve Equations (75) for the unseparated loading coefficients $(\gamma_{n_u}{}^*)_i$ by setting $\Gamma_i{}^* = 0$ for $i = 1$.

(k) Solve Equations (75) for the loading coefficients due to separation $(\gamma_{n_s}{}^*)_i$ by setting $\Gamma_i{}^* = 1$ and omitting the remainder of the right-hand side of Equations (75) for $i = 1$.

(l)   Replace results of step (e) with results of steps (j) and (k).

(m)   Determine $\Gamma_i{}^*$ for $i = 1$ by using Equation (51). This completes the first iteration on $(\gamma_n{}^*)_1$.

(n)   Replace results of step (f) with results of step (m).

(o)   Repeat steps (g) through (n) for $i = 2, 3, \ldots, n_w$ with $i \neq k$ in steps (g) and (h). This completes the first iteration for all wing elements.

(p)   Calculate normal force coefficient and center of pressure using Equations (87) and (90).

(q)   Repeat steps (g) through (p) until desired accuracy on normal force is obtained.

(r)   Calculate $\theta_i (i = 1, 2, \ldots, n_w)$ from Equation (86).

(s)   Repeat steps (d) through (r) until the desired accuracy on θ_i is obtained.

6. NUMERICAL CALCULATIONS AND COMPARISON WITH EXPERIMENT

This section of the report will describe the results of the calculations which were made using the analysis presented in Section 4 for the rectangular wing and that presented in Section 5 for the swept wing. The rectangular wing calculations will be discussed first, since this wing element is the building block for the swept wing analysis. Convergence of the rectangular wing solution is therefore necessary if the swept wing solution is to converge. The rectangular wing calculations were carried out on an IBM 1620 digital computer, whereas the swept wing calculations were performed on an IBM 7094 computer.

6.1 Rectangular Wing

Two investigations were made using the rectangular wing analysis presented in Section 4. The first of these was to determine the number of terms (nonzero Fourier harmonics) required in the series representation of the loading in order to insure convergence on values of the normal force and center of pressure. The second investigation was to determine the angle θ at which the separated vortices must be shed in order for the vortices to follow the local streamlines in the vertical plane containing the wing tip. After these studies were completed, systematic calculations of the normal-force coefficient and center of pressure were carried out for a range of aspect ratios and angles of attack, and the results have been compared with available experiment. In all of these calculations, the rectangular wing is represented by a single wing element, since we wish to investigate the convergence of the basic building block of the theory.

6.1.1 Convergence with number of harmonics

Table II presents the results of rectangular wing calculations in which the number of nonzero harmonics n_h in the loading was varied from 2 to 14, for two angles of attack, over a range of aspect ratios. For these calculations, the control line was fixed at the 3/4-chord location and the shedding angle θ was held fixed at half the angle of attack. It can be seen that the values of

C_N, $\bar{x}/c$, and Γ^* converge rapidly and that 8 nonzero harmonics evidently suffice for 1-percent accuracy in C_N even at an aspect ratio of 20. The values of $\bar{x}/c$ and Γ^* converge somewhat more slowly, as seen from Tables II(b) and II(c), and it can be seen that the rate of convergence decreases as the aspect ratio is increased. (This point is significant in regard to the swept wing solution.) Also, it can be seen that convergence is more rapid at the higher angles of attack, and it is evident that the solution will have convergence difficulties at vanishing angles of attack, since the shed vortices tend to coalesce into the wing tip.

The significance of the increase in the number of harmonics required with increasing aspect ratio is illustrated by Figure 3, which can be used as a guide for the swept wing solution. For the rectangular wing itself, this feature of the solution is of little significance, since one would logically return to linear theory at very high aspect ratios. However, for a swept wing, even of low aspect ratio, the aspect ratio of the trailing element increases as the number of wing elements is increased. For example, if a delta wing of aspect ratio 3 is represented by 10 rectangular wing elements, the trailing element has an aspect ratio of 14.25. Thus, Figure 3 may be used as a guide for estimating the number of harmonics one might need to use in the swept wing solution. It must be borne in mind, however, that the mutual interference among wing elements may require still larger numbers of nonzero harmonics for convergence of the swept wing solution.

6.1.2 Detailed loading coefficients for a specific case

The detailed convergence of the mathematical solution is perhaps best illustrated by listing all of the loading coefficients for a particular rectangular wing element. For this purpose, we shall select a rectangular wing of aspect ratio 3.5 at 20° angle of attack, with the shedding angle θ fixed at half the angle of attack and the control line located at the 3/4-chord position. The reason for selecting this particular case is that it represents

the fourth wing element of a delta wing of aspect ratio 2. We shall, therefore, be able to compare the loading coefficients on the isolated wing element with those in which the interference from other elements is included.

The loading coefficients for the selected case are listed in Table III, and it is noted that 19 nonzero harmonics have been carried in the calculation, to correspond with the delta wing calculations of Section 6.2.4. It can be seen from Table III that the loading coefficients associated with the higher harmonics (n large) are several orders of magnitude smaller than the leading coefficients so that one need not have carried 19 harmonics for this case. In fact, as was pointed out in the previous section (Fig. 3), 6 harmonics was a sufficient number for the selected case.

The separated vortex strength Γ^* and the normal force and center of pressure corresponding to the loading coefficients of Table III are obtained by using Equations (51), (67), and (69). The resulting values are

$$\Gamma^* = 0.06307$$

$$C_N = 1.4450$$

$$\overline{x}/c = 0.4043$$

6.1.3 Shedding angle calculations

Calculations have been carried out to determine the shedding angle θ of the separation vortices by the iterative procedure of Section 4.2.6, and the results are plotted in Figure 4. It can be seen that the shedding angle ratio θ/α increases with aspect ratio and decreases with angle of attack. Furthermore, it is noted that the shed vortices are found to lie <u>above the free-stream direction</u> for aspect ratios above 2 for angles of attack below

15°. This result is known to be unrealistic because of the down-wash which must be produced by a lifting wing and which must cause the trailing-edge vortices to drift below the free-stream direction. On the other hand, it must be borne in mind that the assumed mathematical model does not permit rolling up of the side-edge vortex sheets. This process would naturally tend to drive the shed vortices downward and result in a smaller shedding angle of the rolled-up vortex cores.

6.1.4 Effect of control line location

Because of the above result, and because the placement of the control line (where θ is calculated) at the 3/4-chord location was based on matching the lift-curve slope at $\alpha = 0$, it was considered worthwhile to investigate the effect of control line location on the calculated shedding angle θ. Therefore, θ was recomputed with the control line placed at the 65 and 85 percent chord locations, and the results are presented in Figure 5. It can be seen that the effect of control line location on the shedding angle was rather small, and that the new control line locations failed to yield more realistic values of θ. Therefore, it was concluded that the control line should remain at the 3/4-chord location , in order to insure the correct lift-curve slope at small angles of attack, but that the values of the shedding angle θ determined by the iterative technique of the present analysis (using a single-wing element) are evidently unrealistic. This fact is most likely associated with the use of a lifting line rather than a lifting surface and with the fact that the shedding angle is determined only at the location of the control line at which the boundary condition is satisfied. This situation might be expected to improve if one were to use a number of wing elements of higher aspect ratio to represent the rectangular wing. This has not been done.

6.1.5 Normal force and center of pressure

Systematic calculations have been preformed to determine the variations of normal force and center of pressure on rectangular wings at various angles of attack for a wide range of aspect ratios (using a single wing element), and these results are presented in Figure 6. For these calculations, the control line is at the 3/4-chord location, and the value of θ is that determined by iteration. For a given angle of attack, the normal-force coefficient is found to increase with increasing aspect ratio while the center of pressure moves forward. For a given aspect ratio, the normal-force coefficient increases nonlinearly with angle of attack, and the center of pressure is seen to be relatively insensitive to angle of attack.

6.1.6 Comparisons with experiment

The calculated variation of normal force with angle of attack (for a single rectangular wing element), is compared with experimental data in Figure 7(a) for rectangular wings of aspect ratios from 0.2 to 5.0. It can be seen that the theoretical normal force agrees with experiment within about 10 percent over the angle-of-attack range shown. A notable exception is the aspect ratio 5 wing beyond the stall, and it is recalled that the present theoretical model does not account for leading-edge stall on rectangular wings. In a broader sense, it may be said that the theory fails if the flow becomes unsteady. Thus, for all aspect ratios, the theory will fail above some angle of attack, since all flat plates at 90° angle of attack produce an unsteady wake, whether the vortices in question arise from leading, trailing, or side edges. However, the angle of attack for the onset of unsteady shedding will be lower for the higher aspect ratios, because of the orientation of the shed vortices (spanwise rather than chordwise). That is to say, vortices which are aligned nearly normal to the free stream produce an unsteady flow, while those aligned nearly with the free stream produce a steady flow. Thus, as seen in Figure 7(a), the angle-of-attack range over which the theory is valid will be larger for the

lower aspect ratios. In Reference 1, Bollay showed that his theory agreed with experiment for angles of attack up to 45° for an aspect ratio of 1/30. The present theory is in close agreement with Bollay's theory for vanishing aspect ratios, at least insofar as normal force is concerned, despite the assumptions of a single lifting line and a constant separated vortex strength along the chord.

In Figure 7(b), the calculated center of pressure is presented for a variety of rectangular wing elements. It is seen that the present theory predicts centers of pressure which are rather far rearward (toward the midchord location). Experimentally (Ref. 4), it is found that the center of pressure remains closer to the quarter chord for rectangular wings of all aspect ratios. It is interesting to note that Bollay's theory (Ref. 1) places the center of pressure at the quarter chord for all aspect ratios by assuming the chordwise load distribution to be that of a wing of infinite aspect ratio. The present theory, on the other hand, places the lifting line at the quarter chord but places the center of pressure of the separated vortices at the midchord by assuming the separated vortices to be uniformly distributed in the chordwise direction. This restriction can be removed by employing a number of rectangular wing elements to represent the rectangular wing and then solving for the chordwise distribution of loading and shed vorticity.

For all of the above results using a single rectangular wing element, the shedding angle of the separated vortices has been calculated by the iterative procedure described in Section 4.2.6. It will be recalled (see Fig. 4) that these calculated shedding angles appear to be unrealistically high, particularly at high aspect ratios and at low angles of attack. Nevertheless, the agreement with experimental normal forces on rectangular wings is quite satisfactory even in these ranges.

Comparisons with experimental values of the shedding angle are of questionable validity, since the mathematical model is clearly unrealistic in this detail. That is to say, the vortex sheet shed from the side edge of a rectangular wing actually rolls up into a

single vortex core which lies above the wing surface. It is the position of this core which is measured experimentally. The only known measurements of this kind (contained in Ref. 23) indicate a considerable (nonlinear) variation in the orientation of this vortex core, both with chordwise location and angle of attack for a rectangular wing of aspect ratio 2. In any case, it would not be reasonable to expect that the theoretical shedding angle at the side edge which renders the mathematical solution of the problem unique for the selected theoretical model (with no rolling up) should agree with experimental measurements of the orientation of the rolled-up vortex core. In fact, it is clear that rolling up of the side-edge vortex sheets would cause the uppermost shed vortices to be depressed toward the wing surface. Therefore, the experimental angle θ_c of the vortex core relative to the plate should logically be smaller than the theoretical angle θ of the side-edge sheets. That is

$$\theta > \theta_c$$

It is of some interest to note that in Bollay's theory (Ref. 1), the theoretical values of shedding angle may well be more realistic, since he satisfied the boundary condition (of no flow through the wing) in the mean rather than at a specific chordwise location, and also since he assumed a more realistic chordwise variation of shed vorticity than the uniform distribution of the present theory for a single-wing element. Bollay's approach yielded shedding angles not far from half the angle of attack in all cases. In the limit of vanishing aspect ratio, the present theory for the single rectangular element does yield values of θ which appear to be converging toward Bollay's value of half the angle of attack.

6.2 Triangular Wing

Calculations have been carried out for the special class of swept wings of triangular planform (i.e., delta wings) using the method of Section 5. Initially, the calculations were made with a double iteration; that is, with iteration on both the loading and the shedding angle of each wing element. However, for reasons which will be discussed below, the final calculations were carried out by iterating on the loading but leaving the shedding angle θ fixed. Therefore, convergence of the swept wing solution was investigated both with and without iteration on θ.

6.2.1 Convergence with number of iterations

Perhaps the key to the success or failure of the procedure described in Section 5.5 lies in the rate of convergence with iteration on the loading of each wing element. Therefore, this was investigated first using four rectangular wing elements. Furthermore, since the rate of convergence is expected to deteriorate with increasing aspect ratio, the highest aspect ratio $(A = 4)$ to be employed here was used for the convergence investigation. Figure 8 shows the convergence of the shed vorticity Γ^*, the first loading coefficient γ_1^* (which determines C_N and $\bar{x}/c_o$), and the normal force coefficient C_N with number of iterations on the loading. It can be seen that the convergence is generally oscillatory in nature and that in this case six iterations are adequate for the load distribution, whereas only three iterations are required to converge on the normal force.

Convergence with θ iterations (which are carried out <u>after</u> convergence on γ_n^*) is illustrated in Figure 9. It can be seen that convergence is again oscillatory and that four iterations on θ suffice here to determine θ within about 0.25°. On the other hand, about six iterations are required for convergence on the normal force.

6.2.2 Shedding angle calculations

A significant difference between the rectangular and tri-angular wing calculations lies in the fact that the present theory predicts a single shedding angle for the rectangular wing, as well as a single value for the shed vorticity, which is assumed constant over the chord, if a single wing element is used. For the delta wing, however, the method yields a chordwise <u>distribution</u> of these quantities by the use of many rectangular wing elements. The cal-culated distribution of shedding angle θ over the chord of a delta wing of aspect ratio 4 at 20° angle of attack is shown in Figure 10 using from two to eight wing elements to represent the delta wing. Here we see again, as in the case of the rectangular wing, that the predicted values of θ are unrealistically high. (in this case, they are all larger than the angle of attack.) But even more disturbing is the observation that θ is increasing as the number of wing elements increases. This may be associated with the increase in the predicted value of θ with aspect ratio, since the aspect ratio of the trailing element increases as the number of elements is increased.

6.2.3 Convergence with number of harmonics

The convergence of the normal force and center of pressure on the delta wing was next investigated using various numbers of rectangular elements to represent the delta wings. These results are shown in Figure 11, and it can be seen that convergence is quite satisfactory if only two wing elements are employed. However, if larger numbers of wing elements are employed, not only are more harmonics required (as would be expected because of the increased aspect ratio of the elements), but also rather large bumps are noted in the variation with harmonics. This is believed to be caused by the fact that there is a finite discontinuity in the downwash at the side edge of each rectangular element. Thus, with certain numbers of harmonics, certain spanwise points used in the Fourier analysis fall close to these discontinuities and cause apparent convergence difficulties. In order to check this hypothesis,

detailed downwash calculations were carried out for one case, and the fit obtained with the Fourier series was investigated. It was found that by adjusting the downwash at the point nearest the discontinuity, the bumps in the curves of Figure 11 could be reduced. It is also felt that with still larger numbers of wing elements the magnitude of each bump may be reduced because of the decrease in the magnitude of the discontinuity.

Perhaps the most significant results of Figure 11 are that (a) the rate of convergence with number of wing elements is slow, (b) the values of C_N are unrealistically high, and (c) the value of C_N is increasing with number of wing elements. Inasmuch as these difficulties with C_N are believed to be associated with the unrealistically high values of θ and their increase with increasing number of elements (see Fig. 10), it was decided to investigate the behavior of the delta wing solution without iterating on θ. The results of these calculations are shown in Figure 12, and it can be seen that (a) the convergence of C_N and $\bar{x}/c_o$ with number of wing elements is improved, and (b) the value of C_N is reduced, even for the rather large value of 1.0 assumed for the ratio of θ/α. It is concluded that, in applying the present theory to swept wings, one should leave θ/α as a parameter, because of the unrealistic predictions of θ for the assumed model.

6.2.4 Detailed loading coefficients for a specific case

In order to give a better insight into the behavior discussed above, detailed loading coefficients for each rectangular wing element are presented in Table IV for a delta wing of aspect ratio 2 $(s_o/c_o = 0.5)$ at 20° angle of attack with the value of θ/α fixed at 0.5. For this calculation, 8 wings and 19 nonzero harmonics are employed, and the characteristics of each wing element are listed in the following table.

Wing element No.	$\dfrac{s_i}{s_o}$	$\dfrac{c_i}{c_o}$	A_i	$\dfrac{C.L.}{c_o}$	$\dfrac{L.L.}{c_o}$	θ_i (deg)
1	0.0625	0.125	0.5	0.09375	0.03125	10
2	.1875	.125	1.5	.21875	.15625	10
3	.3125	.125	2.5	.34375	.28125	10
4	.4375	.125	3.5	.46875	.40625	10
5	.5625	.125	4.5	.59375	.53125	10
6	.6875	.125	5.5	.71875	.65625	10
7	.8125	.125	6.5	.84375	.78125	10
8	.9375	.125	7.5	.96875	.90625	10

where C.L. is the distance from the apex of the delta wing to the control line of each element, and L.L. is the distance from the apex to the corresponding lifting line.

The calculated loading coefficients on each element are listed in Table IV, and it will be recalled that the fourth element (Table IV(d)) has the same geometry as the isolated rectangular wing whose loading coefficients are listed in Table III. But, before comparing the results of Tables III and IV(d), it is well to refer back to Equations (75) representing the delta wing problem. It will be noted that all of the mutual interference among the wing elements is contained in the $(b_j)_{ik}$ and, therefore, appears only

in the <u>unseparated</u> solution $\left(\gamma_{n_u}^*\right)_i$ which is obtained by setting $\Gamma_i^* = 0$. Hence, the separated solution $\left(\gamma_{n_s}^*\right)_i$ is unaffected by interference and should be the same as for an isolated rectangular wing element of the same aspect ratio. Comparison of Tables III and IV(d) shows that this is indeed the case.[10]

A comparison of the values of $\left(\gamma_{n_u}^*\right)_i$ from the same tables shows that in the case of the delta wing (Table IV(d)) the mutual interference among the wing elements severely curtails the rate of convergence; that is, the highest harmonics are nearly the same order of magnitude as the first harmonic. In the case of the corresponding isolated wing element (Table III), these differed by six or seven orders of magnitude. Looking at the other wing elements of the delta wing (Table IV), we see that this difficulty is typical of all the wing elements except the leading element, which shows convergence similar to that for an isolated rectangular wing. The apparent reason for this difference lies in the fact that the present mathematical model produces finite discontinuities in the downwash for all wing elements except the first.

Despite the above difficulty, which may be expected to manifest itself in the calculation of such detailed quantities as span loading and downwash, it has been shown in the previous section and in Figure 12 that the gross quantities $(C_N$ and $\overline{x}/c_o)$ for the delta wing have nevertheless converged with 8 wings and 19 harmonics. For the calculation of these quantities and of the span loading, we require the values of shed vorticity Γ_i^* for each wing element. These are calculated from Equation (51) and are listed below.

---

[10]The small differences are attributed to the fact that the numbers in Table III were calculated on an IBM 1620 whereas those of Table IV were calculated on an IBM 7094.

Wing element No.	Γ_i^*
1	0.34311
2	.17177
3	.11823
4	.09146
5	.07197
6	.05901
7	.04707
8	.03732

The total normal force coefficient and center of pressure for the delta wing are given by Equations (87) and (90). The resulting values for the present case are

$$C_N = 0.9292$$

$$\bar{x}/c_o = 0.6272$$

The span loading on the delta wing can be calculated from Equation (94). The resulting span load distribution is tabulated as a function of y/s_o in Table V. It will be noted that the span loading goes to zero at $y/s_o = 0.9375$ which corresponds to the side edge of the eighth wing element.

6.2.5 Comparisons with experiment

The calculated variations of normal force and center of pressure with angle of attack for delta wings of aspect ratio 1, 2, 3, and 4 are compared with experiment and with linear theory in Figures 13 through 16. As explained earlier, it was found in the course of the calculations that iteration on the shedding angle of the separated vortices produced unrealistically high values of both shedding angle and normal force for delta wings. Therefore, for the calculations presented in Figures 13 through 16, the shedding angle was treated as a parameter and held fixed in each calculation.

It can be seen from Figures 13 through 16 that, for each aspect ratio investigated, there is a single value of the shedding angle ratio θ/α which yields good agreement with the experimental normal force for all angles of attack up to the experimental falling off of the lift-curve slope. This latter phenomenon is not predicted by the present theory and is evidently associated with a change in the type of flow separation (as in the case of rectangular wings). The calculated normal force is seen to increase with θ/α in all cases. (This effect is shown in Figure 17 for various aspect ratios.) On the other hand, the center of pressure is evidently insensitive to θ/α and agrees well with experiment for the cases where data are available (A = 1, 2, 4), particularly at the higher angles of attack. It is noted that linear theory also shows good agreement with experiment with regard to center-of-pressure location.

It is evident from Figures 13 through 16 that the present theory in all cases yields results which are considerably better than linear theory, provided that the appropriate value of the ratio θ/α is selected and held fixed. The required θ/α is a function of aspect ratio, and the resulting variation with aspect ratio is presented in Figure 18.

Since some limited experimental values of the shedding angle θ_c of the vortex cores over slender delta wings are available for aspect ratios of 1 and 1.67 (Refs. 24 and 25), these are also shown in Figure 18. One is again cautioned that these measurements do not actually correspond to experimental values of θ, since the separated vortices of the present mathematical model are not permitted to roll up into a single core. In keeping with this fact, it is seen from Figure 18 that the rolled-up core forms a much smaller angle with the plane of the wing than do the separated vortices of the assumed mathematical model which is required to give the experimental normal force.

It should be pointed out that all of the above calculations were performed using 8 wing elements and 19 harmonics. For the highest aspect ratio (4.0), which corresponds to the lowest shedding angle $(\theta/\alpha \approx 0.1)$, it is not certain that the mathematical solution has converged, particularly at the lowest angle of attack.

As a point of interest, one calculation of span load distribution was carried out for an aspect ratio 2 delta wing at $20°$ angle of attack, since data are available in Reference 26. The results are shown in Figure 19, and it can be seen that discontinuities are indicated in the theoretical span loading at the side edge of each rectangular wing element employed to represent the delta wing. It is observed that approximate agreement with experiment would be obtained by fairing out the discontinuities, but it is evident that a larger number of wing elements (and harmonics) would be required for accurate prediction of the span loading on delta wings.

7. CONCLUSIONS

A theoretical analysis has been developed for calculating the low-speed aerodynamic loads on rectangular wings with side-edge separation. This theory, which includes lifting-line theory for the case of no separation, yields the downwash everywhere in the plane of the wing and also incorporates the Kutta condition of finite velocity along the side edges. Because of this feature, it has been possible to extend the theory to other planforms with sweptback leading edges. An iterative technique has therefore been devised for calculating the aerodynamic characteristics of sweptback wings with leading-edge separation by representing the wings as a system of elementary rectangular wings.

Calculations have been carried out for both rectangular and delta wings of various aspect ratios, and the calculated normal force, center of pressure, load distribution, and shedding angles compared with experimental data. The following conclusions are drawn from the calculated results.

7.1 Rectangular Wings

(1) The method appears to converge rapidly with respect to number of harmonics, except at low angles of attack and/or high aspect ratios. These cases, however, are well covered by lifting-line theory and slender wing theory.

(2) A characteristic feature of the spanwise load distribution for a rectangular wing with side-edge separation is found to be a zero slope at the side edges.

(3) For aspect ratios from zero to five, the normal force predicted by the present theory using a single wing element agrees with experiment within 10 percent up to the onset of leading edge stall, which is not included in the theoretical model.

(4) The present theory evidently predicts unrealistically high values of the shedding angle for the separated vortices, particularly for high aspect ratios and low angles of attack.

(5) The predicted normal force increases with shedding angle of the separated vortices but becomes less sensitive to shedding angle as the aspect ratio increases.

7.2 Delta Wings

(1) For delta wings, the unrealistically high shedding angles evidently produce correspondingly high predicted values of normal force.

(2) If the shedding angle is held fixed, the present theory is capable of giving substantial improvement over other theories in predicting both normal force and center of pressure for aspect ratios from one to four over a wide range of angle of attack, provided an appropriate shedding angle is selected. A plot of the required shedding angle has been developed.

(3) The predicted center of pressure is relatively insensitive to the shedding angle of the separated vortices.

(4) The method appears to converge with respect to number of wing elements and harmonics, whether or not one solves for the shedding angle by iteration. For aspect ratios up to four, it appears that 8 wings and 19 nonzero harmonics suffice for 2 percent precision on normal force, provided that the separated vortices lie at least 3° above the wing surface.

(5) Convergence of the method deteriorates as the shedding angle (and consequently the angle of attack) decreases and as the aspect ratio increases. That is, larger numbers of harmonics are required for convergence at low angles of attack and/or high aspect ratios. However, linear theory suffices for those cases.

(6) The present theory affords prediction of the detailed span loading as well as the downwash everywhere in the flow field. However, accurate prediction of the span loading (and, hence, of the downwash) evidently requires larger numbers of wing elements and harmonics than does accurate prediction of the normal force and center of pressure.

(7) The span loading on a swept wing, as predicted by the
present method using 8 wings and 19 harmonics, exhibits sizeable
fictitious discontinuities at the side edge of each wing element.
However, when these were faired out, the resulting span load dis-
tribution compared well with experiment for the one case which
was calculated for an aspect ratio two delta wing at 20° angle of
attack.

(8) The present theory evidently does not predict the fall-
ing off of lift-curve slope near the stall. Thus, for delta wings
of aspect ratio three and higher, the theoretical normal force is
too high for angles of attack above 20°.

REFERENCES

1. Bollay, W.: A Non-linear Wing Theory and Its Application to Rectangular Wings of Small Aspect Ratio. Z. Angew., Math. Mech. Bd. 19 Nr., 1 Feb. 1939.

2. Betz, A.: Applied Airfoil Theory. Div. J., Chap. III, vol. IV, Aerodynamic Theory, W. F. Durand, Editor, Springer, Berlin, 1935, pp. 69-70.

3. Weinig, F.: Lift and Drag of Wings with Small Span. NACA TM 1151, Aug. 1947.

4. Gersten, K.: Nonlinear Airfoil Theory for Rectangular Wings in Compressible Flow. NASA RE 3-2-59W, Feb. 1959.

5. Scholz, N.: Beiträge Zur Theorie der Tragenden Fläche. (Contributions to the Theory of the Lifting Surface, Thesis-in German), Ing.-Archiv, XVIII Band, 2 Heft, 1950.

6. Sears, W. R.: Some Recent Developments in Airfoil Theory. Jour. of Aero. Sci., vol. 23, no. 5, May 1956.

7. Schairer, R. S.: Unsymmetrical Lift Distributions on a Stalled Monoplane Wing. Calif. Inst. of Technology, Thesis, 1939.

8. Brown, C. E. and Michael, W. H.: On Slender Delta Wings with Leading-Edge Separation. NACA TN 3430, Apr. 1955.

9. Legendre, R.: Écoulement au Voisinage de la Pointe Avant d'une Aile Forte Flèche Aux Incidences Moyennes. La Recherche Aéronautique (ONERA), No. 30, 1952, and No. 35, 1953.

10. Adams, M. C.: Leading-Edge Separation from Delta Wing at Supersonic Speeds. Readers' Forum, Jour. of Aero. Sci., vol. 20, no. 6, June 1953, p. 430.

11. Edwards, R. H.: Leading-Edge Separation from Slender Delta Wing. Readers' Forum, Jour. of Aero. Sci., vol. 21, no. 2, Feb. 1954, pp. 134-135.

12. Ward, G. N.: Linearized Theory of Steady High-Speed Flow. Cambridge Monographs on Mechanics and Applied Mechanics, Cambridge University Press, 1955.

13. Cheng, H. K.: Aerodynamics of a Rectangular Plate with Vortex Separation in Supersonic Flow. Jour. of Aero. Sci., vol. 22, no. 4, Apr. 1955.

14. Mangler, K. W. and Smith, J. H. B.: Calculation of the Flow Past Slender Delta Wings with Leading Edge Separation. RAE Rep. No. Aero. 2593, May 1957.

15. Pappas, C. E. and Kunen, A. E.: An Investigation of the Aerodynamics of Sharp Leading-Edge Swept Wings at Low Speeds. Jour. of Aero. Sci., vol. 21, no. 10, Oct. 1954.

16. Gersten, K.: Nichtlineare Tragflächentheorie Insbesondere für Tragflügel mit Kleinem Seitenverhältnis. Ingenieur - Archiv, 30 Band, 6 Heft, pp. 431-452, 1961.

17. Truckenbrodt, E.: Tragflächentheorie bei Inkompressibler Strömung. Jahrbuch 1953 der Wissenschafftlichen Gesellschaft für Luftfahrt (WGL), 1955, pp. 40-65.

18. Jones, R. T.: Properties of Low-Aspect-Ratio Pointed Wings at Speeds Below and Above the Speed of Sound. NACA Rept. 835, 1946.

19. Van Karman, Th. and Burgers, J. M.: General Aerodynamic Theory-Perfect Fluids. Chapt. 3, Div. E., Vol. II of Aero-dynamic Theory, W. F. Durand, Editor, Springer, Berlin, 1935.

20. Adams, E. P. and Hippisley, R. L.: Smithsonian Mathematical Formulae and Tables of Elliptic Functions. Smithsonian Miscellaneous Collections, vol. 74, no. 1, 1939.

21. Groebner, W. and Hofreiter, N.: Integraltofel Umbestimmte Integrale. Vol. I, Springer-Verlag, 1958.

22. Weissinger, J.: Über die Auftriebsverteilung von Pfeilflügeln. Zentrale für Wissenschaftliches Berichtswesen der Luftfahrtforschung des Generalluftzeugmeisters (ZWB) Berlin-Adlershof. Forschungsbericht Nr. 1553, den 27.2, 1942.

23. Schock, D. L.: An Investigation of the Flow Characteristics About a Low Aspect Ratio, Sharp Leading-Edge Rectangular Wing. Princeton University, Dept. of Aeronautical Engineering, Rept. no. 574, Nov. 1961.

24. Bergesen, Andrew J. and Porter, J. D.: An Investigation of the Flow Around Slender Delta Wings with Leading-Edge Separation. Princeton University, Dept. of Aeronautical Engineering. Rept. no. 510, May 1960.

25. Peckham, D. H.: Low-Speed Wind-Tunnel Tests on a Series of Uncambered Slender Pointed Wings with Sharp Edges. ARC Tech. Rept., R&M No. 3186, 1961.

26. Wick, B. E.: Chordwise and Spanwise Loadings Measured at Low Speed on a Triangular Wing Having an Aspect Ratio of Two and an NACA 0012 Airfoil Section. NACA TN 1650, June 1948.

27. Glauert, H.: The Elements of Aerofoil and Airscrew Theory. The Macmillan Co., New York, 1943, pp. 127-128.

28. Reid, E. G.: Applied Wing Theory. McGraw-Hill Book Co., Inc., New York, 1932.

29. Winter, H.: Flow Phenomena on Plates and Airfoils of Short Span. NACA TM 798, July 1936.

30. LaVallee, R. S.: Wind Tunnel Tests on Wedge-Shaped Wings. Rept. R-5503-2, United Aircraft Corp., Research Dept., Jan. 1947.

APPENDIX A

UPWASH INDUCED BY A HORSESHOE VORTEX
## LYING ABOVE THE WING

To determine the upwash w induced at an arbitrary point
(x,y,z) by a horseshoe vortex which is inclined to the wing
surface, let us consider the following sketch:
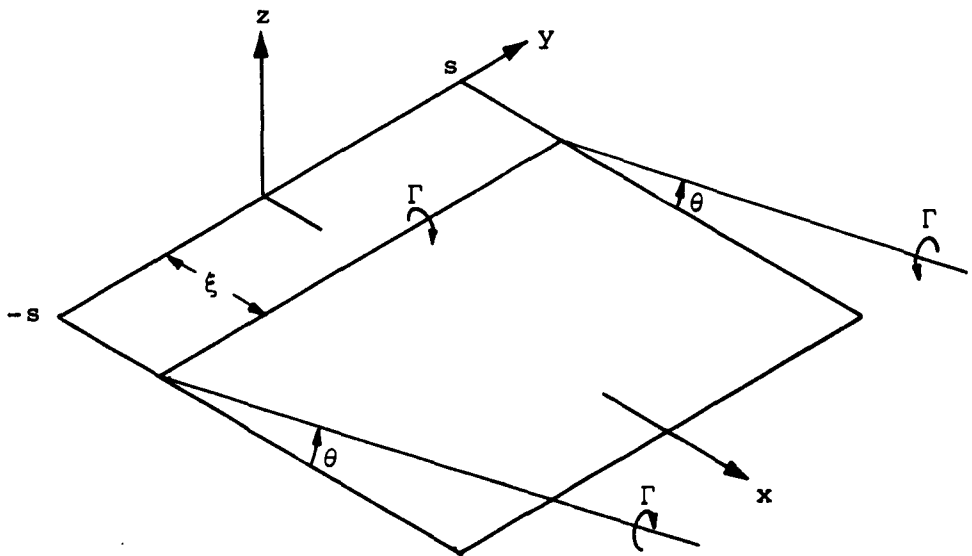
Here we have a rectangular wing of semispan s lying in the x,y
plane and a horseshoe vortex of strength Γ. This vortex consists
of three parts, a bound part, of semispan s, lying in the plane
of the wing at a distance ξ behind the leading edge, and a right
and left trailing vortex each of which is inclined at an angle θ
to the wing as shown. Let us divide the upwash w produced at
point (x,y,z) into the components produced by each part of the
horseshoe vortex. That is, let

$$w(x,y,z) = w_B(x,y,z) + w_R(x,y,z) + w_L(x,y,z) \qquad \text{(A.1)}$$

The upwash induced by the bound vortex can be determined with the aid of the following sketch:
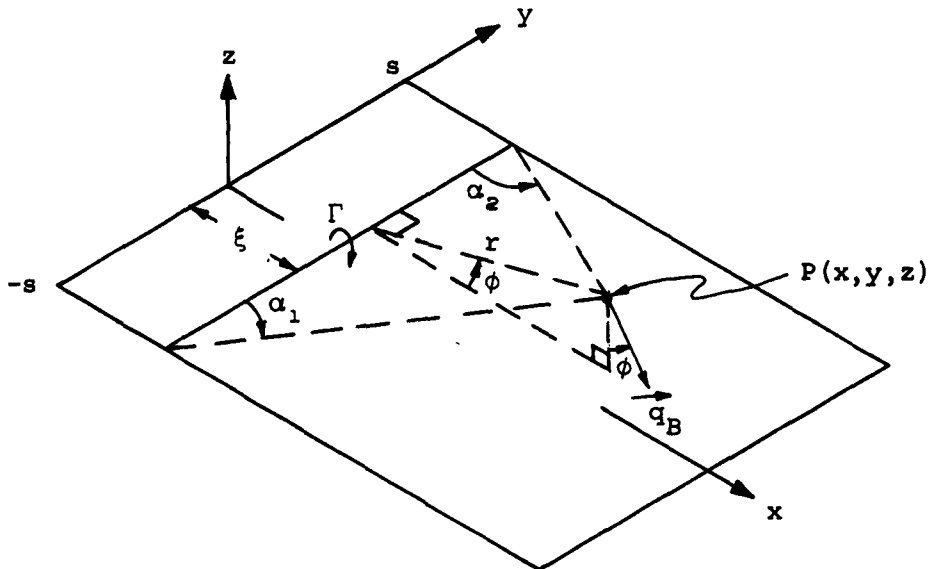
Thus, the total velocity induced at point P by the bound vortex of span $2s$ is (Ref. 27)

$$\vec{q}_B = \frac{\Gamma}{4\pi r} (\cos \alpha_1 + \cos \alpha_2) \, \vec{i}_{q_B} \qquad (A.2)$$

where $\vec{i}_{q_B}$ is the unit vector in the direction of $\vec{q}_B$. Hence the upwash in the positive z direction is given by (see sketch)

$$w_B = \vec{q}_B \cdot \vec{i}_z$$

$$= - \left| \vec{q}_B \right| \cos \phi = - \frac{\Gamma \cos \phi}{4\pi r} (\cos \alpha_1 + \cos \alpha_2) \qquad (A.3)$$

where $\vec{i}_z$ is the unit vector in the z direction.

The preceding sketch yields the following relationships:

$$r = \frac{x - \xi}{\cos \phi}$$

$$\cos \phi = \frac{x - \xi}{\sqrt{(x - \xi)^2 + z^2}}$$

$$\cos \alpha_1 = \frac{s + y}{\sqrt{(x - \xi)^2 + (s + y)^2 + z^2}}$$

$$\cos \alpha_2 = \frac{s - y}{\sqrt{(x - \xi)^2 + (s - y)^2 + z^2}}$$

(A.4)

so that substitution into Equation (A.3) gives

$$w_B = -\frac{\Gamma(x - \xi)}{4\pi\left[(x - \xi)^2 + z^2\right]}\left[\frac{s + y}{\sqrt{(x - \xi)^2 + (s + y)^2 + z^2}}\right.$$

$$\left. + \frac{s - y}{\sqrt{(x - \xi)^2 + (s - y)^2 + z^2}}\right]$$

(A.5)

The next component of the upwash at point P to be determined is that due to the right trailing vortex. For this purpose let us look at the next sketch.
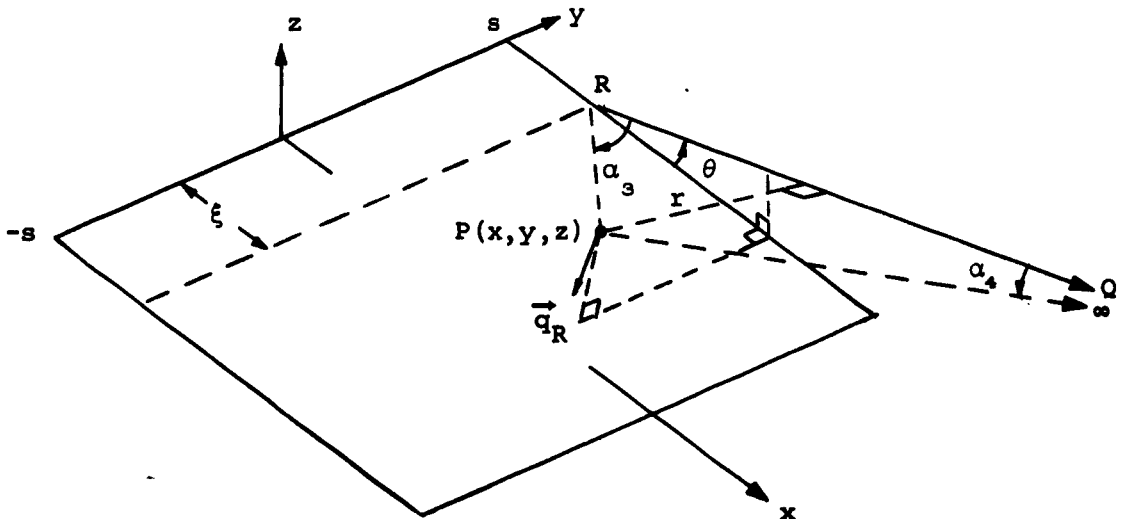
If we apply the relationship given by Equation (A.2) to this case, we have

$$\vec{q}_R = \frac{\Gamma}{4\pi r} (\cos \alpha_3 + \cos \alpha_4) \vec{i}_{q_R} \tag{A.6}$$

where $\vec{i}_{q_R}$ is the unit vector. Since the vortex we are dealing with is semi-infinite, α_4 approaches zero degrees and

$$\cos \alpha_4 = 1.0 \tag{A.7}$$

Let us now write the expressions for two unit vectors, one in the direction R to Q and the other in the direction R to P. These are

$$\vec{i}_{RQ} = \cos \theta \, \vec{i}_x + \sin \theta \, \vec{i}_z \tag{A.8}$$

and

$$\vec{i}_{RP} = \frac{(x - \xi)\vec{i}_x - (s - y)\vec{i}_y + z\vec{i}_z}{\sqrt{(x - \xi)^2 + (s - y)^2 + z^2}} \tag{A.9}$$

From these two unit vectors we find

$$\cos \alpha_3 = \vec{i}_{RQ} \cdot \vec{i}_{RP} = \frac{(x - \xi)\cos \theta + z \sin \theta}{\sqrt{(x - \xi)^2 + (s - y)^2 + z^2}} \tag{A.10}$$

$$r = \left| \vec{RP} \right| \sin \alpha_3 = \left| \vec{RP} \right| \sqrt{1 - \cos^2 \alpha_3}$$

$$= \left\{ (s - y)^2 + \left[(x - \xi)\sin \theta - z \cos \theta \right]^2 \right\}^{1/2} \tag{A.11}$$

and

$$\vec{i}_{q_R} = \frac{\vec{i}_{RQ} \times \vec{i}_{RP}}{\sin \alpha_3} = \frac{\vec{i}_{RQ} \times \vec{RP}}{r}$$

This cross product is, from Equations (A.8) and (A.9)

$$\frac{\vec{I}_{RQ} \times \vec{RP}}{r} = \frac{1}{r}\left\{(s - y)\sin\theta\ \vec{I}_x + \left[(x - \xi)\sin\theta - z\cos\theta\right]\vec{I}_y \right.$$
$$\left. - (s - y)\cos\theta\ \vec{I}_z\right\} \tag{A.12}$$

Therefore, substitution of Equations (A.7), (A.10), (A.11), and (A.12) into Equation (A.6) will give the expression for $\vec{q}_R$. Thus, for the upwash induced at P (i.e., the component of $\vec{q}_R$ in the $\vec{I}_z$ direction), we find

$$w_R = \vec{q}_R \cdot \vec{I}_z$$
$$= -\frac{\Gamma}{4\pi}\left\{\frac{(s - y)\cos\theta}{(s - y)^2 + \left[(x - \xi)\sin\theta - z\cos\theta\right]^2}\right\}$$
$$\left[\frac{(x - \xi)\cos\theta + z\sin\theta}{\sqrt{(x - \xi)^2 + (s - y)^2 + z^2}} + 1\right] \tag{A.13}$$

From symmetry considerations, the expression for the upwash induced at point P by the left trailing vortex can immediately be written as

$$w_L = -\frac{\Gamma}{4\pi}\left\{\frac{(s + y)\cos\theta}{(s + y)^2 + \left[(x - \xi)\sin\theta - z\cos\theta\right]^2}\right\}$$
$$\left[\frac{(x - \xi)\cos\theta + z\sin\theta}{\sqrt{(x - \xi)^2 + (s + y)^2 + z^2}} + 1\right] \tag{A.14}$$

Finally, the total upwash w due to the horseshoe vortex of strength Γ shown in the first sketch of this appendix is

$$w = w_B + w_R + w_L$$

where

$$w_B = -\frac{\Gamma(x-\xi)}{4\pi\left[(x-\xi)^2 + z^2\right]}\left[\frac{s+y}{\sqrt{(x-\xi)^2 + (s+y)^2 + z^2}}\right.$$

$$\left. + \frac{s-y}{\sqrt{(x-\xi)^2 + (s-y)^2 + z^2}}\right]$$

$$w_R = -\frac{\Gamma}{4\pi}\left\{\frac{(s-y)\cos\theta}{(s-y)^2 + \left[(x-\xi)\sin\theta - z\cos\theta\right]^2}\right\}$$

$$\left[\frac{(x-\xi)\cos\theta + z\sin\theta}{\sqrt{(x-\xi)^2 + (s-y)^2 + z^2}} + 1\right]$$

$$w_L = -\frac{\Gamma}{4\pi}\left\{\frac{(s+y)\cos\theta}{(s+y)^2 + \left[(x-\xi)\sin\theta - z\cos\theta\right]^2}\right\}$$

$$\left[\frac{(x-\xi)\cos\theta + z\sin\theta}{\sqrt{(x-\xi)^2 + (s+y)^2 + z^2}} + 1\right]$$

(A.15)

APPENDIX B

INFLUENCE OF THE GROUND PLANE

If the wing in question is in the proximity of a ground plane, then the upwash at the wing surface will be altered in the same fashion as if the ground plane were replaced by an inverted "image" wing located as shown in the sketch below (Ref. 28):
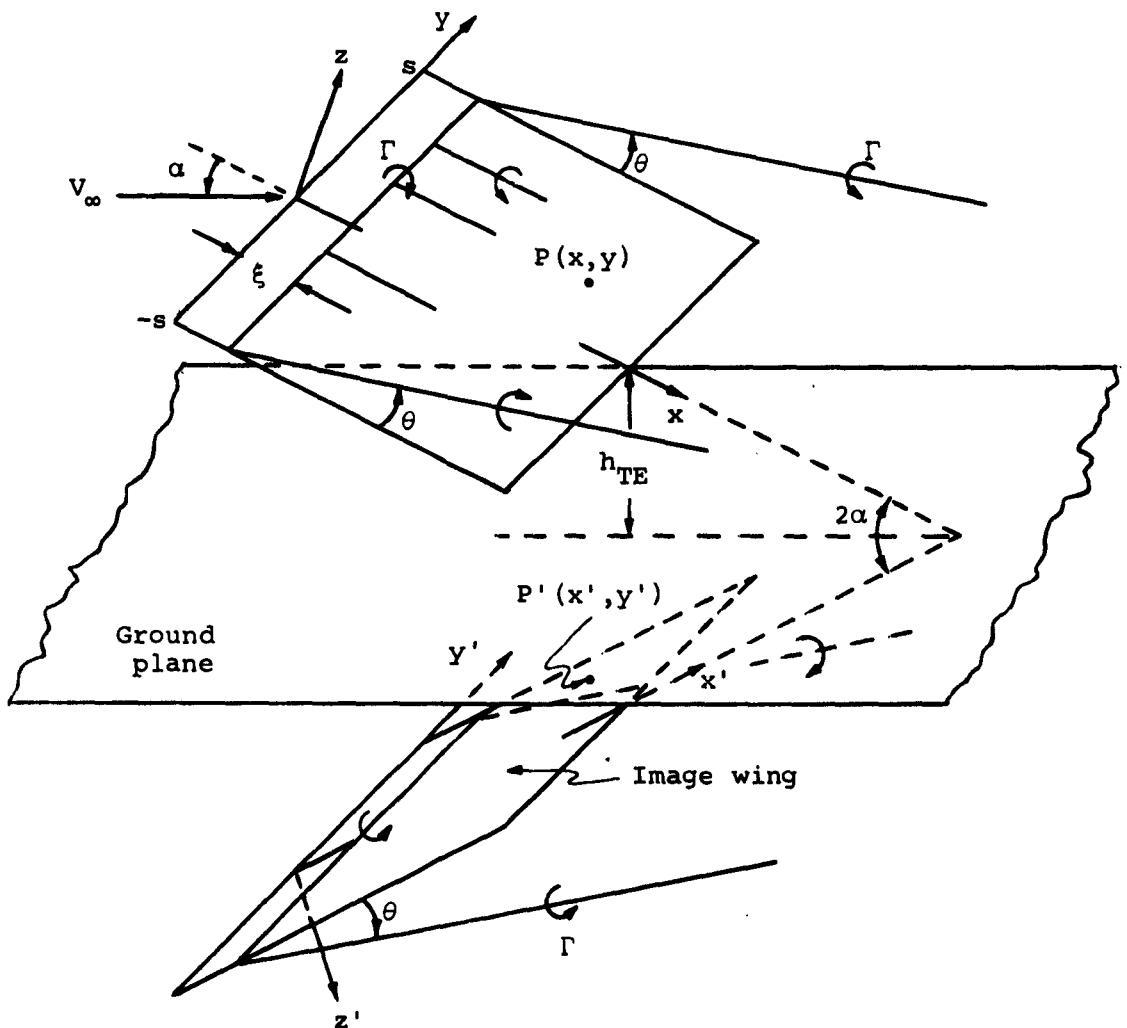
Thus, we can rewrite the boundary condition of no flow through the wing surface (Eq. (9)) in the form

$$w^*(x_p, y_p) + \bar{w}(x_p, y_p) + w_g^*(x_p, y_p) + \bar{w}_g(x_p, y_p) = - V_\infty \sin \alpha$$

$$(B.1)$$

where the subscript g denotes the contribution of the ground plane or image system.

It can be seen from the above sketch that the z component of the velocity produced at point $P(x, y)$ on the wing by the image system is equal to the z' component of velocity produced at the image point $P'(x', y')$ by the actual vortex system associated with the real wing. Therefore, we can determine the upwash $w_g^*(x, y)$ and $\bar{w}_g(x, y)$ of Equation (B.1) by writing expressions for the velocity component in the z' direction produced at the image point P' by the actual wing. For this purpose, it can be seen from the sketch below that we shall require both the x and z components of velocity induced at the point P'.
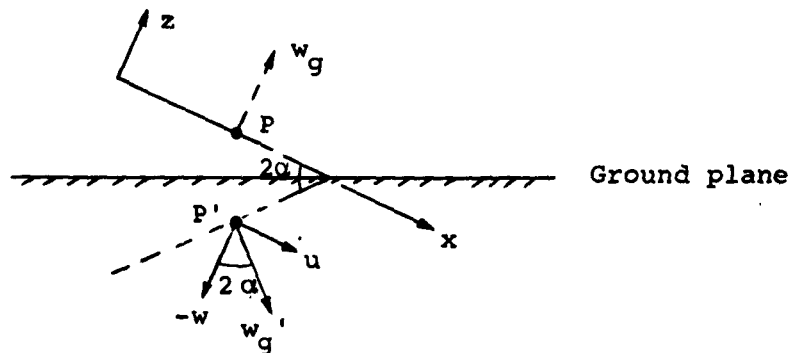

That is,

$$w_g = w_g' = -w \cos 2\alpha + u \sin 2\alpha \qquad (B.2)$$

where w and u are the z and x components of velocity induced at P'.

The coordinates x_i, y_i, z_i (in the x, y, z system) of the image point P' are required for use in the general expressions for w and u. But, since the y coordinate of the image point is the same as that for the corresponding point in the wing itself, we have

$$y_i = y \qquad (B.3)$$

The coordinates x_i and z_i can be obtained from the following sketch, which is a cut through the $y = y_i$ plane.
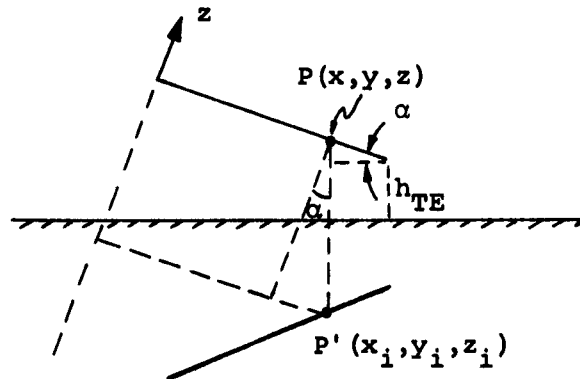
Thus, we see that

$$z_i = -2 \left[h_{TE} + (c - x)\sin \alpha \right] \cos \alpha \qquad (B.4)$$

and

$$x_i = x - z_i \tan \alpha = x + 2 \left[h_{TE} + (c - x)\sin \alpha \right] \sin \alpha$$

$$(B.5)$$

Having the coordinates x_i, y_i, z_i of the image point P', as given by Equations (B.3), (B.4), and (B.5), we can now express the u and w velocity components at that point by using the results of Appendix A. Thus, the w component is given directly by Equations (A.15) if we replace x by x_i and z by z_i. Similarly, the u components at point $P(x, y, z)$ are obtained from Equations (A.2) and (A.6) by writing the appropriate dot products of the velocity vectors. Thus, from Equation (A.2), we have (see sketch, p. A-2)

$$u_B = \vec{q}_B \cdot \vec{i}_x$$

$$= \left| \vec{q}_B \right| \sin \phi = \frac{\Gamma \sin \phi}{4\pi r} (\cos \alpha_1 + \cos \alpha_2) \tag{B.6}$$

Therefore, using the relationships of Equation (A.4), we find that

$$u_B = \frac{\Gamma z}{4\pi \left[(x - \xi)^2 + z^2 \right]} \left[\frac{s + y}{\sqrt{(x - \xi)^2 + (s + y)^2 + z^2}} \right.$$

$$\left. + \frac{s - y}{\sqrt{(x - \xi)^2 + (s - y)^2 + z^2}} \right] \tag{B.7}$$

By the same procedure, we find from Equations (A.6) through (A.12) that

$$u_R = \vec{q}_R \cdot \vec{i}_x$$

$$= \frac{\Gamma}{4\pi} \left\{ \frac{(s - y)\sin \theta}{(s - y)^2 + \left[(x - \xi)\sin \theta - z \cos \theta \right]^2} \right\}$$

$$\left[\frac{(x - \xi)\cos \theta + z \sin \theta}{\sqrt{(x - \xi)^2 + (s - y)^2 + z^2}} + 1 \right] \tag{B.8}$$

From symmetry considerations, the corresponding expression for u_L induced at P by the left trailing vortex can immediately be written as

$$u_L = \frac{\Gamma}{4\pi} \left\{ \frac{(s + y)\sin \theta}{(s + y)^2 + \left[(x - \xi)\sin \theta - z \cos \theta\right]^2} \right\}$$

$$\left[\frac{(x - \xi)\cos \theta + z \sin \theta}{\sqrt{(x - \xi)^2 + (s + y)^2 + z^2}} + 1 \right] \tag{B.9}$$

Finally, the u and w components induced at the image point P'(x_i, y_i, z_i) are obtained directly from Equations (A.15), (B.7), (B.8), and (B.9) by simply replacing x and z by x_i and z_i as given by Equations (B.4) and (B.5). Then the actual upwash w_g produced at the point P by the image wing (i.e., by the ground plane) is given by Equation (B.2).

It must be recalled that the above expressions give only the velocities induced by a single vortex, whereas the additional upwash components required in the boundary condition of Equation (B.1) are those produced by the entire vortex system associated with the image wing. Therefore, in order to obtain w_g^* and $\overline{w}_g$, we must integrate the above expressions in a manner analogous to that employed in the main body of the present report (see Sections 4.2.2 and 4.2.3). The integrations required will, of course, be more difficult than those of the main analysis, since they now involve points lying out of the plane of the wing (i.e., $z \neq 0$).

Inasmuch as the detailed analysis and programing of the influence of the ground plane represents a formidable task, it is well to re-examine the validity of the assumptions made in this analysis before embarking on such an endeavor. That is, one should perhaps first consider whether the mathematical model is sufficiently realistic to justify this extension. In particular, it is pointed out that the shed vortices associated with the lifting line are assumed to extend in the chordwise direction

while the separated vortices are assumed to be shed at an angle θ above the wing. Even in the absence of a ground plane, this assumption is of course an approximation to the real vortex system in which the vortices roll up into two concentrated cores. But as the wing approaches the ground, an additional complication arises which is not accounted for in the present analysis. The shed vortices are deflected upward by the influence of the ground plane and are also driven outward in the manner of a vortex ring which expands when approaching a flat surface. This latter effect has been observed experimentally behind a delta wing model. These effects will, of course, become increasingly important as the ground plane is approached, but their quantitative effect upon the calculated results is not known.

TABLE I.- DOWNWASH IN WAKE BEHIND ELLIPTICALLY LOADED LIFTING LINE.

$\dfrac{x-\xi_i}{s}$ ╲ $\dfrac{y}{s}$	$\left(-\dfrac{w^*}{V_\infty}\right)\Big/\left(\dfrac{\gamma_1}{4\pi s V_\infty}\right)$				
	0	.25	.50	.75	1.0
0	∞	∞	∞	∞	∞
.25	11.9556	11.7484	11.1091	10.0024	8.5199
.50	8.412	8.3407	8.1313	7.8053	7.4289
.75	7.396	7.3651	7.2766	7.1434	6.9902
1.0	6.9618	6.9446	6.9039	6.8398	6.7645
∞	2π	2π	2π	2π	2π

(a) Normal force coefficient, C_N.

n_h \ A	0.5	1.0	2.0	5.0	10.0	20.0
			$\alpha = 10°$			
2	0.20000	0.27389	0.36855	0.50624	0.59015	0.64592
4	.22054	.34797	.53439	.79532	.93393	1.01222
6	.22062	.34714	.53126	.80581	.96298	1.05155
8	.22062	.34717	.53110	.80490	.97091	1.07273
10	.22062	.34717	.53113	.80428	.97122	1.08140
12	.22062	.34717	.53113	.80424	.97054	1.08367
14	.22062	.34717	.53113	.80426	.97023	1.08364
			$\alpha = 20°$			
2	0.52900	0.70979	0.90730	1.14926	1.28317	1.36875
4	.53631	.77896	1.12889	1.64101	1.91084	2.04682
6	.53631	.77922	1.12623	1.64092	1.95365	2.13664
8	.53631	.77921	1.12632	1.63916	1.95403	2.16498
10	.53631	.77921	1.12632	1.63925	1.95239	2.16810
12	.53632	.77922	1.12632	1.63928	1.95224	2.16665
14	.53631	.77922	1.12632	1.63928	1.95232	2.16584

TABLE II.- CONTINUED.

(b) Center of pressure, $\overline{x}/c$

n_h \ A	0.5	1.0	2.0	5.0	10.0	20.0
			$\alpha = 10^{\circ}$			
2	0.45637	0.41864	0.37608	0.33097	0.31059	0.29914
4	.45663	.42380	.38891	.34560	.31963	.30101
6	.45651	.42328	.39072	.35812	.33837	.31990
8	.45651	.42329	.39042	.35872	.34395	.33061
10	.45651	.42329	.39044	.35835	.34456	.33509
12	.45651	.42329	.39044	.35828	.34427	.33636
14	.45651	.42329	.39044	.35829	.34409	.33642
			$\alpha = 20^{\circ}$			
2	0.48239	0.45755	0.42277	0.37606	0.35051	0.33463
4	.48215	.45781	.42766	.38832	.36067	.33703
6	.48216	.45769	.42716	.39269	.37487	.35795
8	.48216	.45769	.42716	.39221	.37573	.36490
10	.48216	.45769	.42716	.39219	.37532	.36582
12	.48216	.45769	.42716	.39219	.37524	.36550
14	.48216	.45769	.42716	.39219	.37524	.36528

TABLE II.- CONCLUDED.

(c) Strength of shed vorticity, Γ^*.

$\alpha = 10°$

n_h \ A	0.5	1.0	2.0	5.0	10.0	20.0
2	0.153657	0.085974	0.043245	0.015259	0.006655	0.002954
4	.169640	.112566	.069084	.028305	.012104	.004806
6	.169607	.111967	.069575	.032434	.015840	.006841
8	.169606	.111983	.069409	.032578	.016979	.008047
10	.169606	.111983	.069419	.032442	.017095	.008564
12	.169606	.111983	.069420	.032419	.017030	.008710
14	.169606	.111983	.069420	.032423	.016992	.008715

$\alpha = 20°$

n_h \ A	0.5	1.0	2.0	5.0	10.0	20.0
2	0.243507	0.145907	0.077626	0.028698	0.012773	0.005736
4	.246621	.160320	.099317	.044963	.020944	.008821
6	.246628	.160280	.098802	.046379	.024162	.011422
8	.246629	.160280	.098815	.046173	.024333	.012319
10	.246628	.160280	.098815	.046169	.024233	.012435
12	.246629	.160281	.098815	.046172	.024215	.012393
14	.246628	.160280	.098815	.046172	.024217	.012365

TABLE III.- CALCULATED LOADING COEFFICIENTS FOR AN
ISOLATED RECTANGULAR WING ELEMENT OF ASPECT RATIO 3.5
($\alpha = 20^{\circ}$, $\theta = 10^{\circ}$, $n_h = 19$, $x_c/c = 0.75$).

n	$\left(\gamma_n^*\right)_u$	$\left(\gamma_n^*\right)_S$	γ_n^*
1	9.7049×10^{-2}	-7.4834×10^{-1}	4.9849×10^{-2}
3	1.0241×10^{-2}	-4.8942×10^{-1}	-2.0628×10^{-2}
5	1.2764×10^{-4}	-2.6161×10^{-1}	-1.6374×10^{-2}
7	-1.3987×10^{-4}	-1.2853×10^{-1}	-8.2470×10^{-3}
9	-2.5040×10^{-5}	-5.5478×10^{-2}	-3.5243×10^{-3}
11	4.9398×10^{-7}	-1.9203×10^{-2}	-1.2108×10^{-3}
13	1.3147×10^{-6}	-3.7588×10^{-3}	-2.3577×10^{-4}
15	2.9635×10^{-7}	1.3218×10^{-3}	8.3671×10^{-5}
17	9.8930×10^{-9}	2.0750×10^{-3}	1.3089×10^{-4}
19	-2.8367×10^{-9}	1.4869×10^{-3}	9.3786×10^{-5}
21	-3.7550×10^{-8}	7.7604×10^{-4}	4.8911×10^{-5}
23	1.8738×10^{-8}	2.9531×10^{-4}	1.8645×10^{-5}
25	2.5503×10^{-9}	5.3567×10^{-5}	3.3813×10^{-6}
27	-1.1670×10^{-8}	-3.4224×10^{-5}	-2.1704×10^{-6}
29	-6.4205×10^{-9}	-4.7103×10^{-5}	-2.9774×10^{-6}
31	-3.3350×10^{-9}	-3.4346×10^{-5}	-2.1697×10^{-6}
33	7.2535×10^{-9}	-1.8373×10^{-5}	-1.1516×10^{-6}
35	-1.4820×10^{-8}	-2.3315×10^{-6}	-1.6188×10^{-7}
37	-7.7647×10^{-11}	2.8269×10^{-6}	1.7823×10^{-7}

TABLE IV.- CALCULATED LOADING COEFFICIENTS FOR EACH RECTANGULAR WING ELEMENT OF A DELTA WING OF ASPECT RATIO 2.0 ($\alpha = 20^\circ$, $\theta_i = 10^\circ$, $(x_c/c)_i = 0.75$, $n_h = 19$).

(a) Wing element number 1.

n	$\left(\gamma_n^*\right)_u$	$\left(\gamma_n^*\right)_S$	γ_n^*
1	0.2155	−0.5293	0.3392×10^{-1}
3	$-.1248\times10^{-3}$	$-.9414\times10^{-1}$	$-.3242\times10^{-1}$
5	$-.1106\times10^{-4}$	$-.5724\times10^{-2}$	$-.1975\times10^{-2}$
7	$.2877\times10^{-6}$	$.1199\times10^{-2}$	$.4117\times10^{-3}$
9	$-.2560\times10^{-8}$	$.2273\times10^{-3}$	$.7798\times10^{-4}$
11	$-.2697\times10^{-9}$	$-.1943\times10^{-4}$	$-.6668\times10^{-5}$
13	$.3009\times10^{-8}$	$-.9041\times10^{-5}$	$-.3099\times10^{-5}$
15	$.1324\times10^{-9}$	$.1016\times10^{-7}$	$.3621\times10^{-8}$
17	$-.1151\times10^{-8}$	$.3423\times10^{-6}$	$.1163\times10^{-6}$
19	$.2171\times10^{-8}$	$.1988\times10^{-7}$	$.8995\times10^{-8}$
21	$-.6955\times10^{-9}$	$-.2789\times10^{-7}$	$-.1026\times10^{-7}$
23	$.3579\times10^{-9}$	$.7980\times10^{-8}$	$.3096\times10^{-8}$
25	$-.3787\times10^{-9}$	$.9309\times10^{-8}$	$.2815\times10^{-8}$
27	$.1605\times10^{-8}$	$-.9566\times10^{-8}$	$-.1676\times10^{-8}$
29	$.2140\times10^{-8}$	$-.8673\times10^{-8}$	$-.8358\times10^{-9}$
31	$-.1896\times10^{-8}$	$.6237\times10^{-8}$	$.2434\times10^{-9}$
33	$-.1955\times10^{-9}$	$.8279\times10^{-8}$	$.2645\times10^{-8}$
35	$-.8298\times10^{-8}$	$.1249\times10^{-6}$	$.3458\times10^{-7}$
37	$.5229\times10^{-8}$	$-.1171\times10^{-6}$	$-.3496\times10^{-7}$

TABLE IV.- CONTINUED.

(b) Wing element number 2.

n	$\left(\gamma_n{}^*\right)_u$	$\left(\gamma_n{}^*\right)_S$	$\gamma_n{}^*$
1	0.1584	−0.6940	0.3924×10^{-1}
3	$.6306 \times 10^{-1}$	−.3015	$.1126 \times 10^{-1}$
5	$-.4885 \times 10^{-1}$	−.1012	$-.6625 \times 10^{-1}$
7	$.3059 \times 10^{-1}$	$-.2411 \times 10^{-1}$	$.2645 \times 10^{-1}$
9	$-.1599 \times 10^{-1}$	$-.1648 \times 10^{-2}$	$-.1628 \times 10^{-1}$
11	$.6325 \times 10^{-2}$	$.1864 \times 10^{-2}$	$.6645 \times 10^{-2}$
13	$-.4304 \times 10^{-3}$	$.1119 \times 10^{-2}$	$-.2380 \times 10^{-3}$
15	$-.2920 \times 10^{-2}$	$.3221 \times 10^{-3}$	$-.2865 \times 10^{-2}$
17	$.4364 \times 10^{-2}$	$.1190 \times 10^{-4}$	$.4366 \times 10^{-2}$
19	$-.4204 \times 10^{-2}$	$-.3980 \times 10^{-4}$	$-.4210 \times 10^{-2}$
21	$.2817 \times 10^{-2}$	$-.2279 \times 10^{-4}$	$.2814 \times 10^{-2}$
23	$-.8444 \times 10^{-3}$	$-.6200 \times 10^{-5}$	$-.8454 \times 10^{-3}$
25	$-.9381 \times 10^{-3}$	$.1882 \times 10^{-6}$	$-.9381 \times 10^{-3}$
27	$.1890 \times 10^{-2}$	$.1051 \times 10^{-5}$	$.1890 \times 10^{-2}$
29	$-.1766 \times 10^{-2}$	$.5290 \times 10^{-6}$	$-.1766 \times 10^{-2}$
31	$.7988 \times 10^{-3}$	$.1458 \times 10^{-6}$	$.7988 \times 10^{-3}$
33	$.4269 \times 10^{-3}$	$.1400 \times 10^{-7}$	$.4269 \times 10^{-3}$
35	$-.8806 \times 10^{-3}$	$.2557 \times 10^{-6}$	$-.8806 \times 10^{-3}$
37	$.3724 \times 10^{-3}$	$-.3111 \times 10^{-6}$	$.3723 \times 10^{-3}$

TABLE IV.- CONTINUED.

(c) Wing element number 3.

n	$\left(\gamma_n{}^*\right)_u$	$\left(\gamma_n{}^*\right)_S$	$\gamma_n{}^*$
1	0.9065×10^{-1}	-0.7347	0.3776×10^{-2}
3	$.1178$	$-.4157$	$.6868 \times 10^{-1}$
5	$-.2504 \times 10^{-1}$	$-.1917$	$-.4771 \times 10^{-1}$
7	$-.4153 \times 10^{-1}$	$-.7680 \times 10^{-1}$	$-.5061 \times 10^{-1}$
9	$.4409 \times 10^{-1}$	$-.2399 \times 10^{-1}$	$.4126 \times 10^{-1}$
11	$-.1425 \times 10^{-1}$	$-.3903 \times 10^{-2}$	$-.1471 \times 10^{-1}$
13	$-.8608 \times 10^{-2}$	$.1560 \times 10^{-2}$	$-.8424 \times 10^{-2}$
15	$.1121 \times 10^{-1}$	$.1873 \times 10^{-2}$	$.1143 \times 10^{-1}$
17	$-.2247 \times 10^{-2}$	$.1060 \times 10^{-2}$	$-.2121 \times 10^{-2}$
19	$-.4651 \times 10^{-2}$	$.3971 \times 10^{-3}$	$-.4604 \times 10^{-2}$
21	$.3053 \times 10^{-2}$	$.7052 \times 10^{-4}$	$.3061 \times 10^{-2}$
23	$.3506 \times 10^{-2}$	$-.3419 \times 10^{-4}$	$.3502 \times 10^{-2}$
25	$-.7061 \times 10^{-2}$	$-.4214 \times 10^{-4}$	$-.7066 \times 10^{-2}$
27	$.3765 \times 10^{-2}$	$-.2472 \times 10^{-4}$	$.3762 \times 10^{-2}$
29	$.2521 \times 10^{-2}$	$-.9463 \times 10^{-5}$	$.2520 \times 10^{-2}$
31	$-.5000 \times 10^{-2}$	$-.1617 \times 10^{-5}$	$-.5001 \times 10^{-2}$
33	$.1624 \times 10^{-2}$	$.7652 \times 10^{-6}$	$.1624 \times 10^{-2}$
35	$.1778 \times 10^{-2}$	$.1922 \times 10^{-5}$	$.1778 \times 10^{-2}$
37	$-.1139 \times 10^{-2}$	$.3864 \times 10^{-6}$	$-.1139 \times 10^{-2}$

TABLE IV.- CONTINUED.

(d) Wing element number 4.

n	$\left(\gamma_n^*\right)_u$	$\left(\gamma_n^*\right)_s$	γ_n^*
1	0.6064×10^{-1}	-0.7483	-0.7796×10^{-2}
3	$.1080$	$-.4894$	$.6326 \times 10^{-1}$
5	$.2722 \times 10^{-1}$	$-.2616$	$.3293 \times 10^{-2}$
7	$-.5315 \times 10^{-1}$	$-.1285$	$-.6490 \times 10^{-1}$
9	$-.1071 \times 10^{-1}$	$-.5547 \times 10^{-1}$	$-.1578 \times 10^{-1}$
11	$.3937 \times 10^{-1}$	$-.1920 \times 10^{-1}$	$.3762 \times 10^{-1}$
13	$-.4958 \times 10^{-2}$	$-.3758 \times 10^{-2}$	$-.5301 \times 10^{-2}$
15	$-.2755 \times 10^{-1}$	$.1322 \times 10^{-2}$	$-.2743 \times 10^{-1}$
17	$.1824 \times 10^{-1}$	$.2075 \times 10^{-2}$	$.1843 \times 10^{-1}$
19	$.5509 \times 10^{-2}$	$.1486 \times 10^{-2}$	$.5645 \times 10^{-2}$
21	$-.7850 \times 10^{-2}$	$.7758 \times 10^{-3}$	$-.7779 \times 10^{-2}$
23	$-.3288 \times 10^{-2}$	$.2954 \times 10^{-3}$	$-.3261 \times 10^{-2}$
25	$.1978 \times 10^{-2}$	$.5360 \times 10^{-4}$	$.1983 \times 10^{-2}$
27	$.7397 \times 10^{-2}$	$-.3428 \times 10^{-4}$	$.7394 \times 10^{-2}$
29	$-.3141 \times 10^{-2}$	$-.4726 \times 10^{-4}$	$-.3146 \times 10^{-2}$
31	$-.9005 \times 10^{-2}$	$-.3440 \times 10^{-4}$	$-.9008 \times 10^{-2}$
33	$.5349 \times 10^{-2}$	$-.1831 \times 10^{-4}$	$.5347 \times 10^{-2}$
35	$.5580 \times 10^{-2}$	$-.1887 \times 10^{-5}$	$.5580 \times 10^{-2}$
37	$-.4149 \times 10^{-2}$	$.2268 \times 10^{-5}$	$-.4149 \times 10^{-2}$

TABLE IV.- CONTINUED.

(e) Wing element number 5.

n	$\left(\gamma_n{}^*\right)_u$	$\left(\gamma_n{}^*\right)_S$	$\gamma_n{}^*$
1	0.3559×10^{-1}	-0.7527	-0.1859×10^{-1}
3	$.8851\times10^{-1}$	$-.5412$	$.4956\times10^{-1}$
5	$.6267\times10^{-1}$	$-.3170$	$.3985\times10^{-1}$
7	$-.3505\times10^{-1}$	$-.1743$	$-.4760\times10^{-1}$
9	$-.4086\times10^{-1}$	$-.8825\times10^{-1}$	$-.4721\times10^{-1}$
11	$.1596\times10^{-1}$	$-.3933\times10^{-1}$	$.1312\times10^{-1}$
13	$.3099\times10^{-1}$	$-.1406\times10^{-1}$	$.2998\times10^{-1}$
15	$-.1223\times10^{-1}$	$-.2687\times10^{-2}$	$-.1243\times10^{-1}$
17	$-.2307\times10^{-1}$	$.1385\times10^{-2}$	$-.2297\times10^{-1}$
19	$.1712\times10^{-1}$	$.2132\times10^{-2}$	$.1728\times10^{-1}$
21	$.4498\times10^{-2}$	$.1682\times10^{-2}$	$.4619\times10^{-2}$
23	$-.6930\times10^{-2}$	$.1015\times10^{-2}$	$-.6857\times10^{-2}$
25	$.3880\times10^{-2}$	$.4886\times10^{-3}$	$.3915\times10^{-2}$
27	$-.8885\times10^{-2}$	$.1688\times10^{-3}$	$-.8873\times10^{-2}$
29	$.4527\times10^{-2}$	$.1365\times10^{-4}$	$.4528\times10^{-2}$
31	$.1052\times10^{-1}$	$-.3891\times10^{-4}$	$.1052\times10^{-1}$
33	$-.9162\times10^{-2}$	$-.3805\times10^{-4}$	$-.9165\times10^{-2}$
35	$-.3712\times10^{-2}$	$-.4074\times10^{-4}$	$-.3715\times10^{-2}$
37	$.4023\times10^{-2}$	$-.2812\times10^{-4}$	$.4021\times10^{-2}$

TABLE IV.- CONTINUED.

(f) Wing element number 6.

n	$\left(\gamma_n{}^*\right)_u$	$\left(\gamma_n{}^*\right)_S$	$\gamma_n{}^*$
1	0.2618×10^{-1}	-0.7535	-0.1827×10^{-1}
3	$.7148 \times 10^{-1}$	$-.5794$	$.3728 \times 10^{-1}$
5	$.6104 \times 10^{-1}$	$-.3623$	$.3966 \times 10^{-1}$
7	$-.1285 \times 10^{-2}$	$-.2143$	$-.1393 \times 10^{-1}$
9	$-.4052 \times 10^{-1}$	$-.1195$	$-.4757 \times 10^{-1}$
11	$-.2327 \times 10^{-1}$	$-.6118 \times 10^{-1}$	$-.2688 \times 10^{-1}$
13	$.3458 \times 10^{-1}$	$-.2744 \times 10^{-1}$	$.3296 \times 10^{-1}$
15	$.1702 \times 10^{-1}$	$-.9671 \times 10^{-2}$	$.1645 \times 10^{-1}$
17	$-.1744 \times 10^{-1}$	$-.1446 \times 10^{-2}$	$-.1752 \times 10^{-1}$
19	$-.1421 \times 10^{-1}$	$.1593 \times 10^{-2}$	$-.1412 \times 10^{-1}$
21	$.7034 \times 10^{-2}$	$.2156 \times 10^{-2}$	$.7161 \times 10^{-2}$
23	$.8889 \times 10^{-2}$	$.1756 \times 10^{-2}$	$.8992 \times 10^{-2}$
25	$-.1244 \times 10^{-2}$	$.1143 \times 10^{-2}$	$-.1176 \times 10^{-2}$
27	$.2460 \times 10^{-2}$	$.6236 \times 10^{-3}$	$.2496 \times 10^{-2}$
29	$-.1128 \times 10^{-1}$	$.2782 \times 10^{-3}$	$-.1127 \times 10^{-1}$
31	$-.1129 \times 10^{-2}$	$.9031 \times 10^{-4}$	$-.1124 \times 10^{-2}$
33	$.8922 \times 10^{-2}$	$.1318 \times 10^{-4}$	$.8923 \times 10^{-2}$
35	$.1978 \times 10^{-2}$	$.1668 \times 10^{-3}$	$.1988 \times 10^{-2}$
37	$-.4042 \times 10^{-2}$	$.1667 \times 10^{-3}$	$-.4032 \times 10^{-2}$

TABLE IV.- CONTINUED.

(g) Wing element number 7.

n	$\left(\gamma_n{}^*\right)_u$	$\left(\gamma_n{}^*\right)_s$	$\gamma_n{}^*$
1	0.1504×10^{-1}	-0.7527	-0.2038×10^{-1}
3	$.5024 \times 10^{-1}$	$-.6086$	$.2159 \times 10^{-1}$
5	$.6197 \times 10^{-1}$	$-.4002$	$.4313 \times 10^{-1}$
7	$.2096 \times 10^{-1}$	$-.2494$	$.9227 \times 10^{-2}$
9	$-.3282 \times 10^{-1}$	$-.1487$	$-.3982 \times 10^{-1}$
11	$-.2544 \times 10^{-1}$	$-.8319 \times 10^{-1}$	$-.2936 \times 10^{-1}$
13	$-.3194 \times 10^{-2}$	$-.4245 \times 10^{-1}$	$-.5192 \times 10^{-2}$
15	$.3308 \times 10^{-1}$	$-.1877 \times 10^{-1}$	$.3220 \times 10^{-1}$
17	$.1888 \times 10^{-2}$	$-.6201 \times 10^{-2}$	$.1596 \times 10^{-2}$
19	$-.1562 \times 10^{-1}$	$-.3332 \times 10^{-3}$	$-.1564 \times 10^{-1}$
21	$-.4374 \times 10^{-2}$	$.1826 \times 10^{-2}$	$-.4288 \times 10^{-2}$
23	$.5223 \times 10^{-2}$	$.2167 \times 10^{-2}$	$.5325 \times 10^{-2}$
25	$.8419 \times 10^{-2}$	$.1776 \times 10^{-2}$	$.8503 \times 10^{-2}$
27	$-.1442 \times 10^{-1}$	$.1213 \times 10^{-2}$	$-.1436 \times 10^{-1}$
29	$.8713 \times 10^{-2}$	$.7236 \times 10^{-3}$	$.8747 \times 10^{-2}$
31	$.5125 \times 10^{-2}$	$.3795 \times 10^{-3}$	$.5143 \times 10^{-2}$
33	$-.6490 \times 10^{-2}$	$.1690 \times 10^{-3}$	$-.6482 \times 10^{-2}$
35	$-.3872 \times 10^{-2}$	$-.1372 \times 10^{-3}$	$-.3878 \times 10^{-2}$
37	$.3965 \times 10^{-2}$	$-.1861 \times 10^{-3}$	$.3956 \times 10^{-2}$

TABLE IV.- CONCLUDED.

(h) Wing element number 8.

n	$\left(\gamma_n{}^*\right)_u$	$\left(\gamma_n{}^*\right)_S$	$\gamma_n{}^*$
1	0.7368×10^{-2}	-0.7512	-0.2067×10^{-1}
3	$.4651\times10^{-1}$	$-.6314$	$.2294\times10^{-1}$
5	$.5005\times10^{-1}$	$-.4325$	$.3390\times10^{-1}$
7	$.1983\times10^{-1}$	$-.2804$	$.9367\times10^{-2}$
9	$-.8729\times10^{-2}$	$-.1755$	$-.1528\times10^{-1}$
11	$-.3937\times10^{-1}$	$-.1046$	$-.4328\times10^{-1}$
13	$-.6698\times10^{-2}$	$-.5815\times10^{-1}$	$-.8869\times10^{-2}$
15	$.1373\times10^{-1}$	$-.2925\times10^{-1}$	$.1264\times10^{-1}$
17	$.3284\times10^{-1}$	$-.1247\times10^{-1}$	$.3237\times10^{-1}$
19	$-.9760\times10^{-2}$	$-.3561\times10^{-2}$	$-.9892\times10^{-2}$
21	$-.2146\times10^{-1}$	$.5685\times10^{-3}$	$-.2144\times10^{-1}$
23	$-.5058\times10^{-2}$	$.2032\times10^{-2}$	$-.4982\times10^{-2}$
25	$.7683\times10^{-2}$	$.2172\times10^{-2}$	$.7764\times10^{-2}$
27	$.1418\times10^{-1}$	$.1772\times10^{-2}$	$.1425\times10^{-1}$
29	$-.4515\times10^{-2}$	$.1246\times10^{-2}$	$-.4469\times10^{-2}$
31	$.1036\times10^{-2}$	$.7753\times10^{-3}$	$.1065\times10^{-2}$
33	$-.1018\times10^{-1}$	$.4086\times10^{-3}$	$-.1016\times10^{-1}$
35	$.1435\times10^{-2}$	$-.5035\times10^{-4}$	$.1433\times10^{-2}$
37	$.3316\times10^{-2}$	$-.1795\times10^{-3}$	$.3310\times10^{-2}$

TABLE V.- CALCULATED SPAN LOAD DISTRIBUTION FOR
A DELTA WING OF ASPECT RATIO 2.0 AT 20° ANGLE
OF ATTACK (8 wings, 19 harmonics, $\theta/\alpha = 0.5$).

y/s_o	$c_l c/c_o$	y/s_o	$c_l c/c_o$
0.0000	0.2072	0.4625	0.1122
.0125	.2073	.4875	.1159
.0250	.2074	.5125	.1190
.0375	.2075	.5375	.1224
.0500	.2077	.5625	.0854
.0625	.1864	.5875	.0898
.0875	.1868	.6125	.0934
.1125	.1874	.6375	.0972
.1375	.1880	.6625	.0993
.1625	.1893	.6875	.0608
.1875	.1578	.7125	.0650
.2125	.1594	.7375	.0673
.2375	.1624	.7625	.0711
.2625	.1653	.7875	.0763
.2875	.1675	.8125	.0421
.3125	.1330	.8375	.0448
.3375	.1366	.8625	.0439
.3625	.1406	.8875	.0420
.3875	.1431	.9125	.0383
.4125	.1454	.9375	.0000
.4375	.1080		
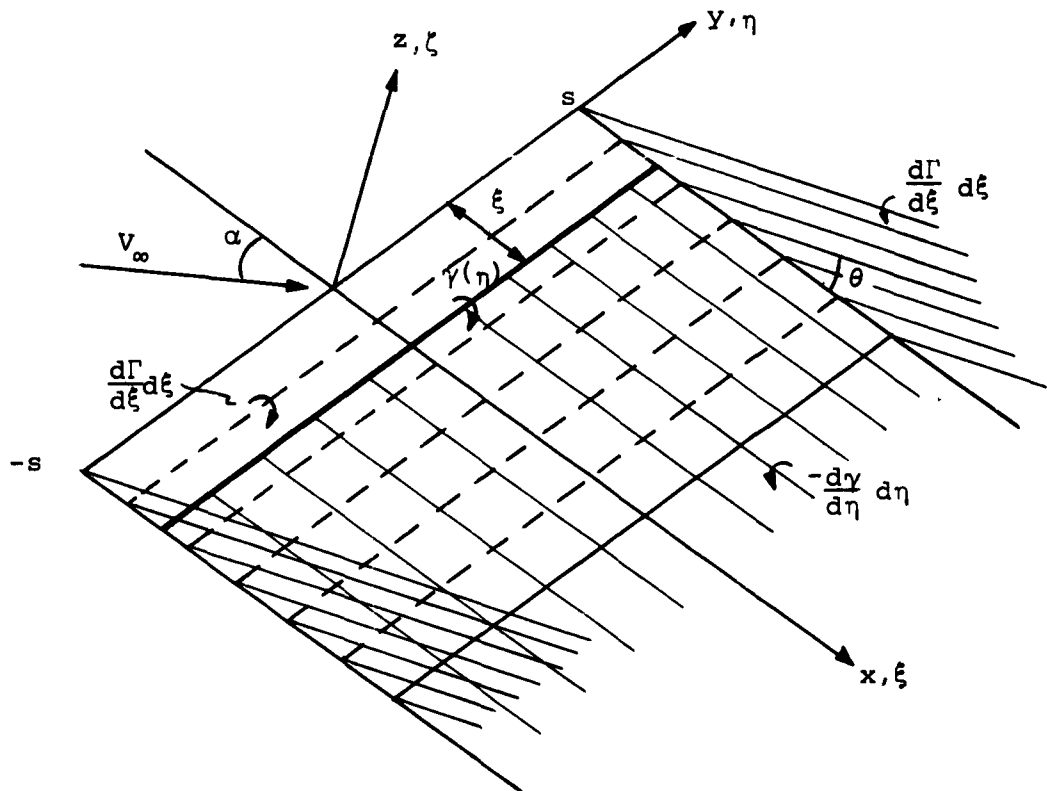
Figure 1.- Assumed mathematical model of a rectangular wing
element with side-edge flow separation.
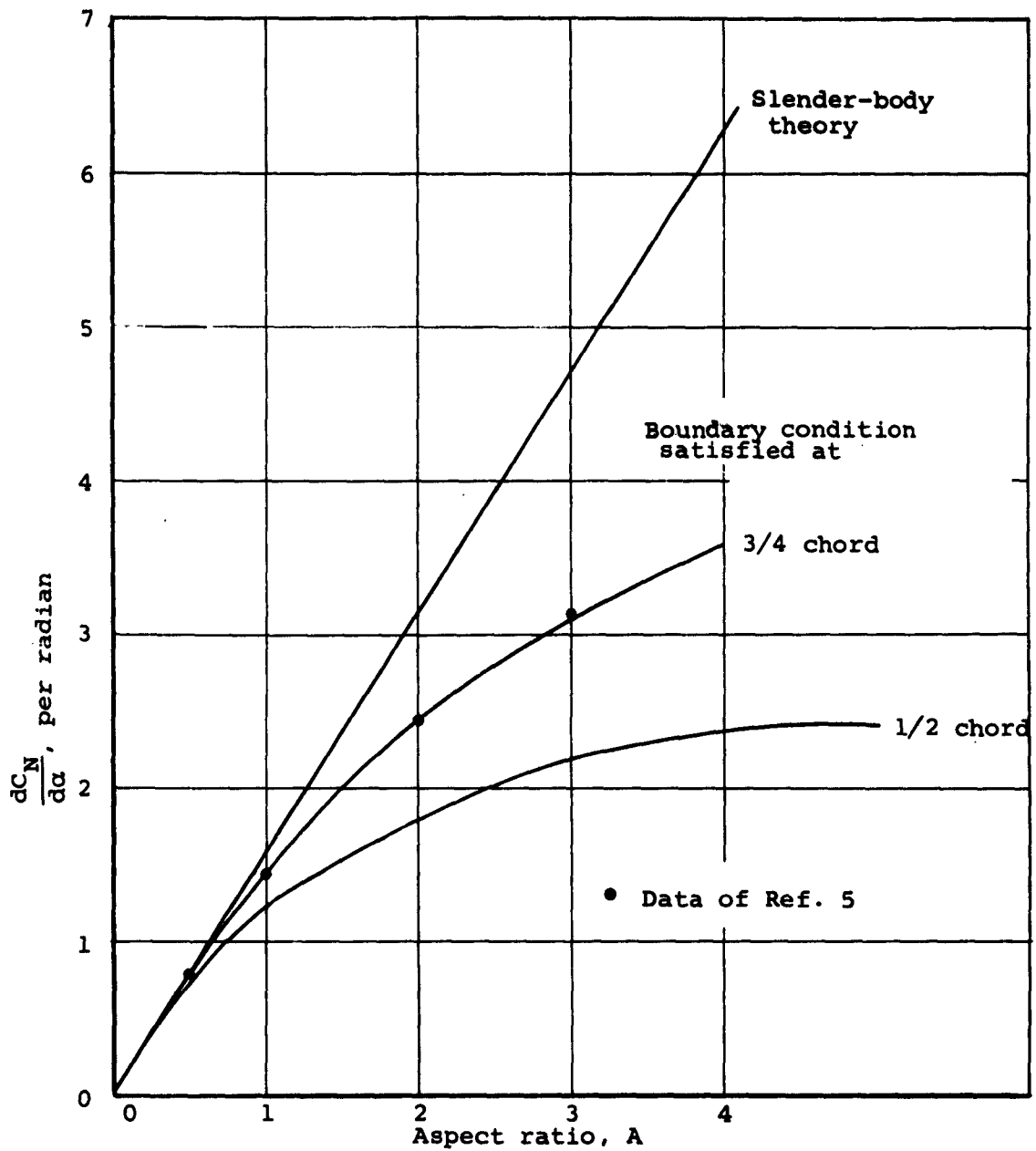
Figure 2.- Dependence of lift-curve slope on location of control
line for rectangular wings, from Equation (64).
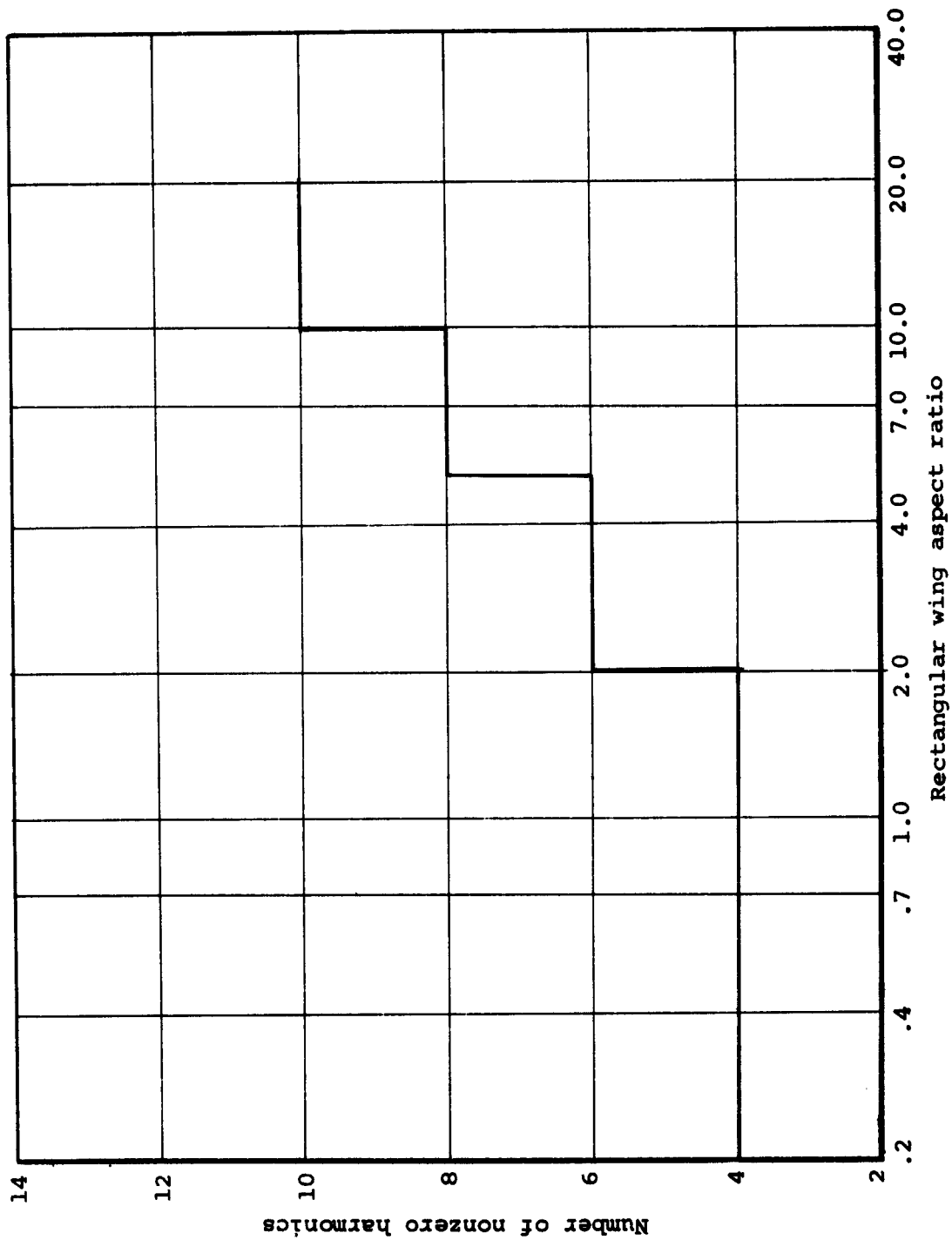
Figure 3.- Number of nonzero harmonics required for 1-percent precision in normal force coefficient (rectangular wings).
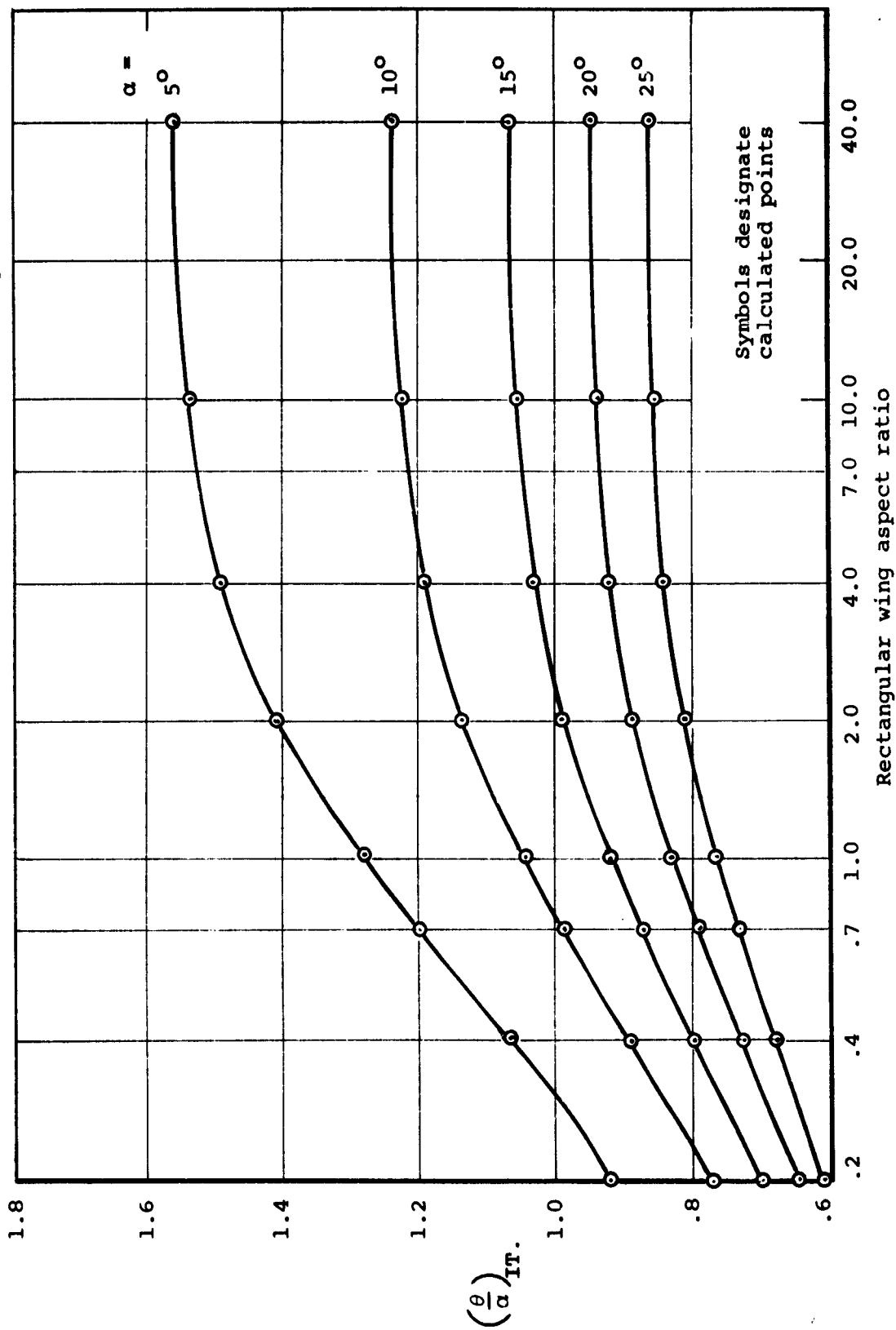
Figure 4.- Iterated value of shedding angle for rectangular wings with control line at 3/4 chord.
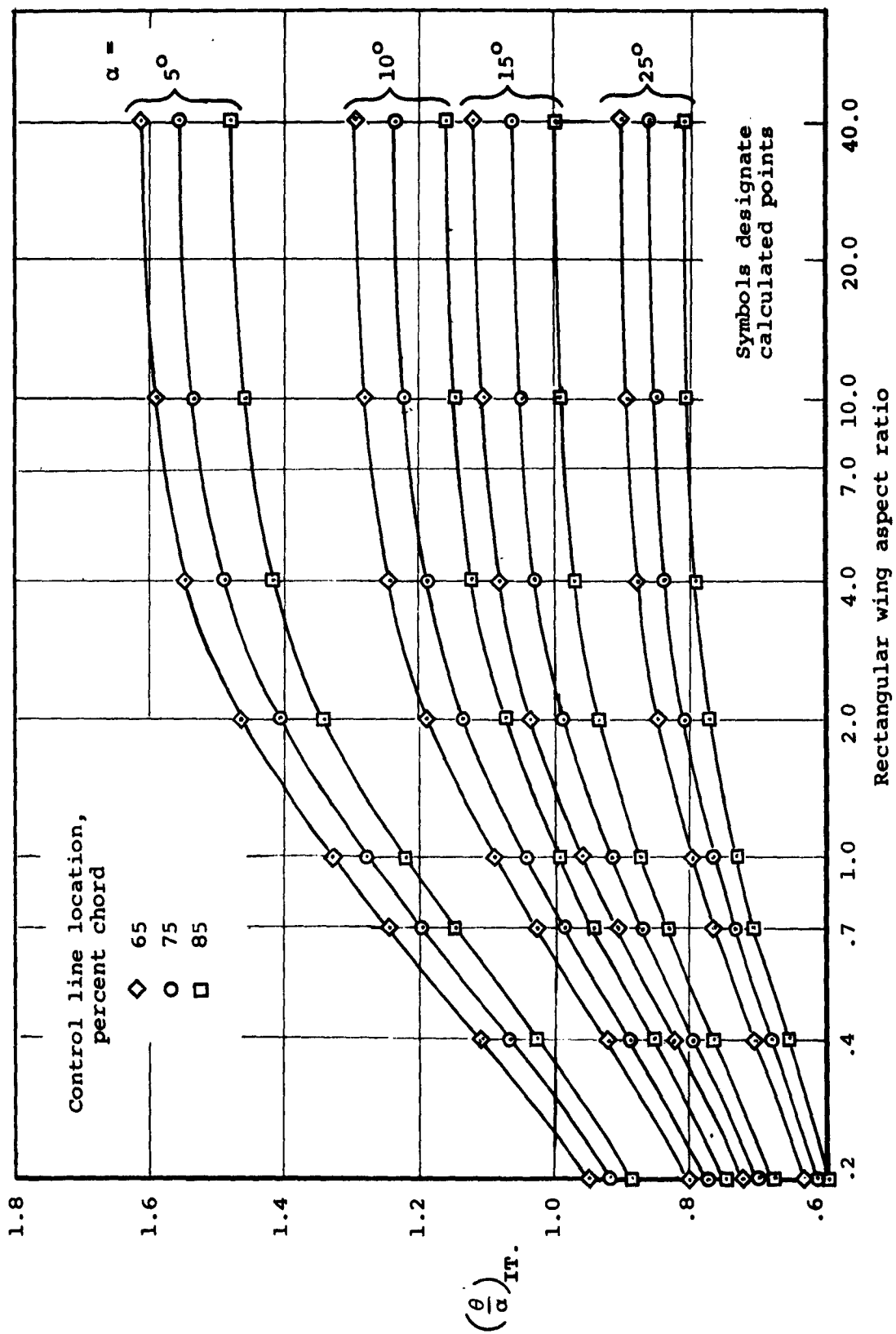
Figure 5.- Effect of control line location on iterated value of shedding angle.
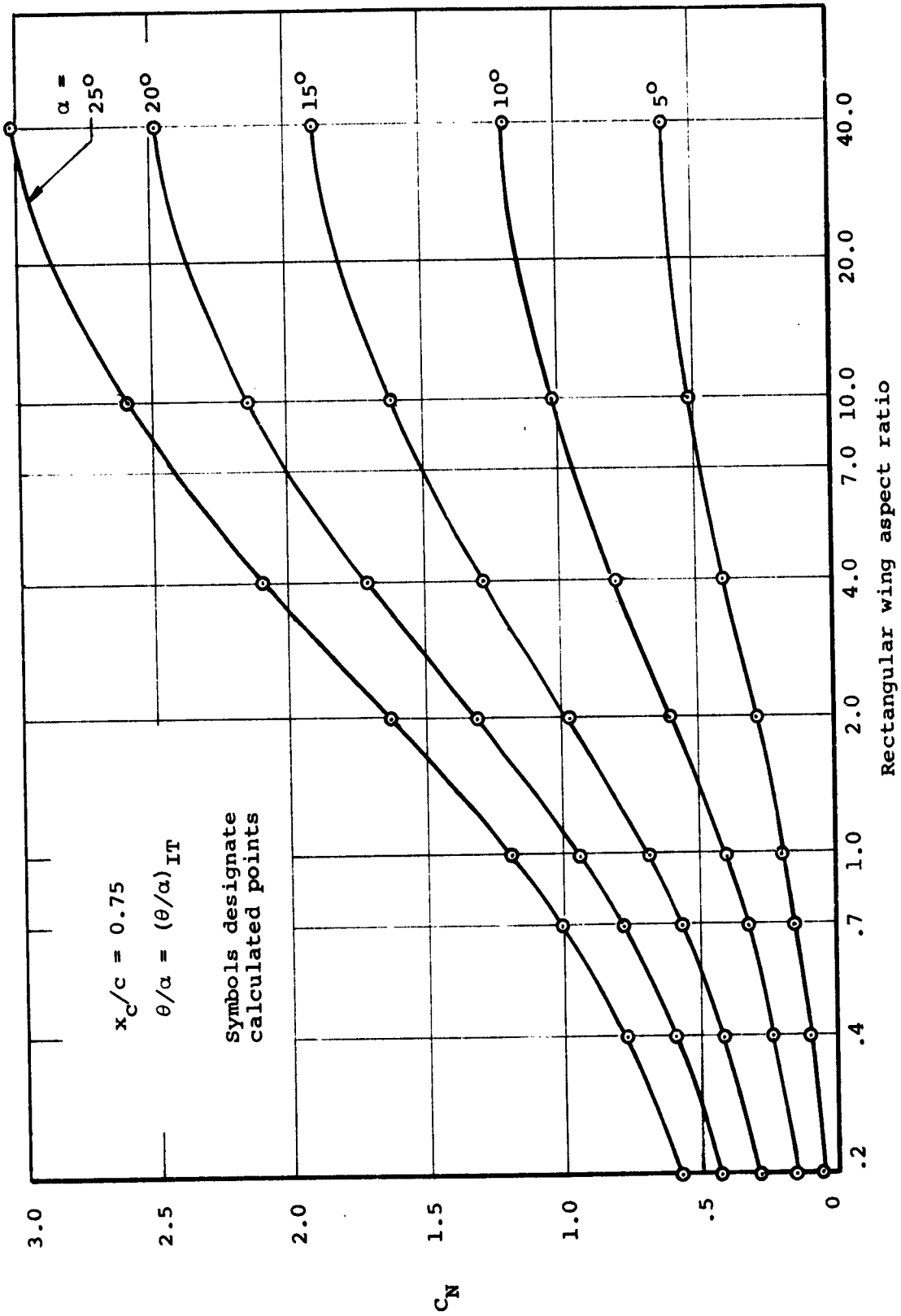
(a) Normal force coefficient.

Figure 6.- Variation of the aerodynamic characteristics of a rectangular wing with aspect ratio and angle of attack.
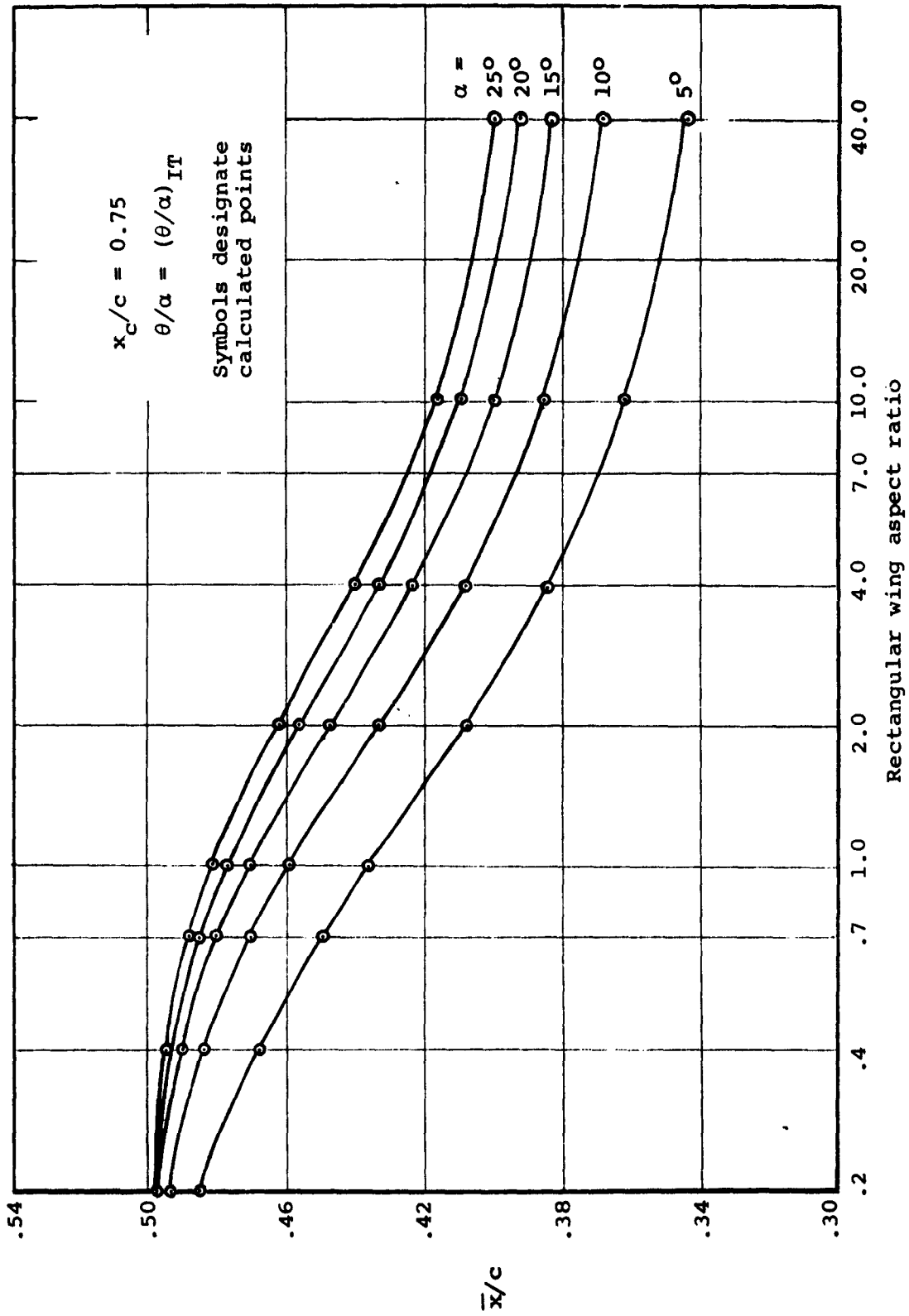
(b) Center of pressure.

Figure 6.- Concluded.
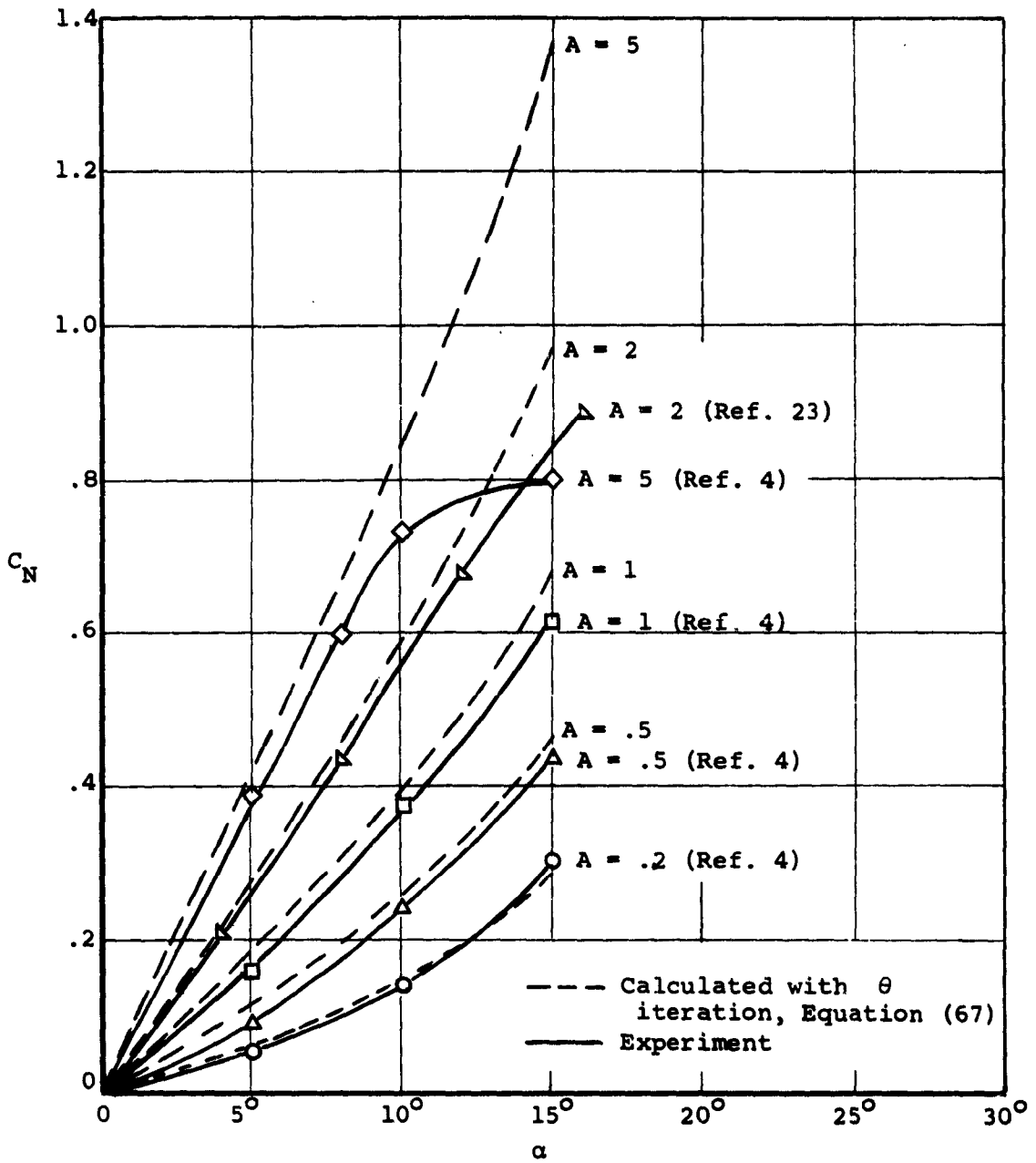
(a) Normal force.

Figure 7.- Aerodynamics of rectangular wings
of various aspect ratios.
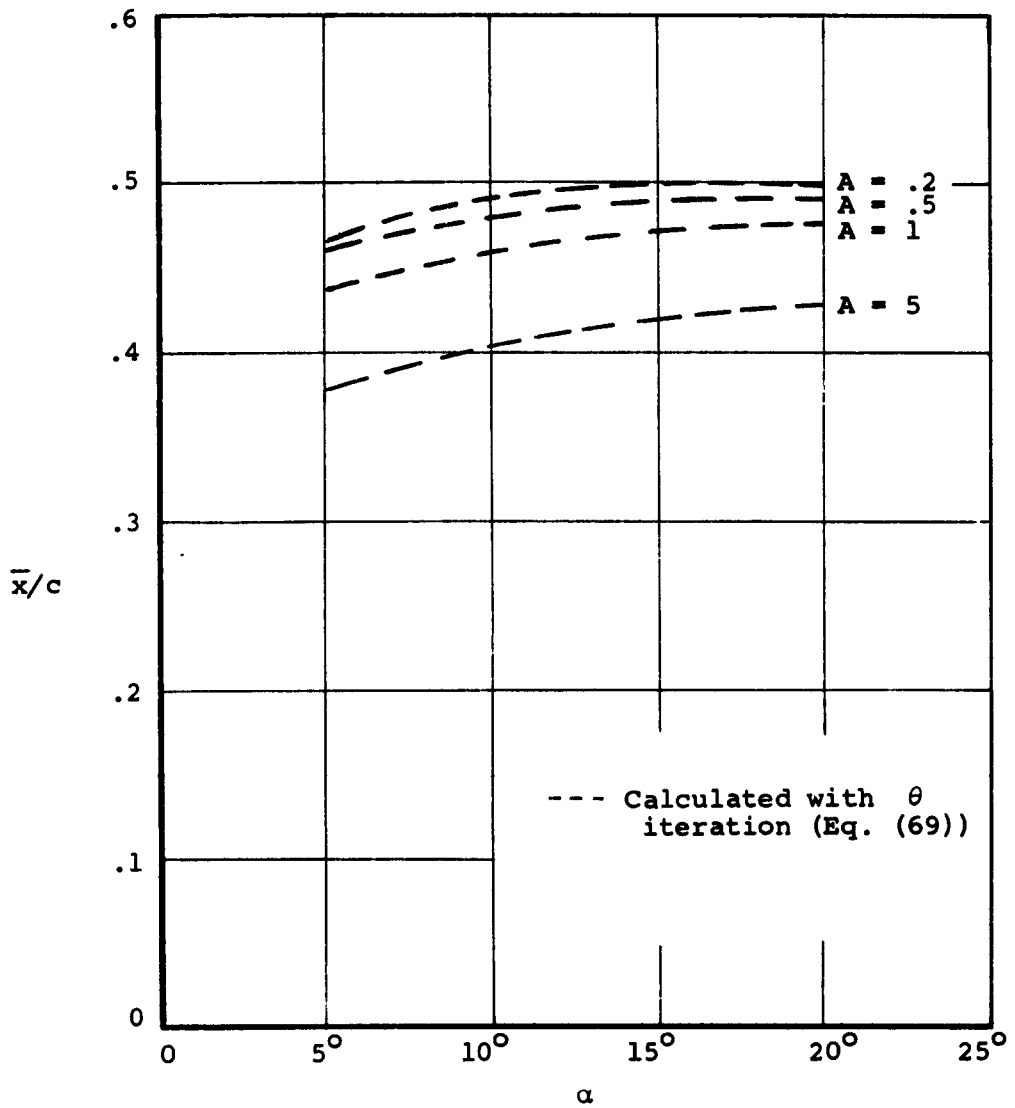
(b)   Center of pressure.

Figure 7.- Concluded.
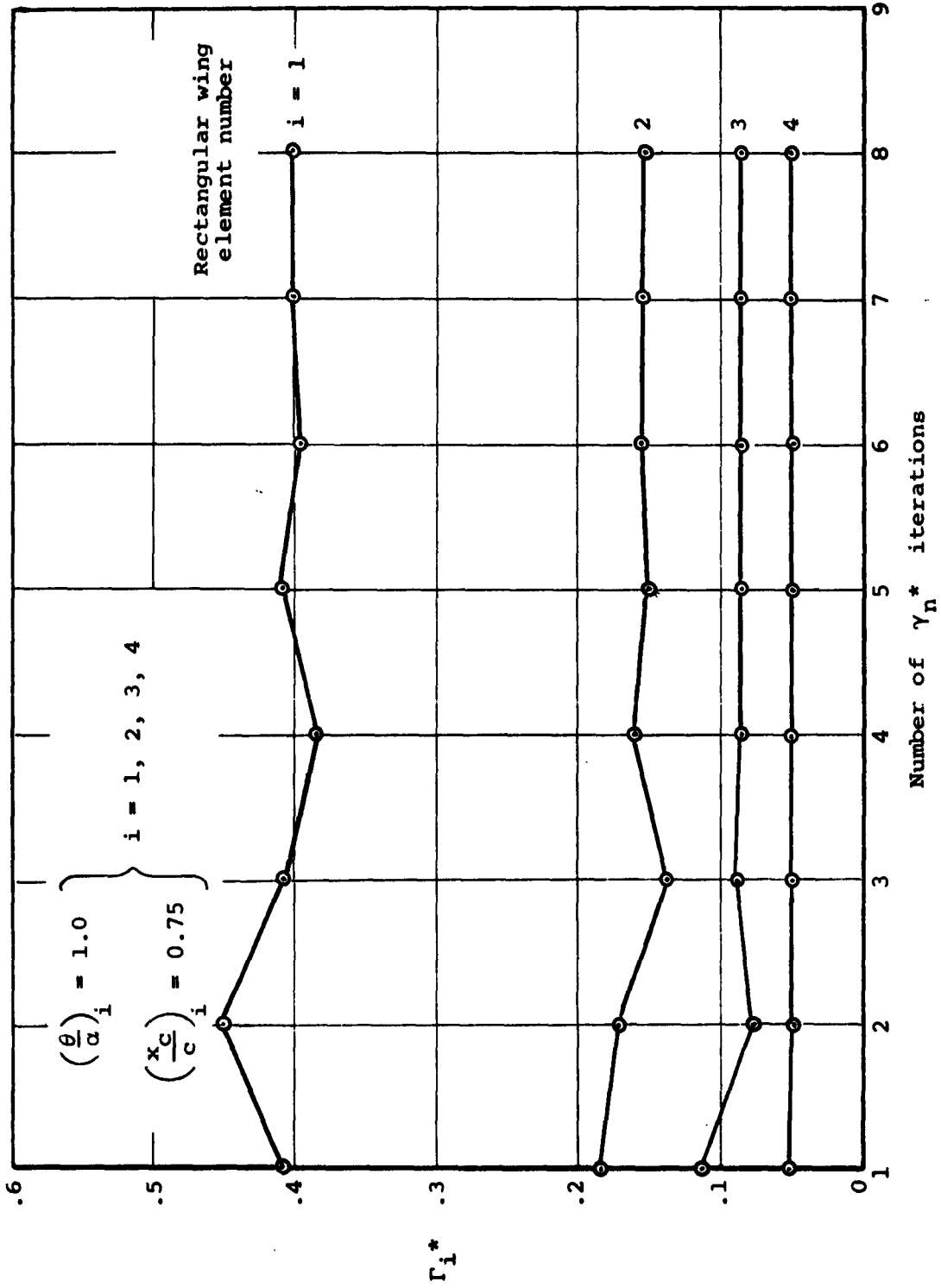
(a) Strength of the shed vorticity on the rectangular elements.

Figure 8.- Demonstration of convergence of various parameters with iteration on the loading coefficients (A = 4 delta wing, 20° angle of attack, 14 nonzero
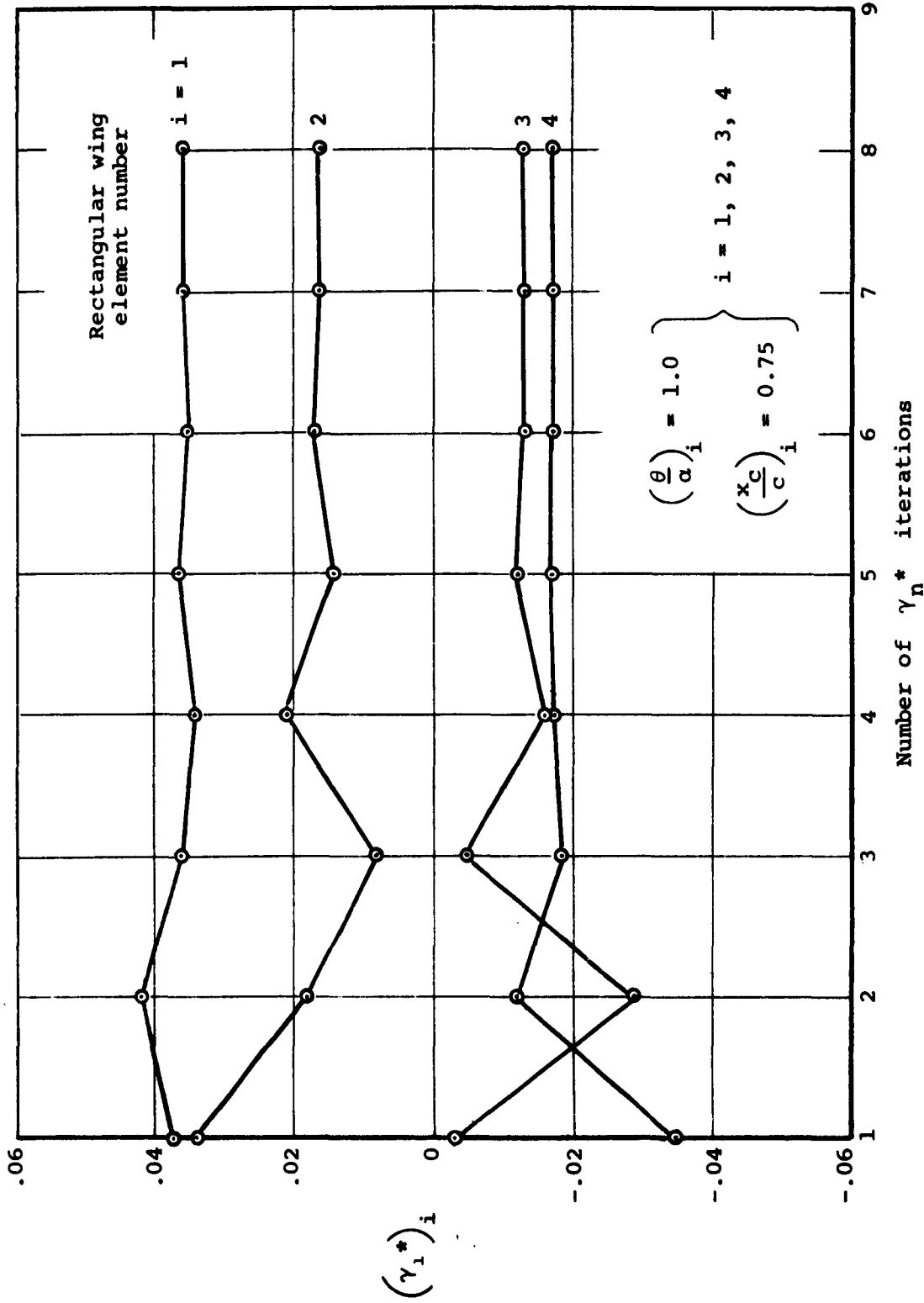
(b) First loading coefficient.

Figure 8.- Continued.
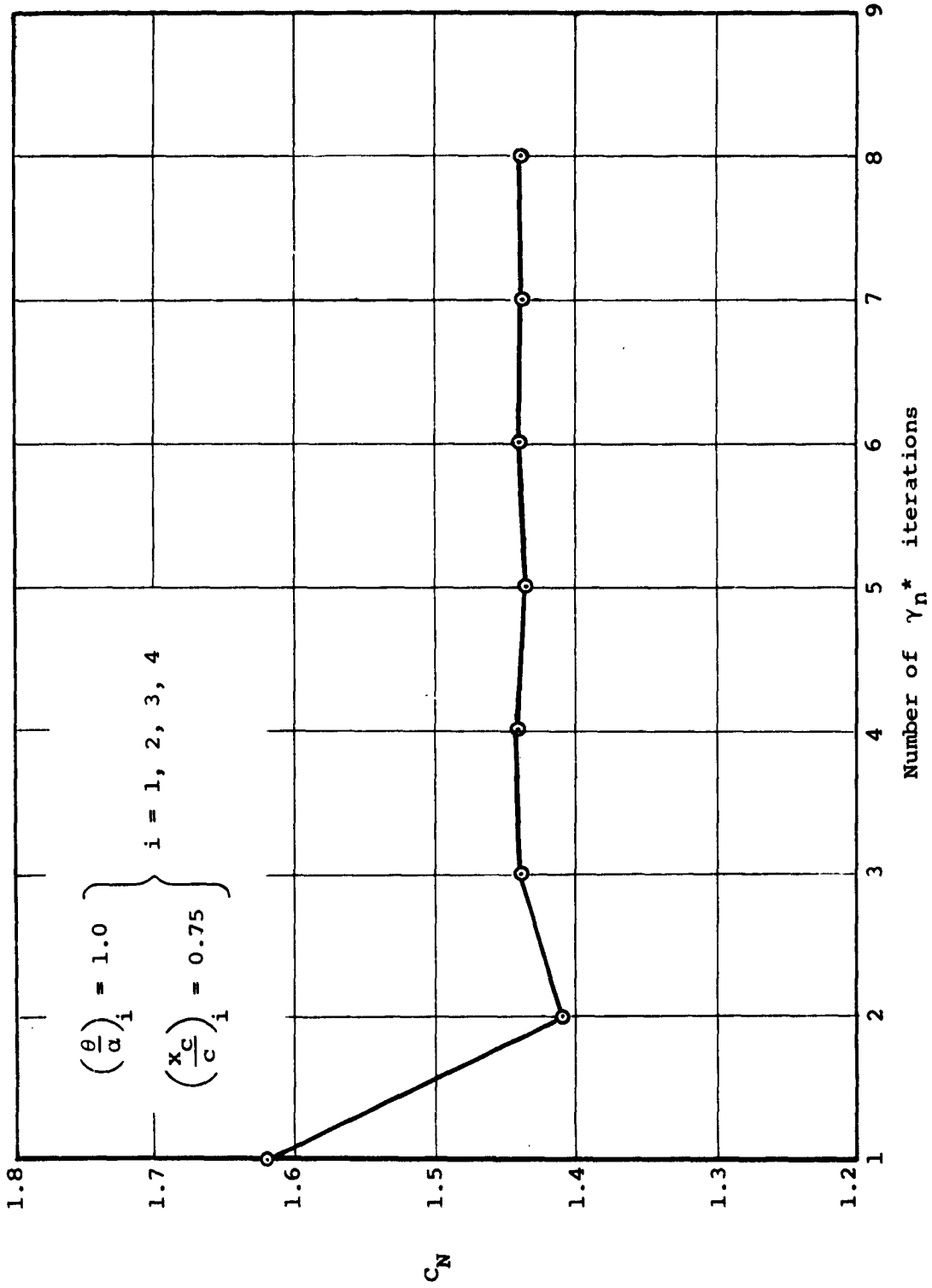
(c) Delta wing normal force coefficient.

Figure 8.- Concluded.
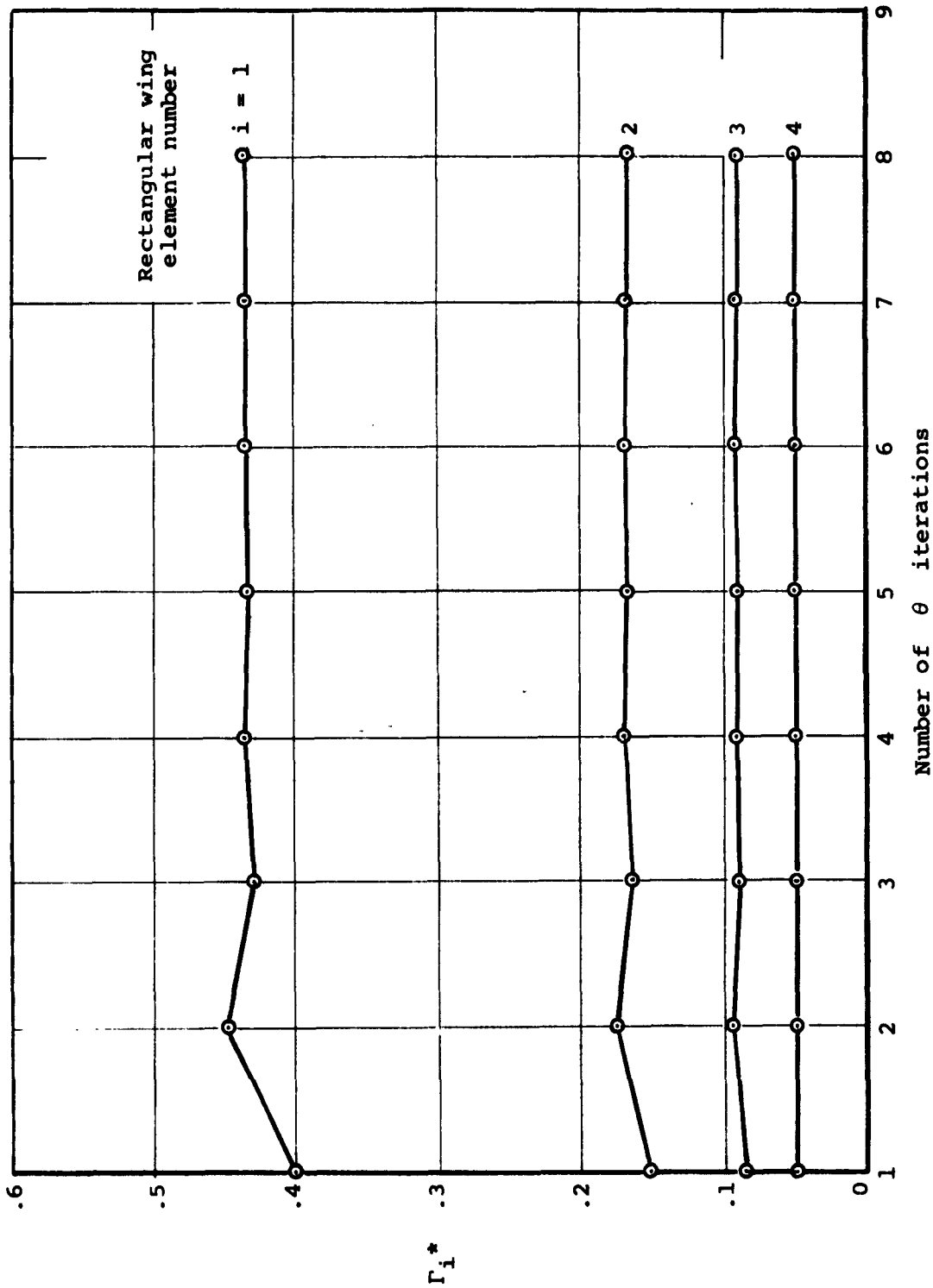
(a) Strength of the shed vorticity on the rectangular elements.

Figure ..- Demonstration of convergence of various parameters with iteration on the shedding angles (A = 4 delta wing, 20° angle of attack, 14 nonzero harmonics, 4 rectangular elements).
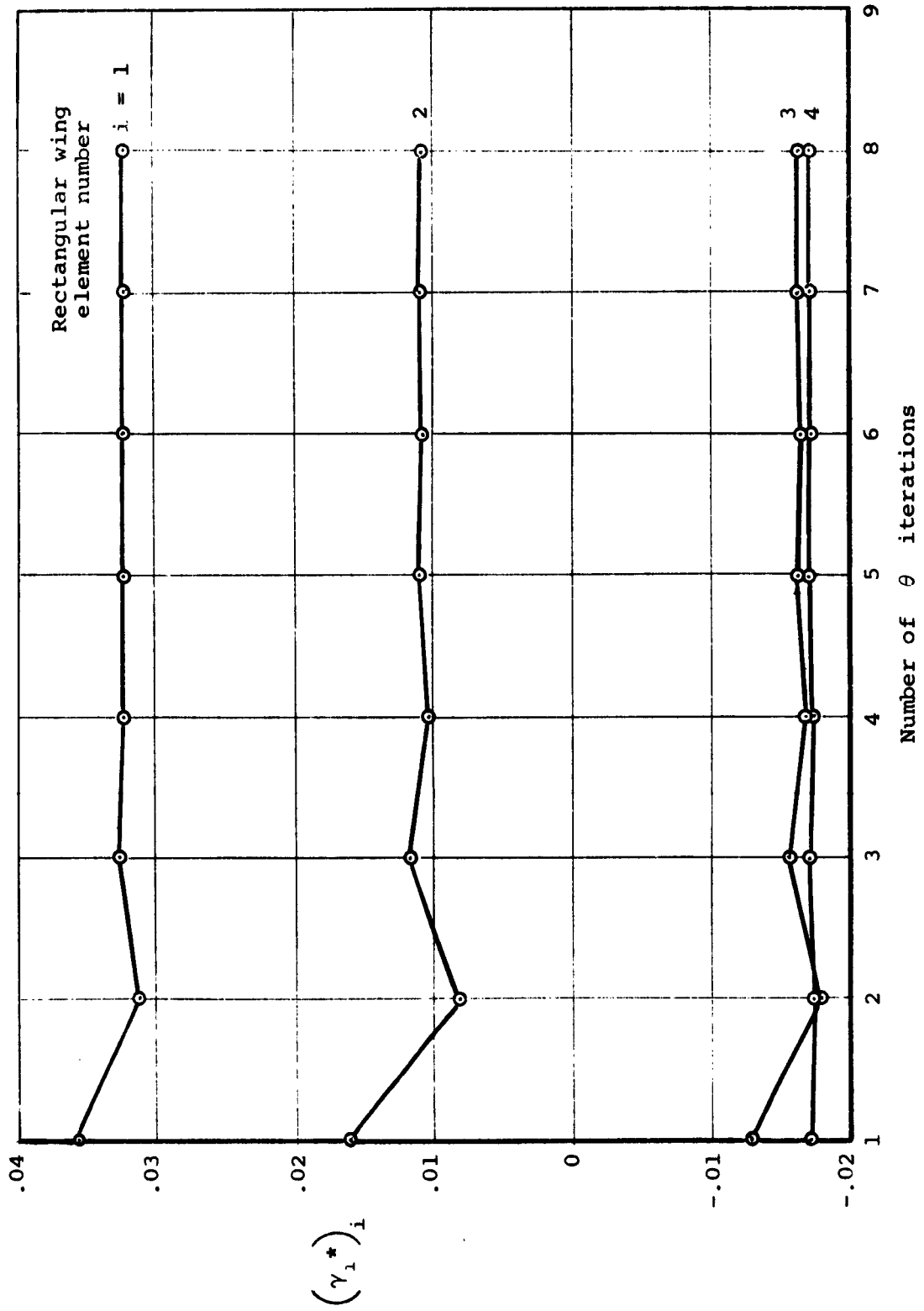
(b) First loading coefficient.

Figure 9.- Continued.
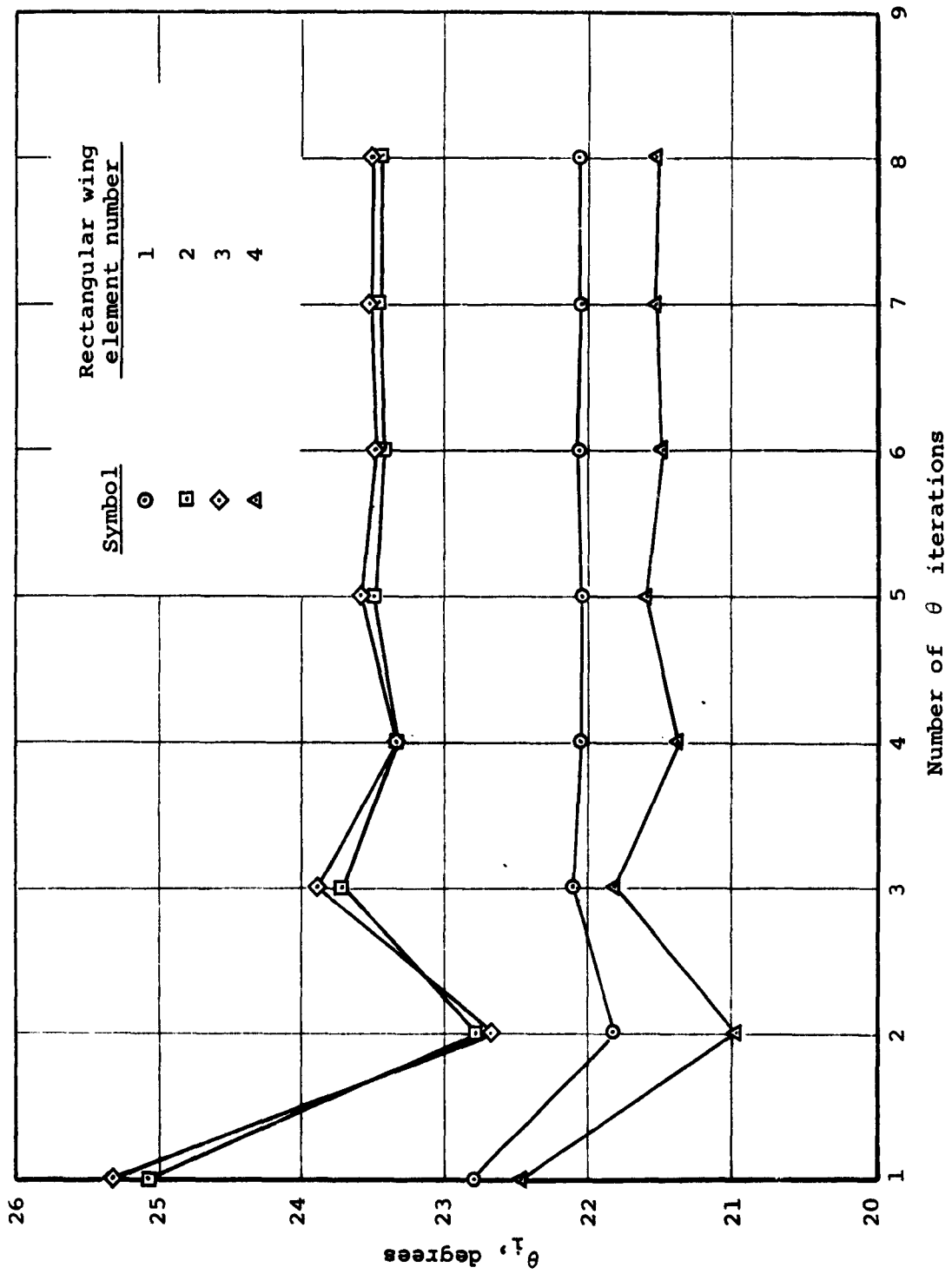
(c) Shedding angle.

Figure 9.- Continued.
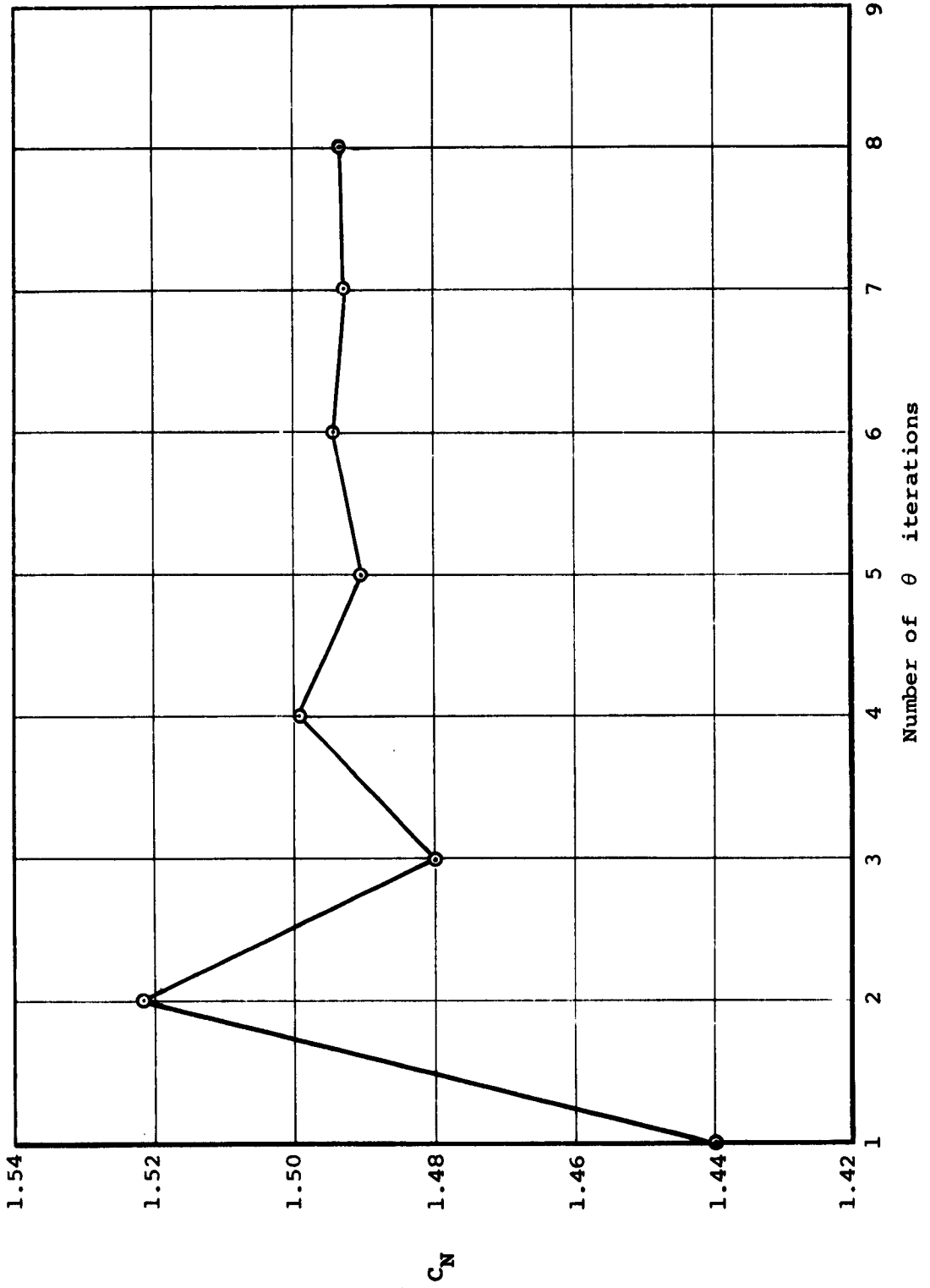
(d) Delta wing normal force coefficient.

Figure 9.- Concluded.
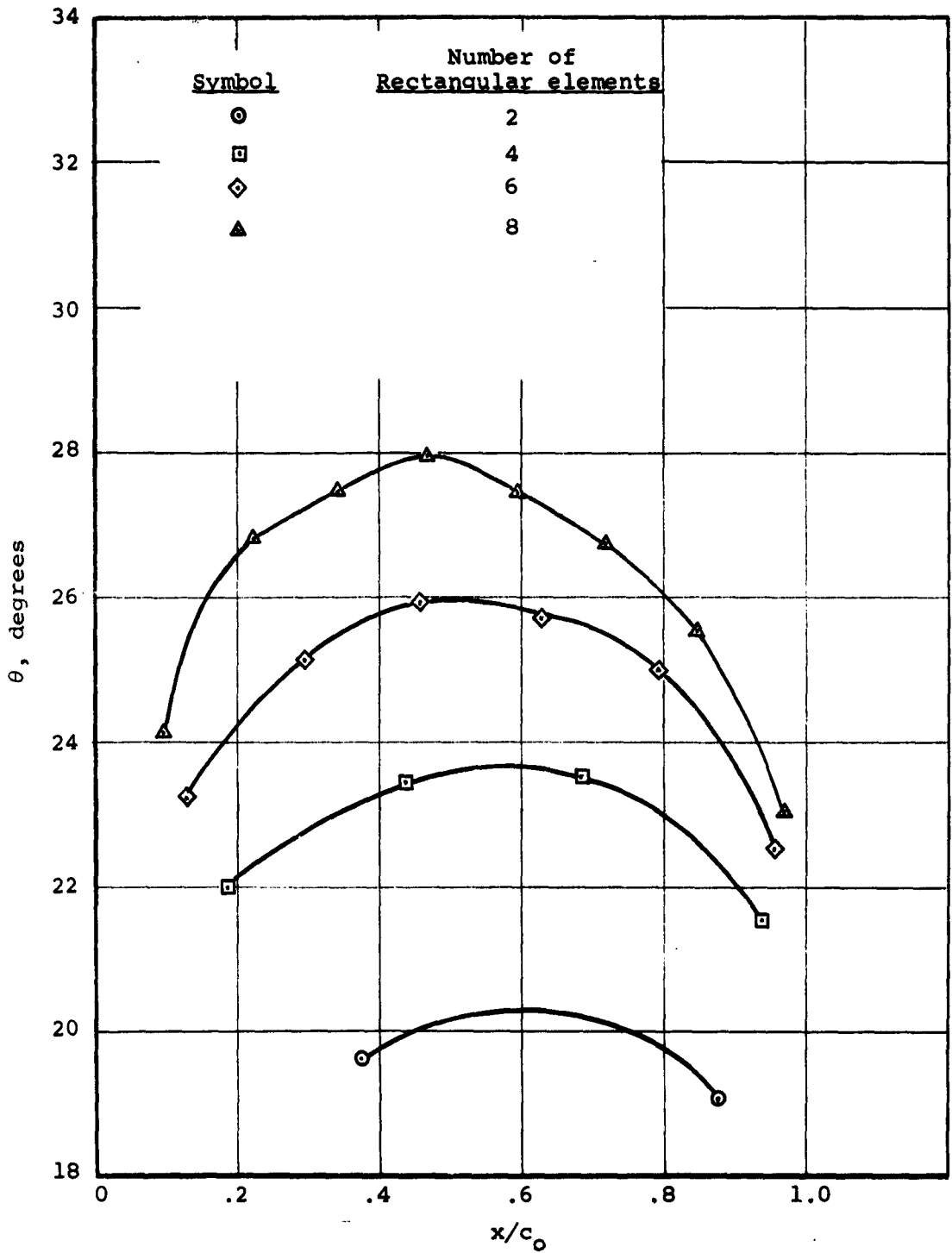
Figure 10.- Chordwise variation of shedding angle on aspect ratio 4 delta wing at 20° angle of attack.
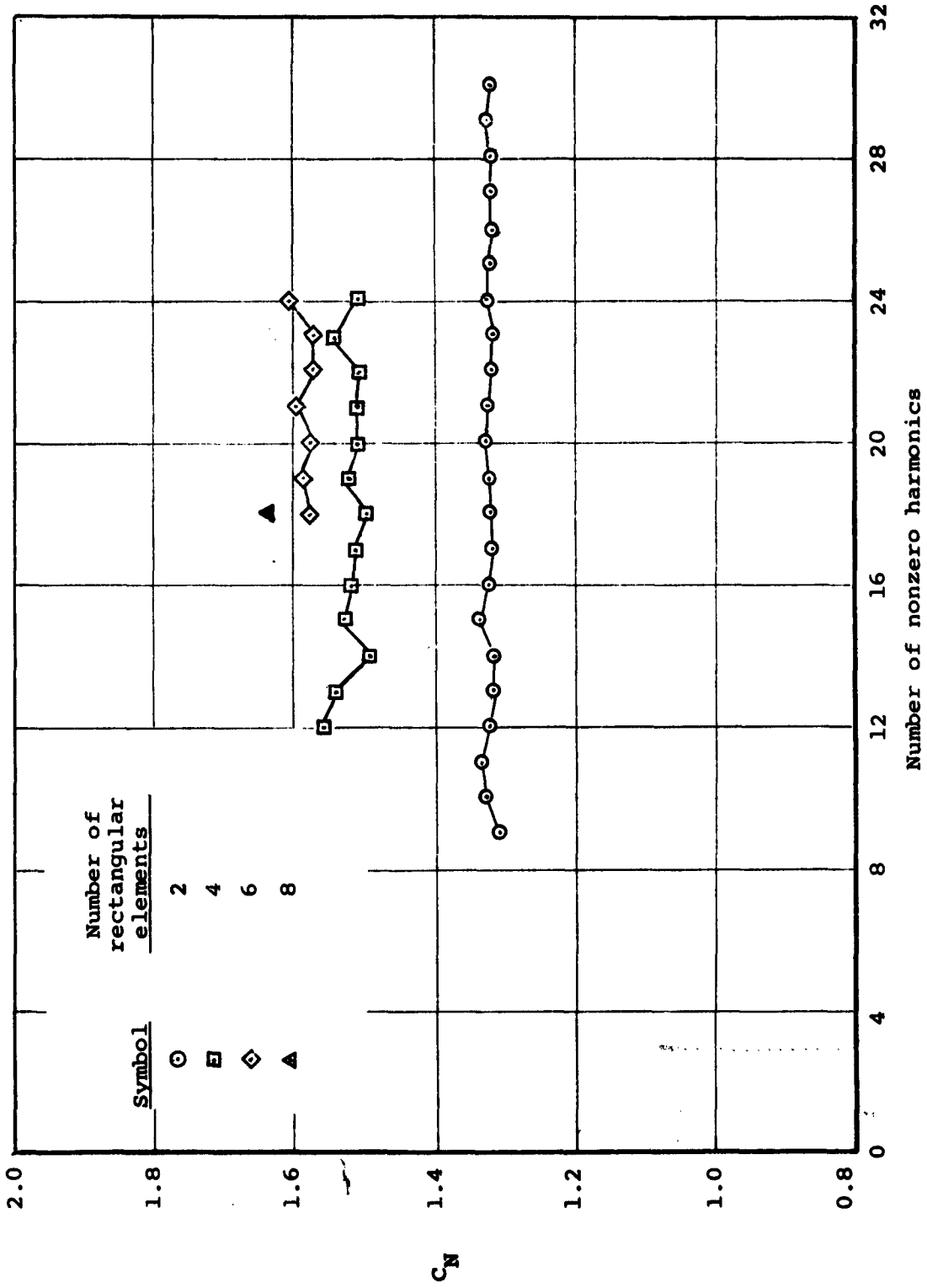
(a) Delta wing normal force coefficient.

Figure 11.- Convergence of aerodynamic characteristics with numbers of rectangular elements and nonzero harmonics.

Number of nonzero harmonics

$\overline{x}/c_o$

Symbol	Number of rectangular elements
⊙	2
⊡	4
◇	6
▲	8
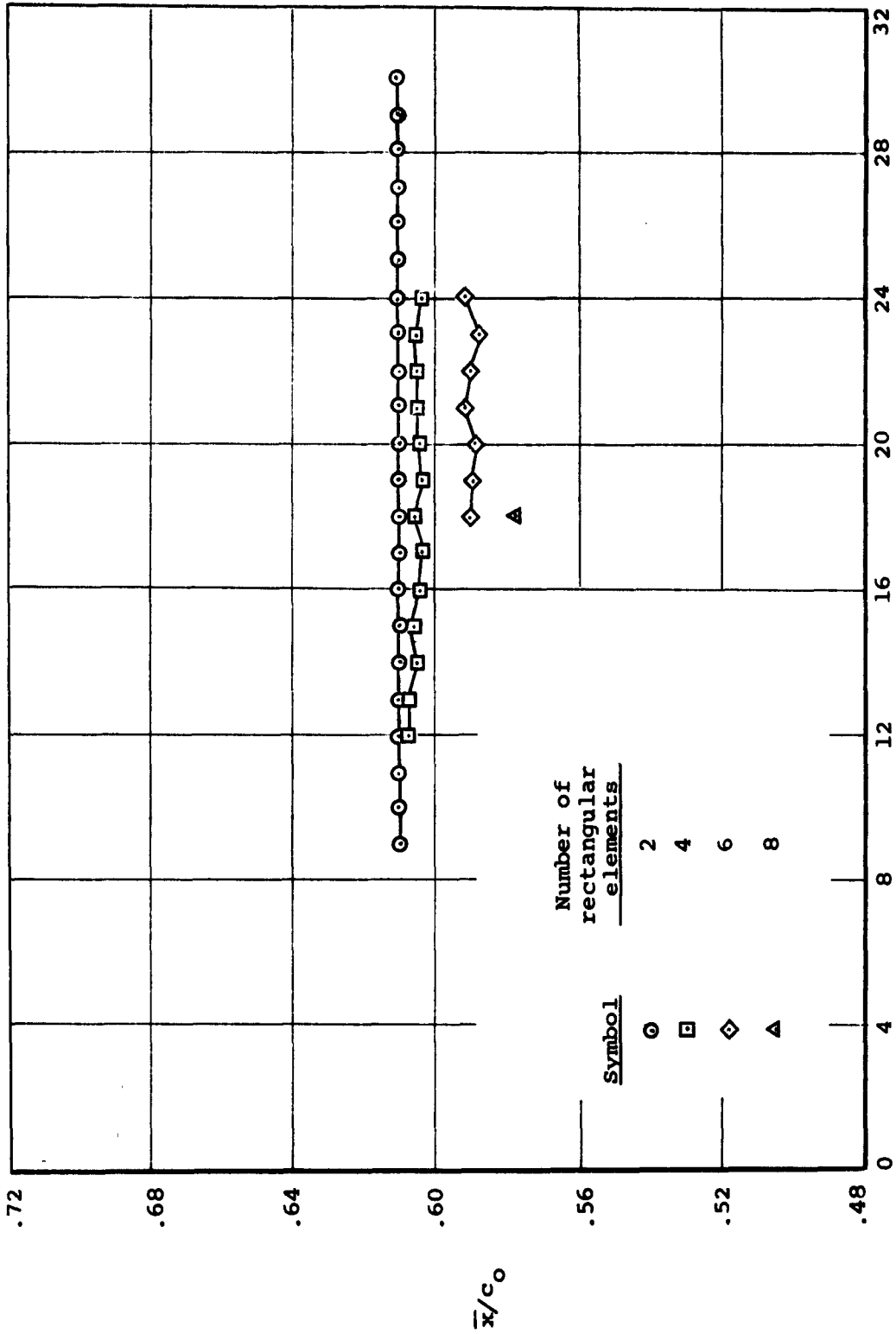
(b) Delta wing center of pressure.

Figure 11.- Concluded.
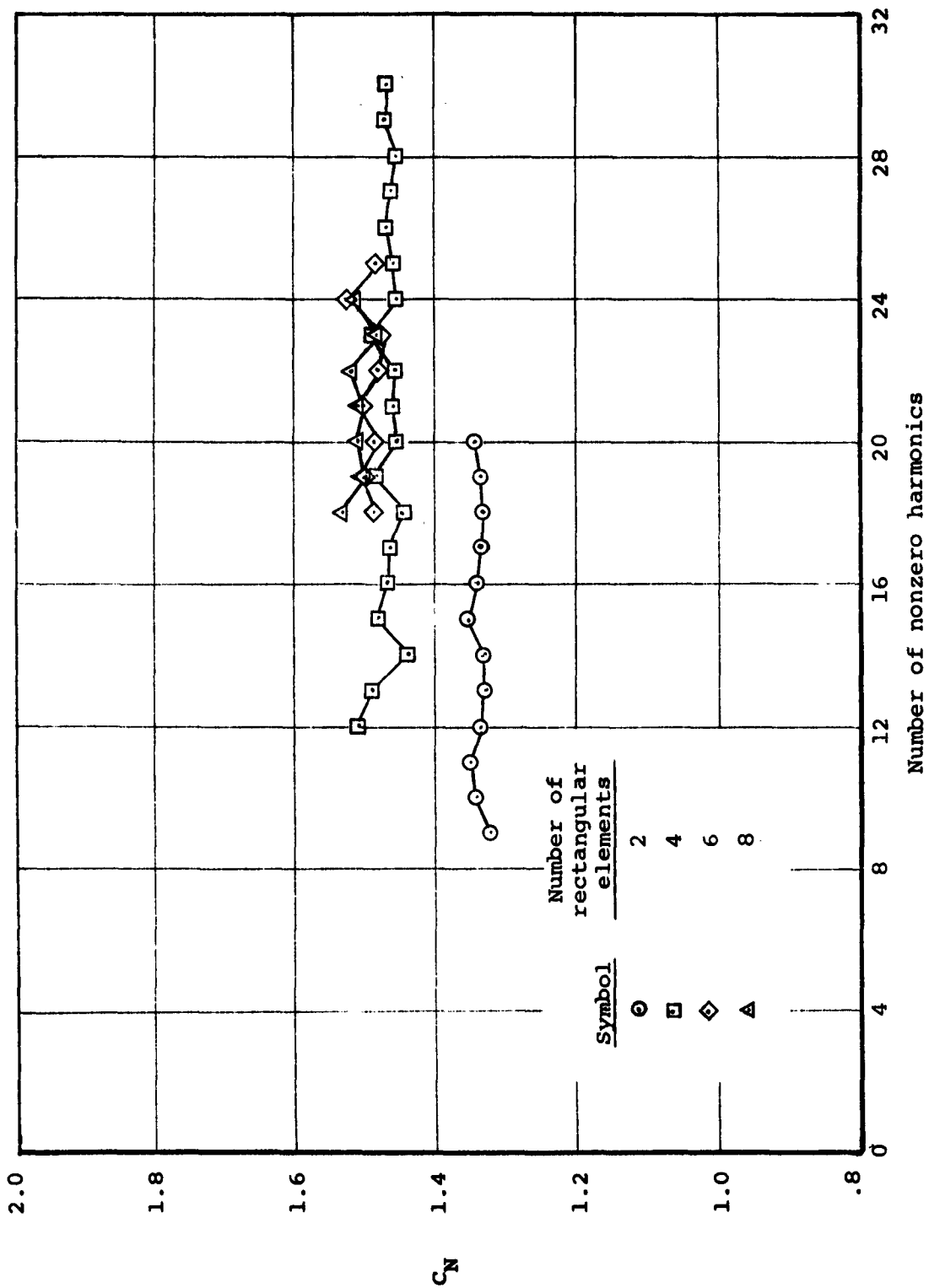
Figure 12.- Convergence without θ iteration $\left(\dfrac{\theta}{\alpha} = 1.0\right)$.

(a) Normal force coefficient.
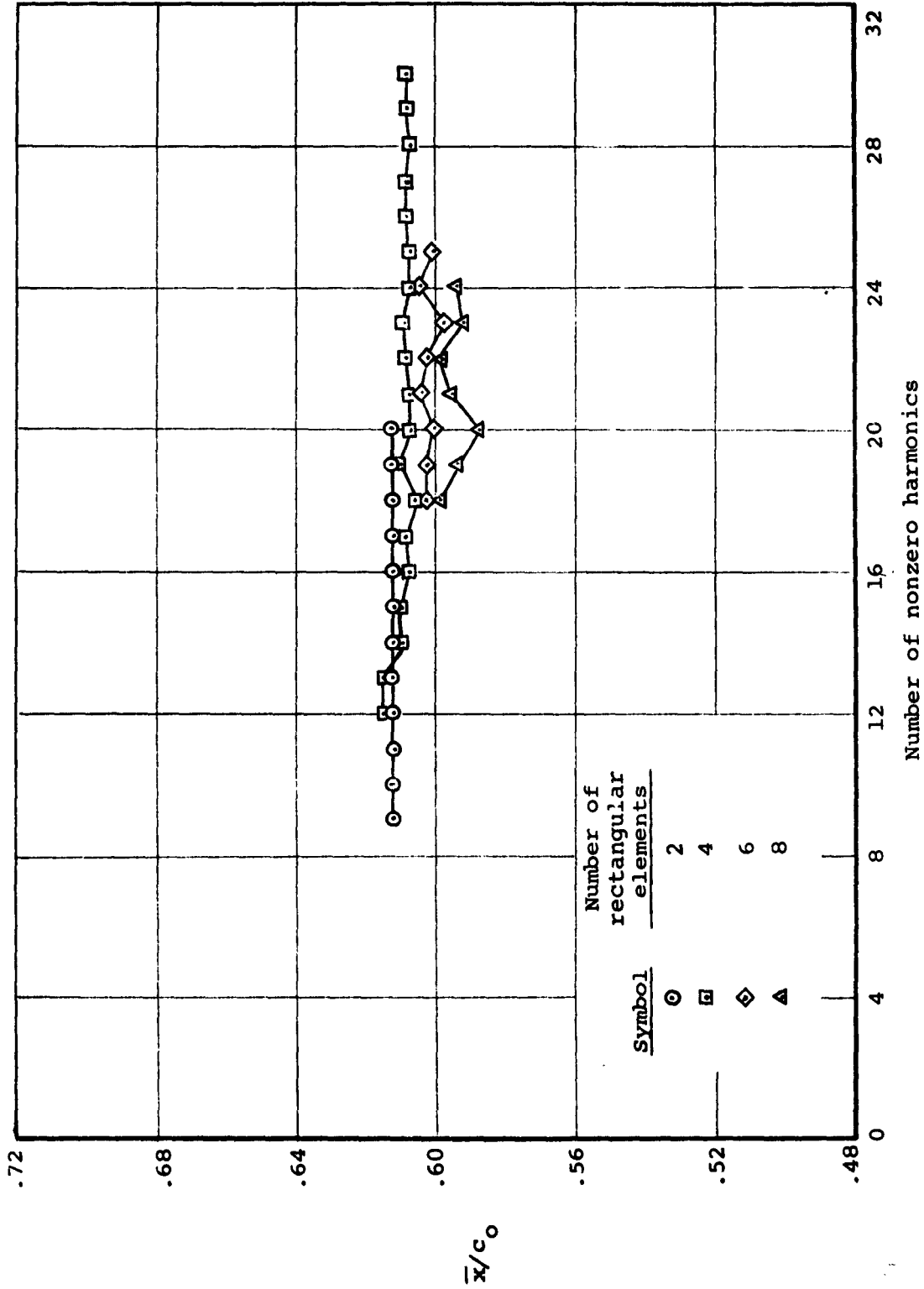
(b) Center of pressure.

Figure 12.- Concluded.
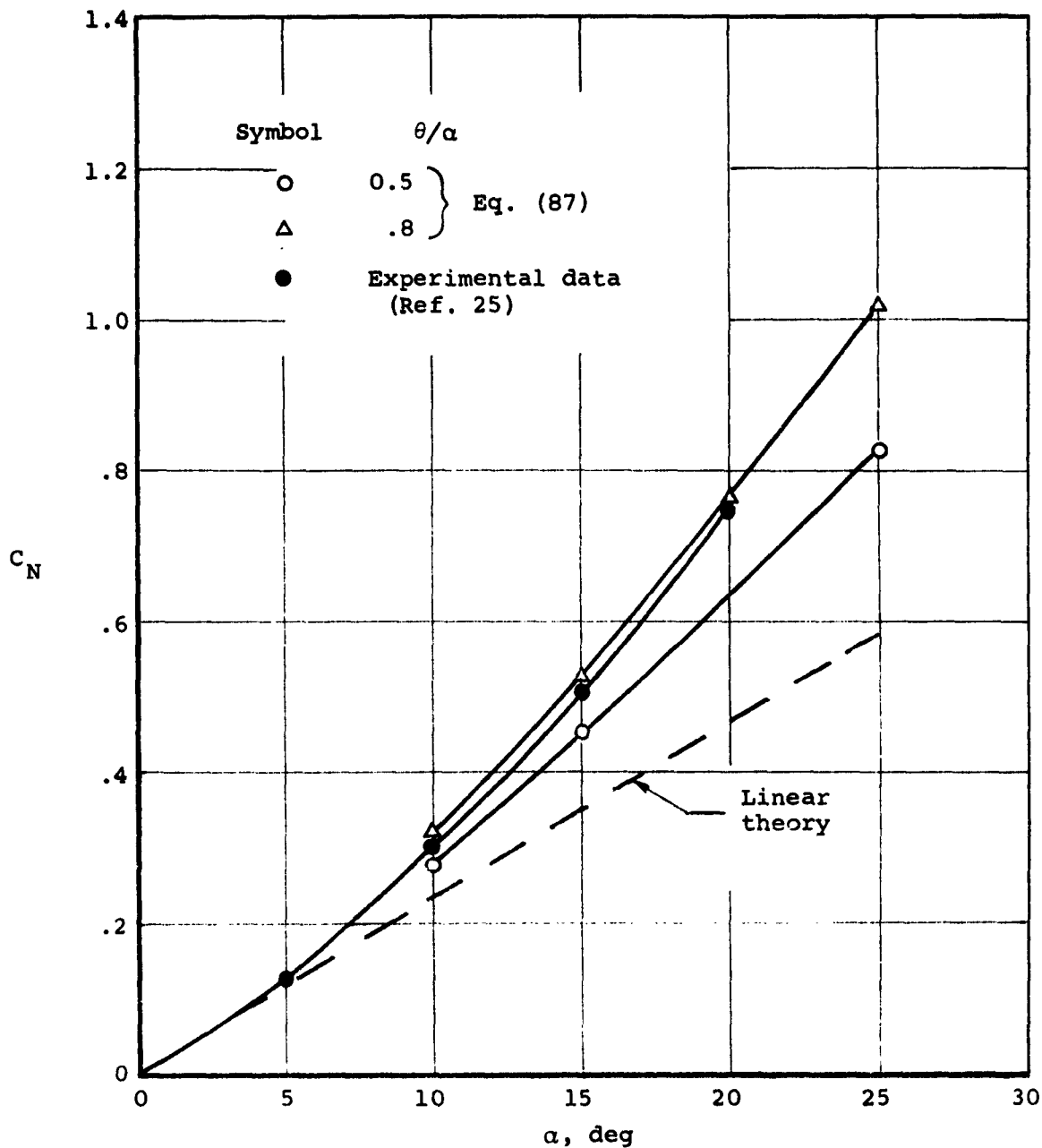
(a)   Normal force.

Figure 13.- Aerodynamics of a delta wing of aspect ratio 1 for various shedding angles (8 wings, 19 harmonics).
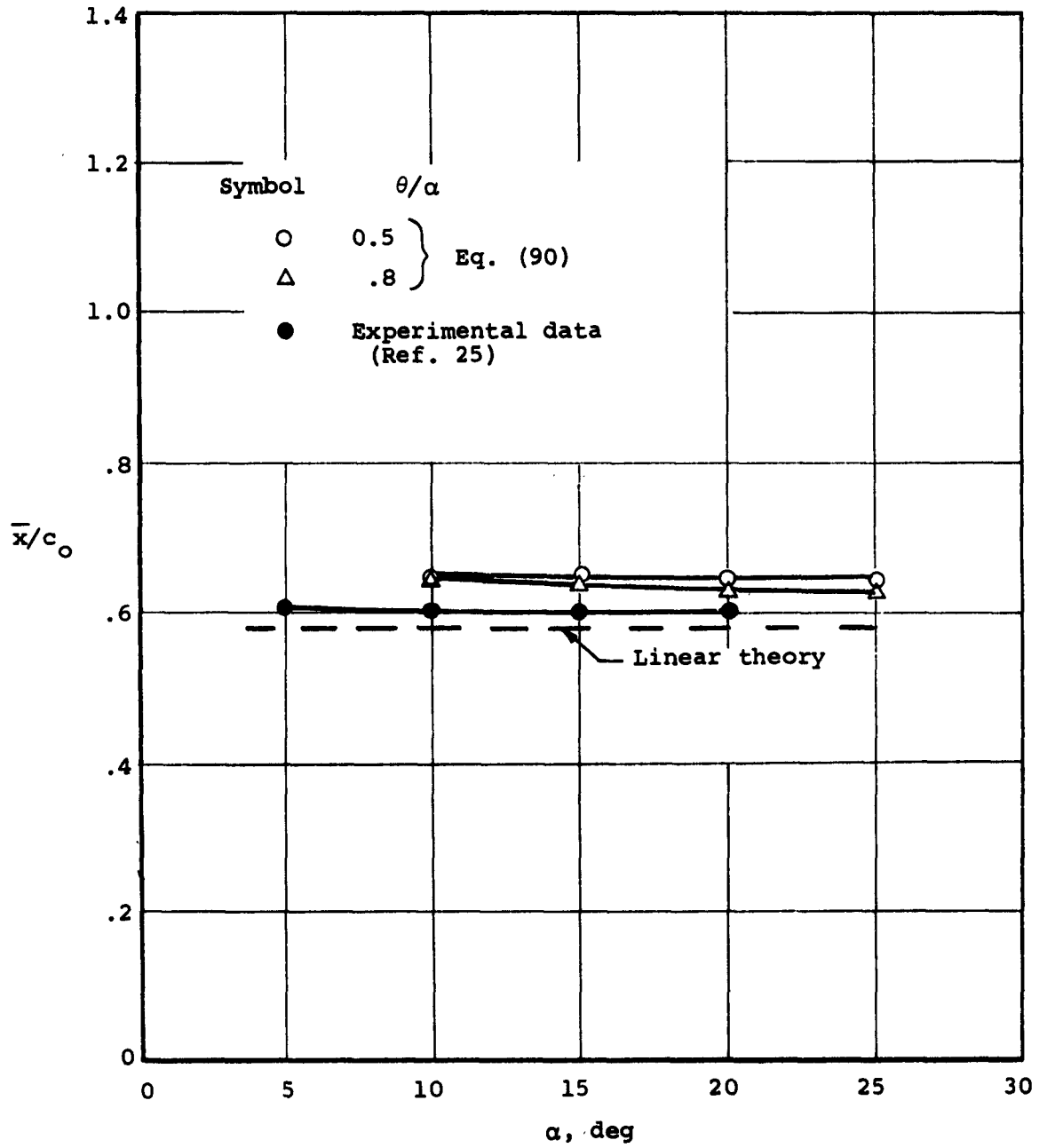
(b) Center of pressure.

Figure 13.- Concluded.

Symbol θ/α

○   0.3 } Eq. (87)
△   .5

●   Experimental data
          (cross plotted from
          Refs. 25, 29, and
   30)

Linear
theory
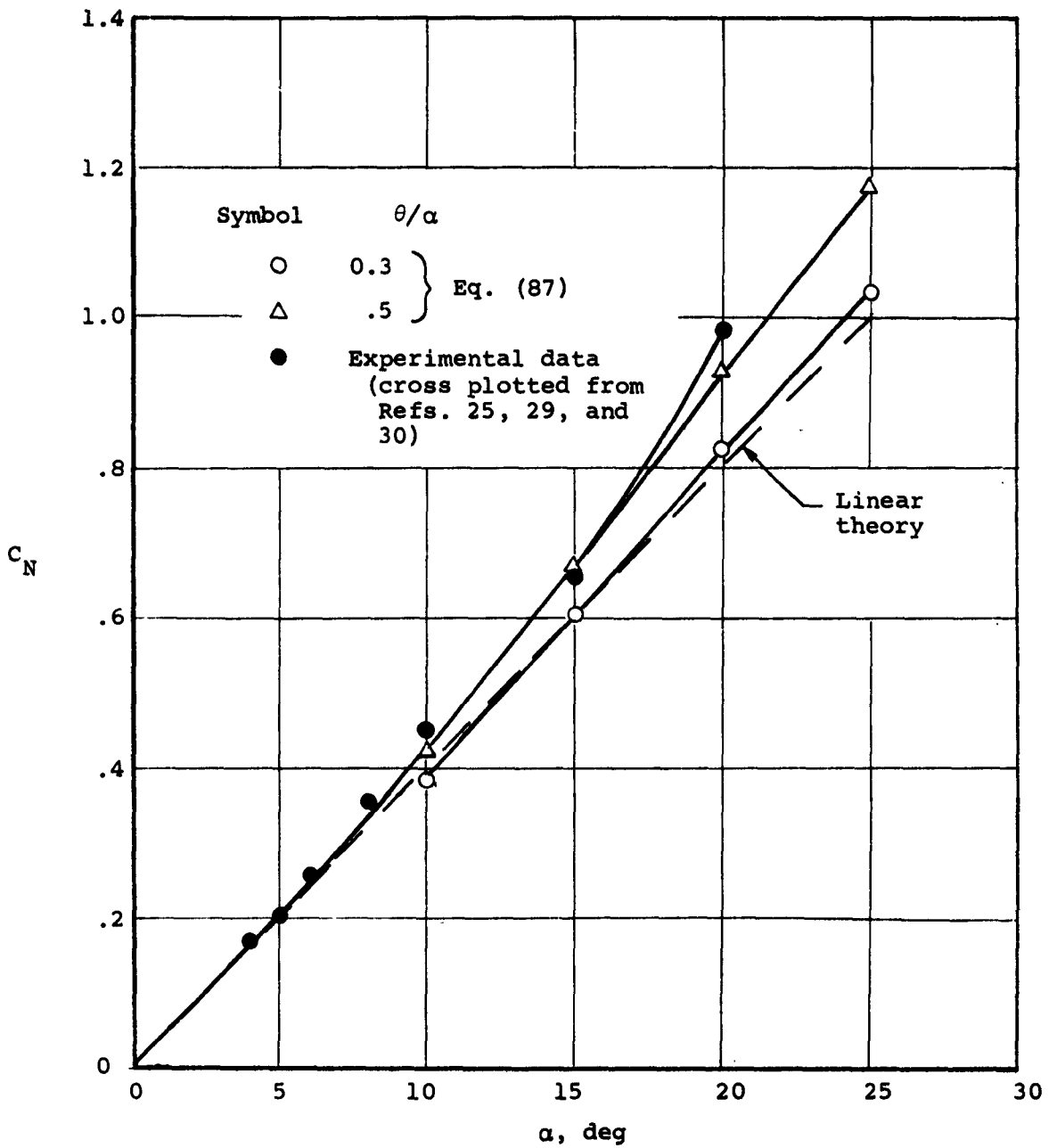
(a)   Normal force.

Figure 14.- Aerodynamics of a delta wing of aspect ratio 2
   for various shedding angles (8 wings, 19 harmonics).
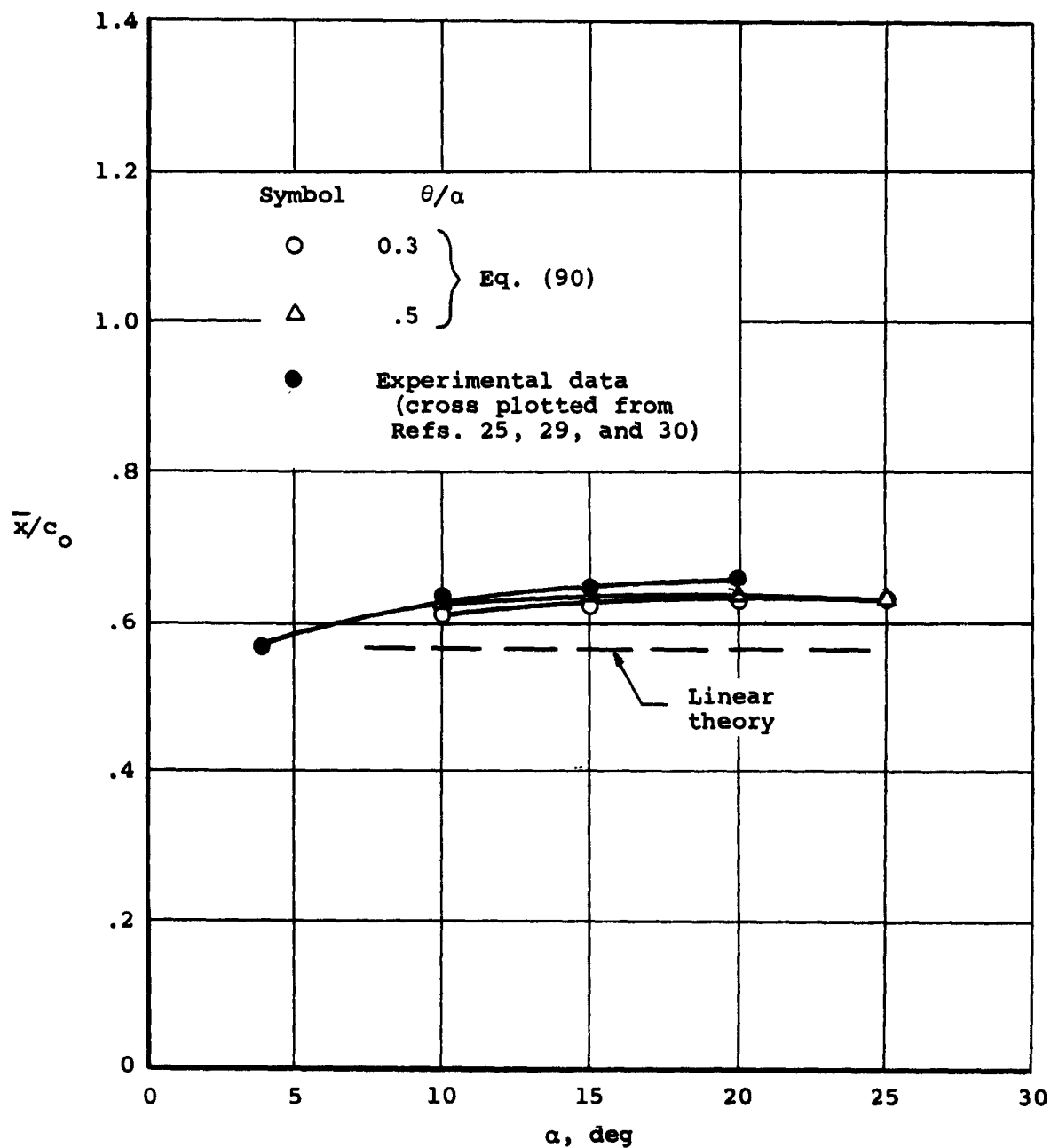
(b) Center of pressure.

Figure 14.- Concluded.
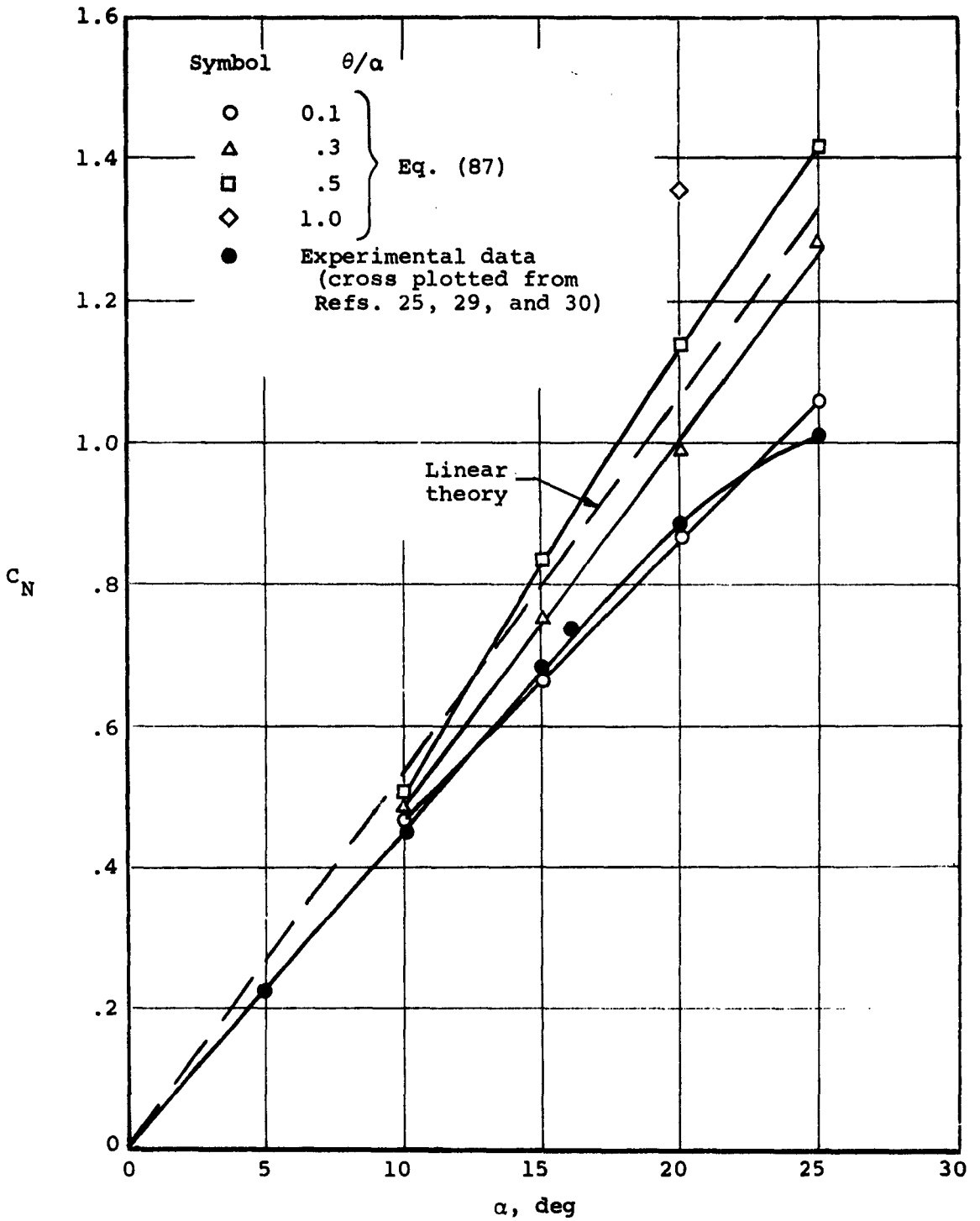
(a)   Normal force.

Figure 15.- Aerodynamics of a delta wing of aspect ratio 3
for various shedding angles (8 wings, 19 harmonics).
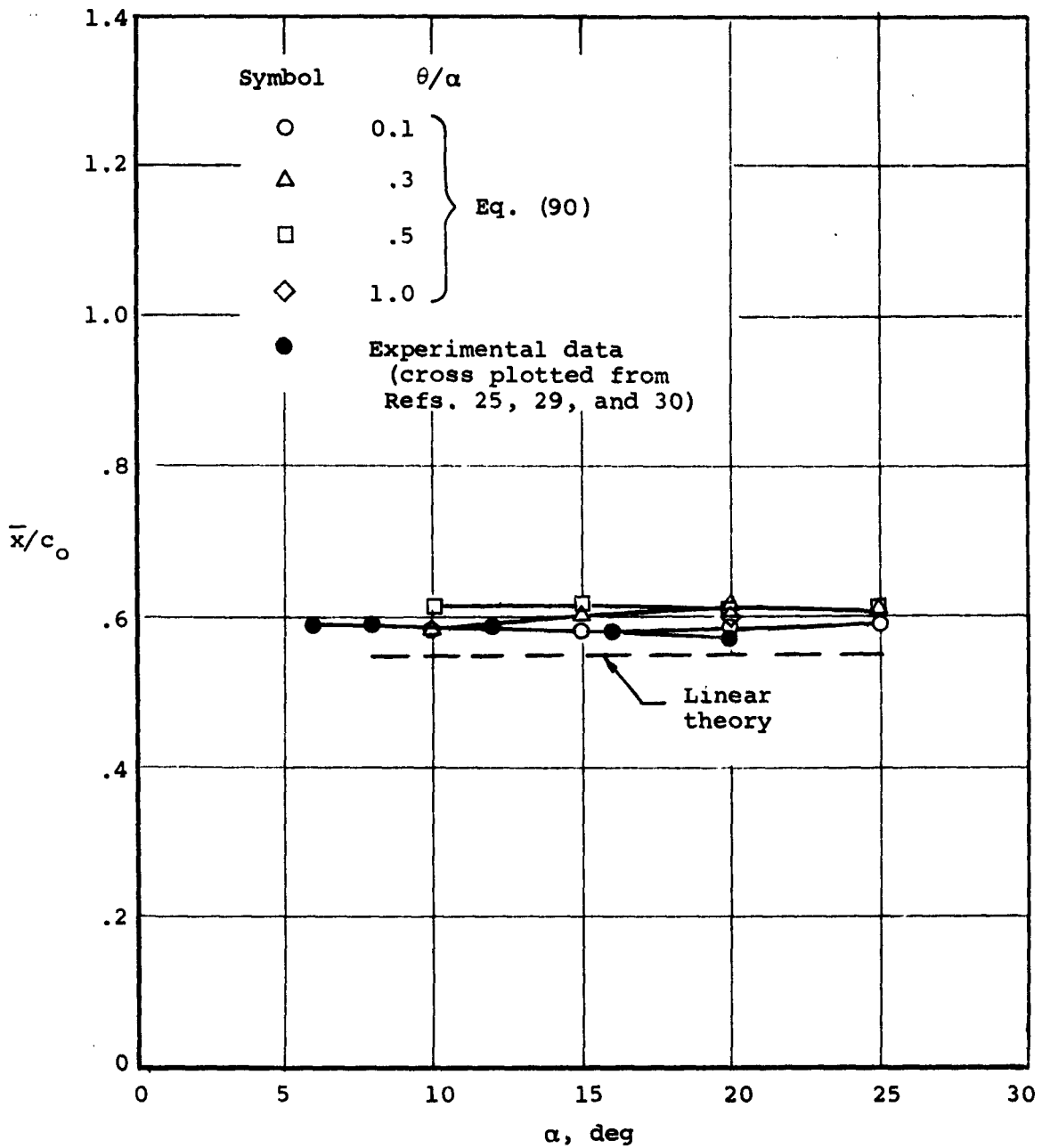
(b) Center of pressure.

Figure 15.- Concluded.
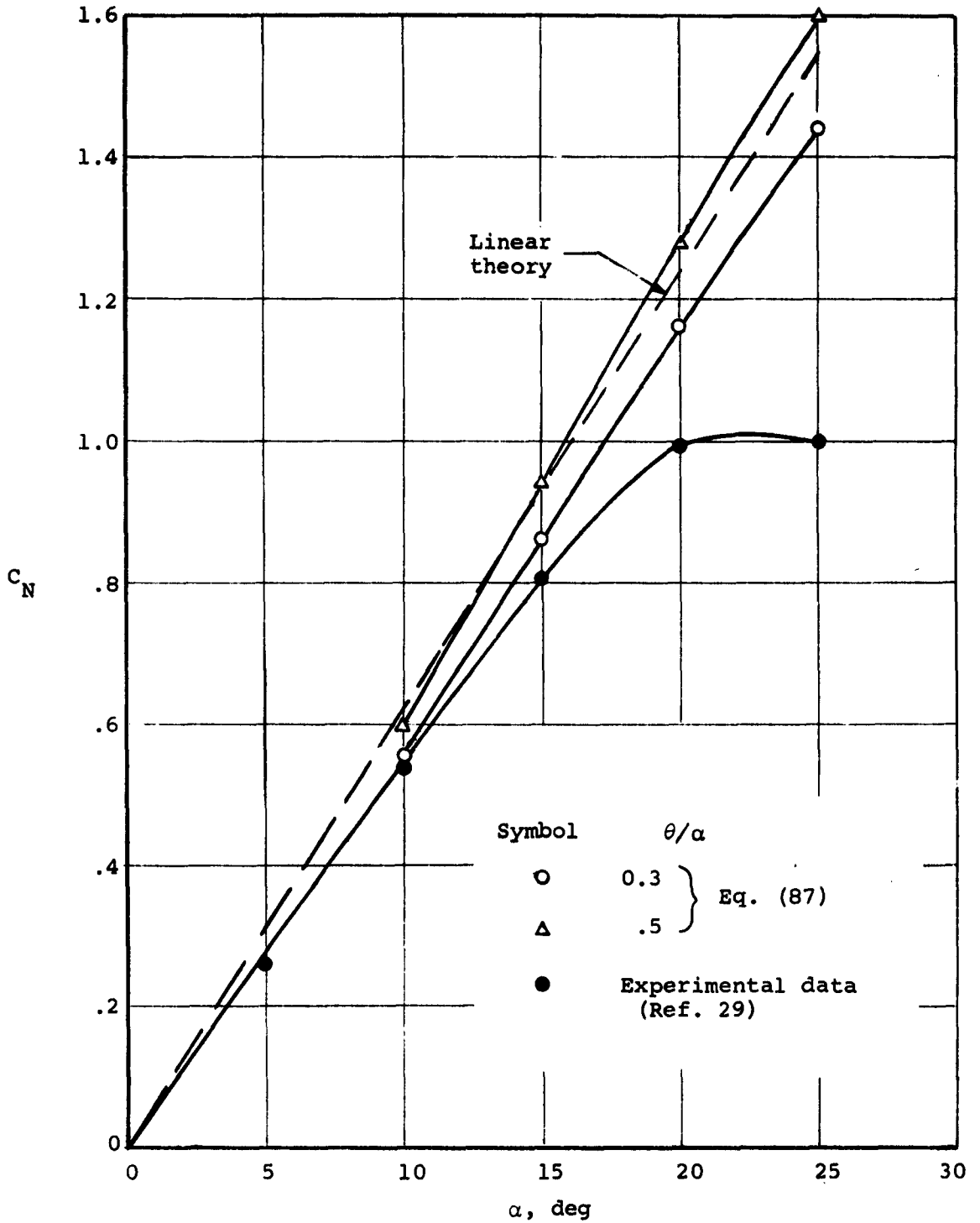
(a) Normal force.

Figure 16.- Aerodynamics of a delta wing of aspect ratio 4
for various shedding angles (8 wings, 19 harmonics).
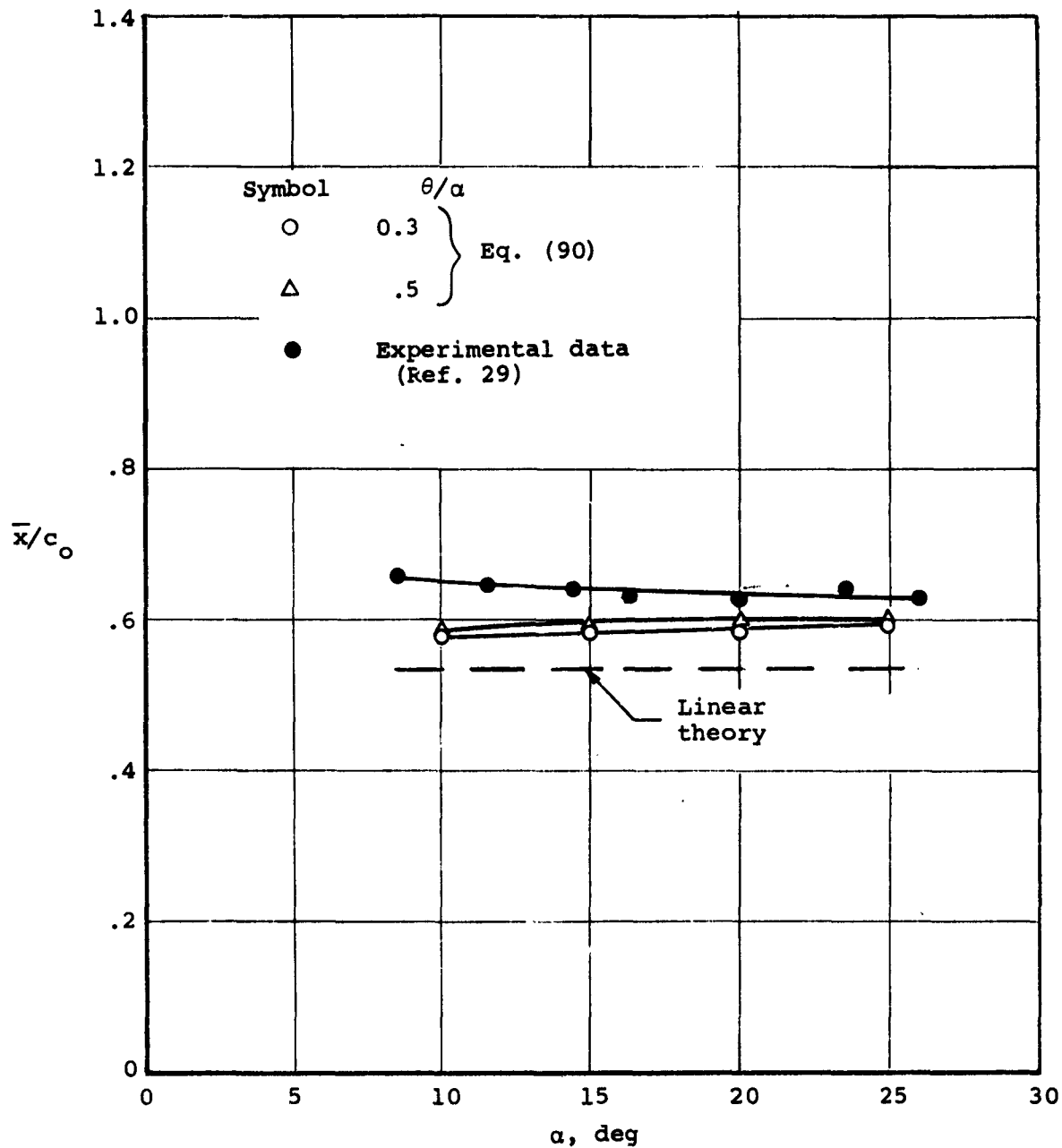
(b) Center of pressure.

Figure 16.- Concluded.
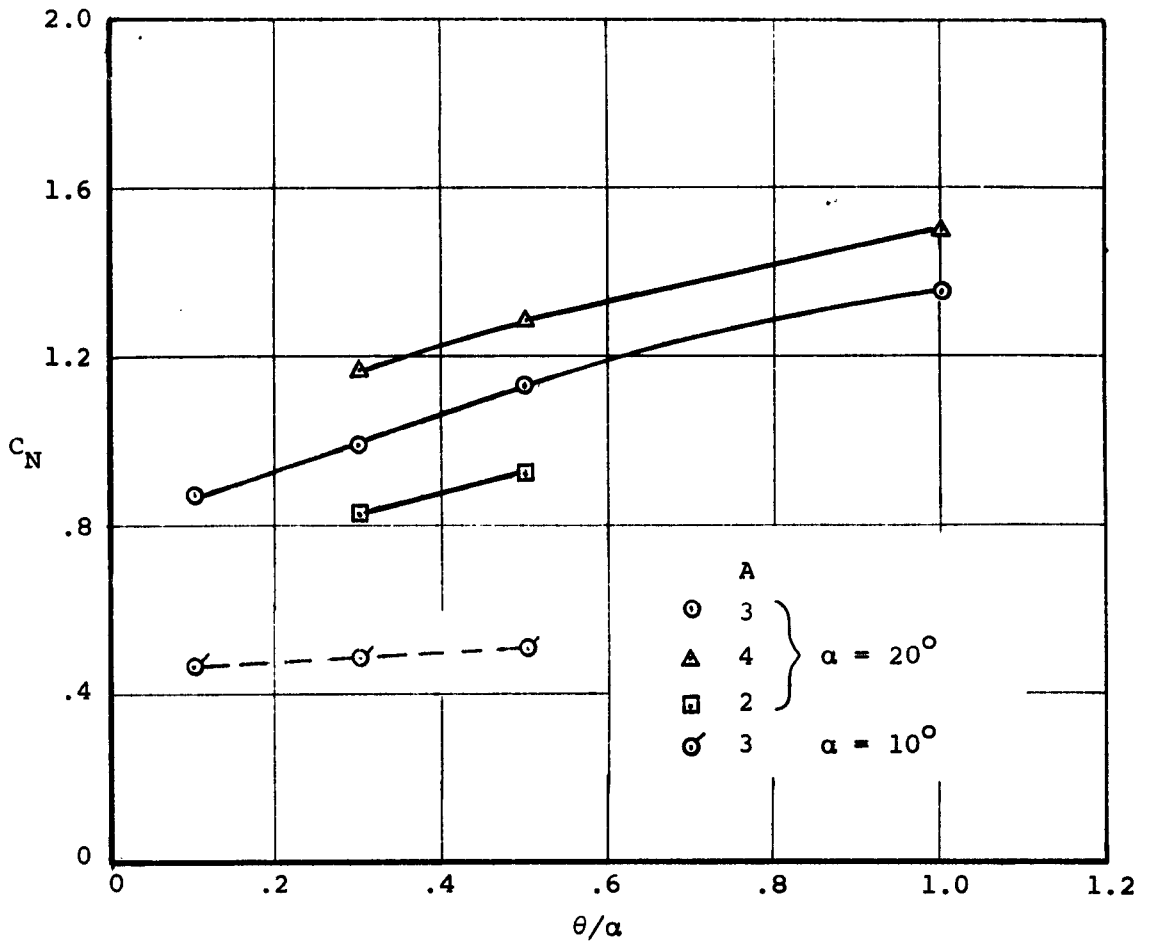
Figure 17.- Variation of calculated normal force
with shedding angle for delta wings.
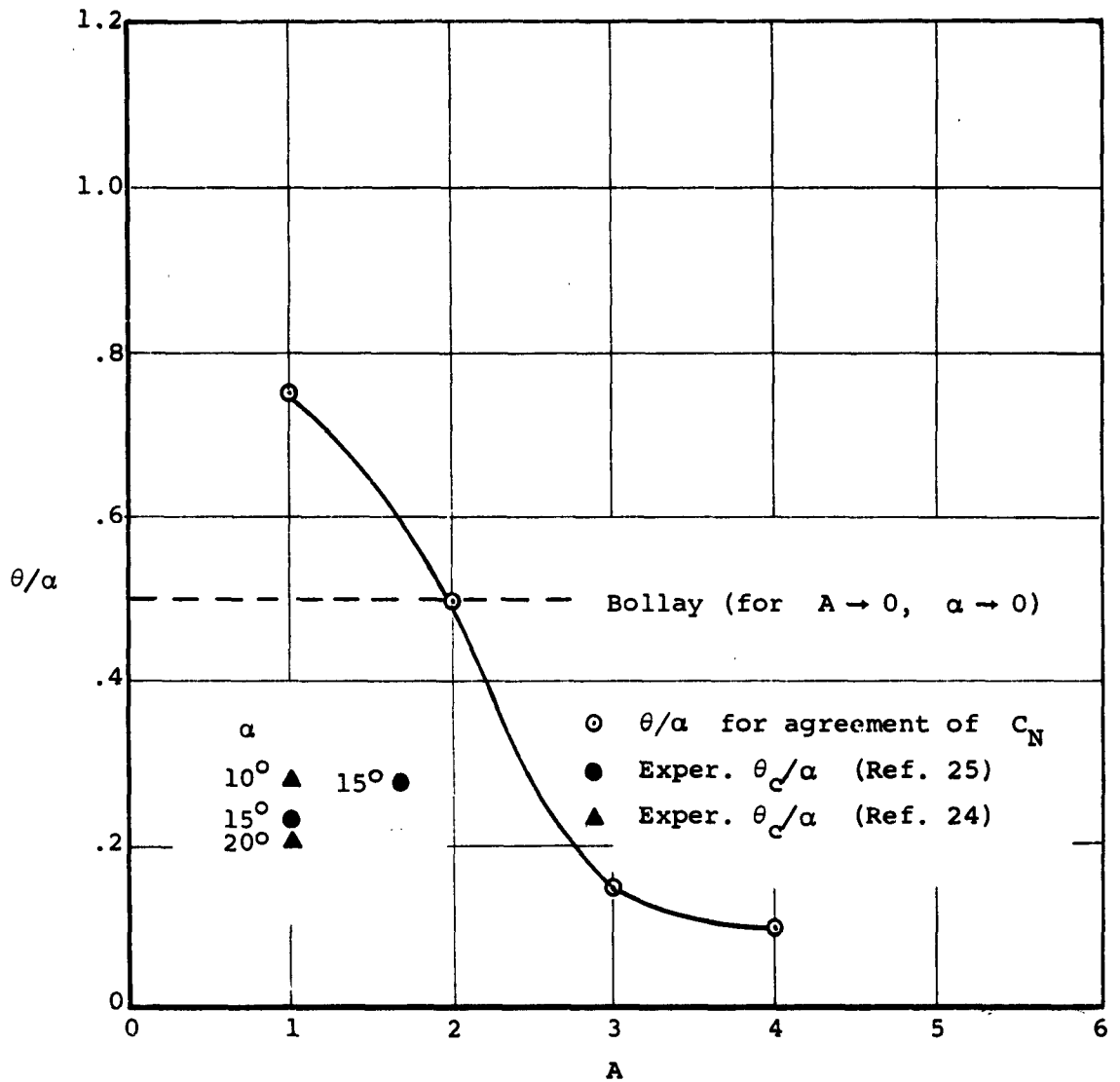
Figure 18.- Value of shedding angle required for accurate prediction of normal force on delta wings.
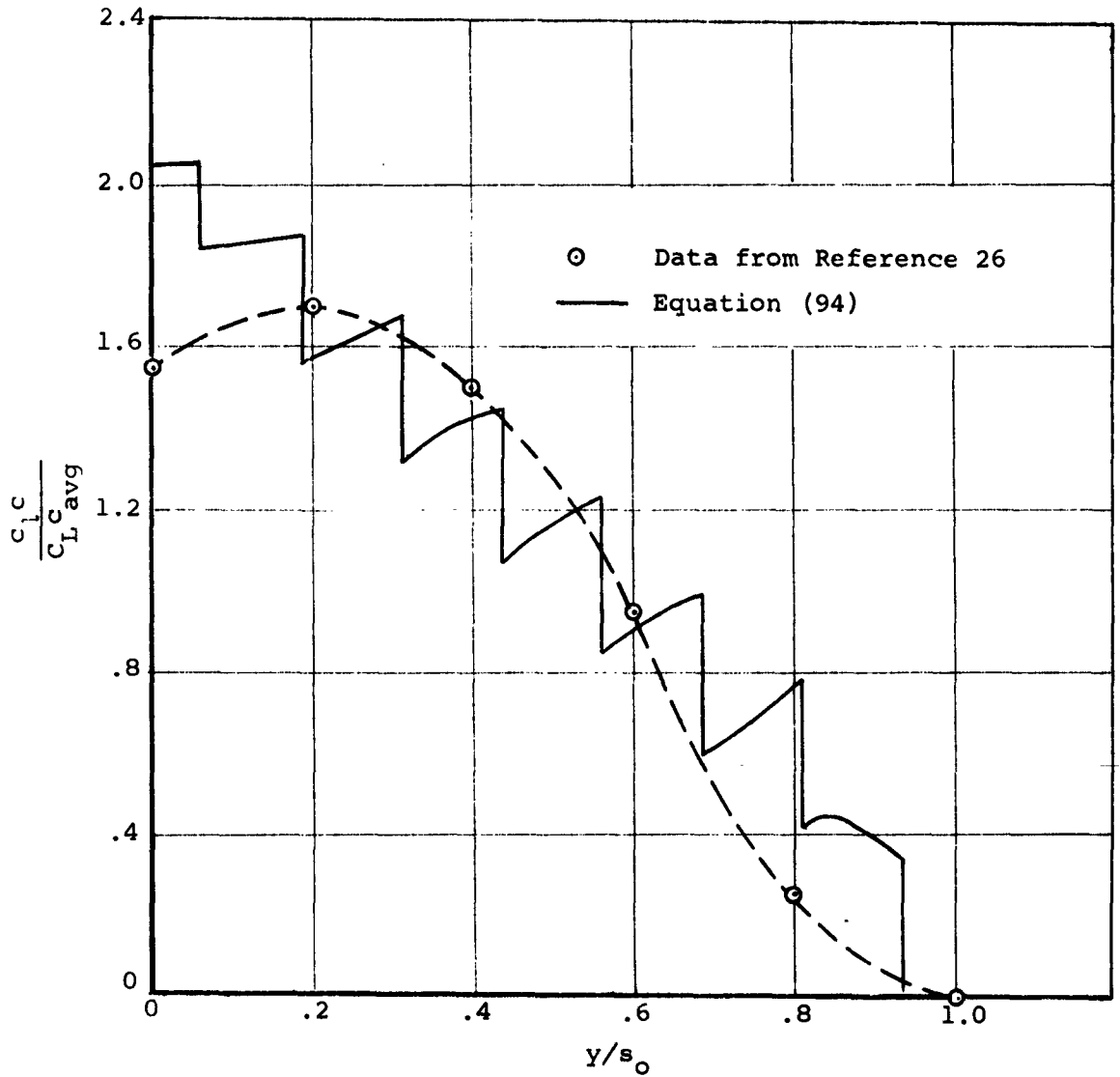
Figure 19.- Span loading on delta wing of aspect ratio 2
at $\alpha = 20^{\circ}$ for $\theta/\alpha = 0.5$ (8 wings, 19 harmonics).

APPROVED DISTRIBUTION LIST

CONTRACT Nonr-3103(00)

Chief, Bureau of Naval Weapons
(RAAD-3)
Department of the Navy
Washington 25, D. C.

Chief, Bureau of Naval Weapons
(RAAD-33)
Department of the Navy
Washington 25, D. C.

Chief, Bureau of Naval Weapons
(RAAD-34)
Department of the Navy
Washington 25, D. C.

Chief, Bureau of Naval Weapons
(RA-4)
Department of the Navy
Washington 25, D. C.

Chief, Bureau of Naval Weapons
(R-55)
Department of the Navy
Washington 25, D. C.

Chief, Bureau of Naval Weapons
(RR-25)
Department of the Navy
Washington 25, D. C.

Chief, Bureau of Naval Weapons
(RRRE-4)
Department of the Navy
Washington 25, D. C.

Commanding Officer and Director
David Taylor Model Basin
Aerodynamics Laboratory
Washington 25, D. C.

Chief of Naval Research (Code 461)
Department of the Navy
Washington 25, D. C.   (6 copies)

Chief of Naval Research (Code 438)
Department of the Navy
Washington 25, D. C.

Commanding Officer
Office of Naval Research Branch Office
Navy #100, Box 39, F. P. O.
New York, New York
ATTN: Head, Documents Section
                        (2 copies)

Commanding Officer
Office of Naval Research Branch Office
346 Broadway
New York 13, New York

Commanding Officer
Office of Naval Research Branch
86 E. Randolph Street
Chicago 1, Illinois

Commanding Officer
Office of Naval Research Branch Office
1030 E. Green Street
Padadena, California

Director
Naval Research Laboratory
Technical Information Office
Washington 25, D. C.   (6 copies)

Commander
Army Material Command
Department of the Army
Washington 25, D. C.
ATTN: AMCRD-RS-PE-A   (2 copies)

Commanding Officer
U. S. Army Transportation Research
  Command
Fort Eustis, Virginia
ATTN: SMOFE-TD   (1 copy)
ATTN: Research Reference Center
                           (1 copy)

Army Research Center
Physical Sciences Division
3045 Columbia Pike
Arlington 4, Virginia
ATTN: Mr. R. Ballard

U. S. Air Force (SRGL)
Office of Scientific Research
Washington 25, D. C.

Aeronautical Systems Division
Deputy for Technology
Wright-Patterson AFB, Ohio
ATTN: ASRSMS

Aeronautical Systems Division
Deputy for Technology
Wright-Patterson AFB, Ohio
ATTN: ASRSSC

Aeronautical Systems Division
Deputy for Technology
Wright-Patterson AFB, Ohio
ATTN: ASRMDF

Aeronautical Systems Division
Deputy for Systems Management
Support Systems Programs Office
Wright-Patterson AFB, Ohio
ATTN: ASZT

Armed Services Technical Information
 Agency
Document Service Center
Arlington Hall Station
Arlington 12, Virginia   (20 copies)

National Aeronautics and Space
 Administration
1512 H Street N. W.
Washington 25, D. C.
ATTN: Mr. J. Brewer, Code RA

National Aeronautics and Space
 Administration
1512 H Street N. W.
Washington 25, D. C.
ATTN: Mr. N. F. Rekos, Code RAP

National Aeronautics and Space
 Administration
Langley Research Center
Langley AFB, Virginia
ATTN: Mr. Donnelly

National Aeronautics and Space
 Administration
Ames Research Center
Moffett Field, California
ATTN: Mr. W. Cook, 40x80 Tunnel

Office of Technical Services
Department of Commerce
Washington 25, D. C.

Library
American Institute of Aeronautics and
 Astronautics
2 East 64th Street
New York 21, New York   (2 copies)

Bell Helicopter Company
P. O. Box 482
Fort Worth 1, Texas
ATTN: Mr. Robert Lynn

Cornell Aeronautical Laboratory, Inc.
4455 Genesee Street
Buffalo 21, New York
ATTN: Mr. Frank duWaldt

Collins Radio Company
Cedar Rapids, Iowa
ATTN: Dr. A. Lippisch

Georgia Institute of Technology
Guggenheim School of Aeronautics
Atlanta 13, Georgia
ATTN: Mr. D. W. Dutton

Hiller Aircraft Corporation
Advanced Research Division
1350 Willow Road
Palo Alto, California
ATTN: Mr. Raymond Lockwood

Massachusetts Institute of Technology
Aeronautical Engineering Department
Cambridge 30, Massachusetts
ATTN: Professor R. H. Miller

McDonnell Aircraft Corporation
St. Louis, Missouri
ATTN: Dr. Kurt Hohenemer

Mississippi State University
Engineering and Industrial Research
 Station
State College, Mississippi
ATTN: Dr. J. J. Cornish

Naval Postgraduate School
Aeronautical Engineering Department
Monterey, California
ATTN: Dr. R. Head

Princeton University
Aeronautical Engineering Department
James Forrestal Research Center
Princeton, New Jersey
ATTN: Professor David C. Hazen

Sikorsky Aircraft Division
United Aircraft Corporation
Stratford 1, Connecticut
ATTN: Mr. Philip Michel

Syracuse University
Mechanical Engineering Department
Syracuse, New York
ATTN: Dr. S. Eskinazi

Therm Advanced Research Division
Therm, Inc.
Ithaca, New York
ATTN: Dr. Ritter

Vehicle Research Corporation
1661 Lombardy Road
Pasadena, California
ATTN: Dr. Scott Rethorst

University of Virginia
Aeronautical Engineering Department
Charlottesville, Virginia
ATTN: Dr. G. B. Matthews

Vertol Division
Boeing Airplane Company
Woodland Avenue
Morton, Pennsylvania
ATTN: Dr. W. Z. Stepniewski

Vidya Division
Itek Corporation
1450 Page Mill Road
Stanford Industrial Park
Palo Alto, California
ATTN: Dr. J. N. Nielsen